NOTE TO USERS

Automated system for Monte Carlo determination of cutout factors of arbitrarily shaped electron beams and experimental verification of Monte Carlo calculated dose distributions

Claude Albaret

Medical Physics Unit
McGill University, Montreal
August 2004

A thesis submitted to the Faculty of Graduate Studies and Research of McGill University in partial fulfillment of the requirements of the degree of Master of Science in Medical Radiation Physics

Library and
Archives Canada

Published Heritage
Branch

395 Wellington Street
Ottawa ON K1A 0N4
Canada

Bibliothèque et
Archives Canada

Direction du
Patrimoine de l'édition

395, rue Wellington
Ottawa ON K1A 0N4
Canada

Canada

Abstract

Dose predictions by Monte-Carlo (MC) techniques could alleviate the measurement load required in linac commissioning and clinical radiotherapy practice, where small or irregular electron fields are routinely encountered. In particular, this study focused on the MC calculation of cutout factors for clinical electron beams. A MC model for a Varian linac CL2300C/D was built and validated for all electron energies and applicators. A MC user code for simulation of irregular cutouts was then developed and validated. Supported by a home-developed graphical user interface, it determines *in situ* cutout factors and depth dose curves for arbitrarily shaped electron fields and collects phase space data. Overall, the agreement between simulations and measurements was excellent for fields larger than 2 cm.

The MC model was also used to calculate dose distributions with the fast MC code XVMC in CT images of phantoms of clinical interest. These dose distributions were compared to dose calculations performed by the pencil-beam algorithm-based treatment planning system CadPlan and verified against measurements. Good agreement between calculations and measurements was achieved with both systems for phantoms containing 1-dimensional heterogeneities, provided a minimal quality of the CT images. In phantoms with 3-dimensional heterogeneities however, CadPlan appeared unable to predict the dose accurately, whereas MC provided with a more satisfactory dose distribution, despite some local discrepancies.

Résumé

L'application des méthodes Monte Carlo (MC) au calcul de dose pourrait réduire le nombre de mesures requises lors de la mise en service d'un accélérateur linéaire et dans la pratique clinique de la radiothérapie, où des champs étroits ou irréguliers sont communément rencontrés. En particulier, cette étude se concentre sur le calcul par MC de facteurs de découpage pour des faisceaux cliniques d'électrons. Un modèle MC de l'accélérateur linéaire Varian CL2300C/D a été construit et validé pour toutes les énergies et tous les applicateurs d'électrons. Un code utilisateur MC pour la simulation de découpages irréguliers a ensuite été développé et validé. Soutenu par une interface graphique utilisateur conçue spécialement, il détermine *in situ* des facteurs de découpage et rendements en profondeur de faisceaux d'électrons arbitrairement découpés et collecte des espaces de phase. Dans l'ensemble, les simulations et les mesures sont en excellent accord pour les champs de dimension supérieure à 2 cm.

Le modèle MC a été également utilisé pour calculer des distributions de dose avec le code MC rapide XVMC dans des images tomographiques de fantômes d'intérêt clinique. Les distributions de dose ainsi obtenues ont été comparées à celles calculées par le système de planification des traitements CadPlan de type algorithme à faisceau étroit et confronté à des valeurs expérimentales. Un bon accord est atteint avec les deux systèmes pour des fantômes contenant des hétérogenéités monodimensionelles, pourvu que la qualité des images CT soit raisonnable. En revanche, dans des fantômes avec des hétérogenéités tridimensionnelles, CadPlan est incapable de prédire la dose correctement, alors que MC fournit des distributions de dose plus satisfaisantes, en dépit de divergences localisées.

Acknowledgements

Table of Contents

List of Figures

*Validation of the central-axis doses calculated by CadPlan and XVMC in the case of a 12 MeV electron beam with a 10x10 cm² field size impinging on a solid water phantom with a 3 cm **bone** slab at 1 cm depth. The CadPlan calculations in the CT image of the phantom (dashed line) and the XVMC simulations in the compressed CT image of the phantom (continuous line) and in a mathematical phantom (+) are compared to the measurements performed with TLD-700 (o).*

*Profiles at z_{max} and R_{50} for a 12 MeV electron beam with a 10x10 cm² field size impinging on a solid water phantom with a 3 cm **bone** slab at 1 cm depth. The XVMC simulations in a compressed CT image (continuous line) and in a mathematical phantom (+) are compared to the dose calculations performed by CadPlan (dashed line).*

*Axial isodose distribution for a 12 MeV electron beam with a 10x10 cm² field size impinging on a solid water phantom with a 3 cm **bone** slab at 1 cm depth. The XVMC simulations in a compressed CT image (continuous line) are compared to the dose calculations performed by CadPlan (dashed line).*

Comparison of the central-axis dose calculated by CadPlan and XVMC for a 12 MeV electron beam with a 10x10 cm² field size impinging on the nose of the anthropomorphic phantom. The CadPlan calculations in the CT image of the phantom (dashed line) and the XVMC simulations in the compressed CT image of the phantom (continuous line) are compared to the raw measurements performed with TLD-700 (o).

Axial isodose (in cGy/100 MU) distribution for a 12 MeV electron beam with a 10x10 cm² field size impinging on the nose of the anthropomorphic phantom. The dashed line represents CadPlan doses reported to water and the crosses with a number correspond to raw TLD measurements reported as dose to medium.

Axial isodose (dose to medium in cGy/100 MU) distribution for a 12 MeV electron beam with a 10x10 cm² field size impinging on the nose of the anthropomorphic phantom. The continuous line represents XVMC simulations, the dashed line represents CadPlan calculation and the crosses with a number correspond to raw TLD measurements.

Percent difference $(D_{MC}-D_{TLD})$x100 between the XVMC calculated and measured dose to medium for a 12 MeV electron beam with a 10x10 cm² field size impinging on the nose of the anthropomorphic phantom. Differences written in yellow, blue and orange are within ±3%, lower than -3% and larger than +3% respectively.

List of Tables

Chapter 1. Introduction

With 67,400 victims in Canada in 2003[1], cancer remains the second leading cause of mortality, also responsible for 30% of the deaths and 20% of potential years of life lost in Quebec in 2000[2]. Significant advances have been made in the research on treatment alternatives such as immunotherapy[3], hyperthermia[4], photodynamic therapy[4], genetic manipulations and nanotechnologies[5,6]. Nevertheless, typical treatment nowadays still consists in a combination of surgery, chemotherapy and radiotherapy; the latter being involved at some stage in the treatment of half of the 139,900 new diagnosed cases.

The first part of this introductory chapter is devoted to the principles and techniques of radiotherapy. A second part will be concerned with the various aspects of treatment process, with a special emphasis on treatment planning. Finally, the structure and rationale of the thesis will be briefly described.

1.1 Radiation therapy

1.1.1 Principle

Cancer is an erratic proliferation of cells that can spread to adjacent tissues or to remote areas of the body through lymphatic and blood routes. Radiotherapy, defined as use of ionizing radiation for therapeutic purposes, aims at tumor eradication and proliferation control while sparing healthy surrounding tissues. It emerged after the discoveries of x-rays by W. Roentgen in 1895 and natural radioactivity by H. Becquerel and M. Curie in the following years. The first case of successful radiation treatment was reported in 1899[7].

From a radiobiological point of view, ionizing radiation acts on cells by transferring energy to the genetic material of the cells, thereby killing cells or preventing their replication. Directly ionizing radiation transfers energy through charged particles that ionize and excite DNA molecules. Conversely, indirectly ionizing radiation is delivered by neutral particles like neutrons and photons releasing chemically active free

1

radicals that further interact with the DNA. Amongst these radiation-induced damages, double-strand break of the DNA is the predominant cause of cell death[8]. The seriousness of the damage to cancerous tissues, and consequently the probability of cure, is correlated to the amount of energy absorbed per unit mass of tissue or *absorbed dose*[9] (The international standard unit for dose is the Gray, 1 Gy = 1 J/kg). The tumor lethal dose required to achieve 95% tumor control probability typically lies between 20 and 80 Gy, depending on the volume and localization of the target as well as on its radiosensitivity, differentiation and type[10]. Those various aspects of the lesion also determine the type of treatment chosen. The various treatment modalities are summarized in the following section.

1.1.2 Types of radiation therapies

Radiotherapy can be administered to a patient either by insertion of sealed radioactive sources inside the body (*brachytherapy*) or by external kilovoltage or megavoltage beams of particles (*external beam therapy* or *teletherapy*). Even though heavy-ions and protons have proven to be advantageous for certain pathologies, they have not reached cost-effectiveness yet and external-beam radiotherapy mainly uses photons and electrons of energy ranging from a few keV to a few MeV.

With the same radiobiological properties as photons, electrons exhibit additional features of a high surface dose, a uniform maximum dose region and a rapid distal dose fall-off. Figure 1.1 shows the central-axis depth dose curve for electron beams compared to that for photons of a 200 kV and a 6 MV. Electrons are therefore especially useful for sub-dermal lesions at a depth down to 6 cm such as skin, lip, ear, scar tissue, chest wall after radical mastectomy, fungus micosis, adenosis carcinoma, head and neck tumors, and residual tumors[11,12]. Overall, electrons are involved in the treatment of at least 20% of the patients undergoing radiation therapy in Canada.

Both types of external beam radiotherapy sources, radioisotope units and linear accelerators, are mounted on a gantry rotating around the patient couch. Teletherapy radioisotope units release high energy gamma rays produced by the decay of an unstable isotope such as Cobalt-60, Cesium-137 or Europium-152. The principle of particle

acceleration in linear accelerators is based on transport of electro-magnetic waves as described below.
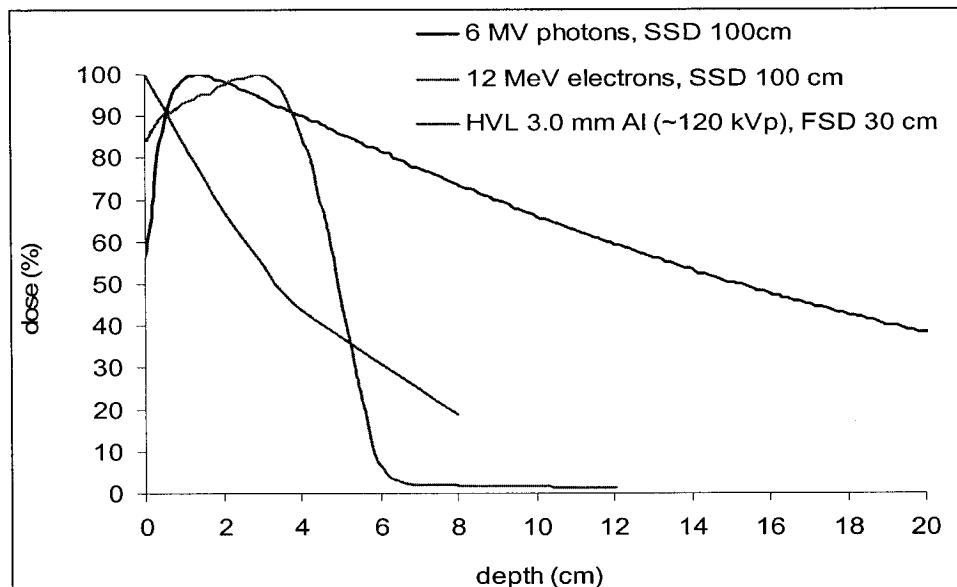
Figure 1.1: Central-axis depth dose curve for a 12 MeV electron beam, a 120 kV_p x-ray beam (<E>~35 keV) and a 6 MV photon beam.

1.1.3 Principle of particle creation in external beam therapy

Medical linear accelerators or *linacs* appeared in the 70s. They produce ionizing radiation by acceleration of electrons. Either the electrons themselves are used or the original electron pencil beam is decelerated through a target made in a material with high atomic number, leading to bremsstrahlung. A typical modern megavoltage medical accelerator can produce photons beams of 6 and 18 MV and electron beams of several energies (6-25 MeV). Linacs are particle accelerators using non-conservative microwave RF fields in the frequency range 10^3 MHz (L-band) to 10^4 MHz (X-band), a majority of them running at 2856 MHz (S-band). The schematic composition of a high energy S-band linac is presented in Figure 1.2. First, electrons of a few keV produced by thermo-ionic emission in the electron gun are brought to megavoltage kinetic energies in accelerating waveguides. The accelerating waveguide is an evacuated metallic tube separated into resonant cavities and fed by high power radiofrequency waves (RF). The high power RF is produced through deceleration of electrons by retarding potentials in magnetron or

klystron type waveguides and transported to the accelerating waveguide through a unidirectional waveguide filled with high pressure dielectric gas. A pulsed modulator releasing ultra-short discharges of high current (100 kV, 100 A, 1 μs) is powering both the electron gun and the microwave power source. As the waveguide of a linac operating at energies above 6 MeV is too long to be mounted straight-through as well as for energy selection purposes, the pencil electron beam is bent, steered and focused by a series of magnets and directed towards the linac head.
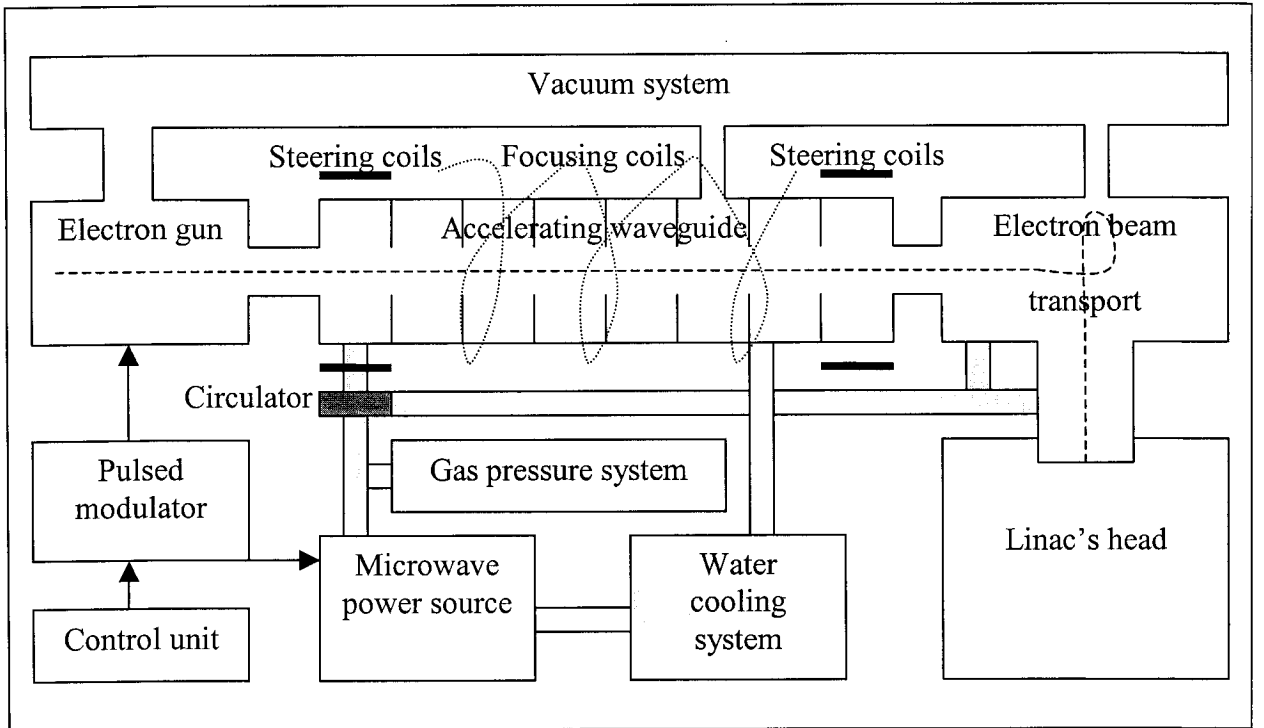
Figure 1.2: Schematics of a high energy S-band medical linear accelerator (adapted from Van Dyk[4]).

At that point in the Varian linac used in this work, in the photon mode, the pencil beam impinges on a high atomic number material target where a Gaussian beam of forward-peaked photons is created by bremsstrahlung. A flattening filter then attenuates preferentially the center of the beam to produce a uniform dose profile. In the electron mode, target and flattening filter are retracted and a set of scattering foils in materials of high atomic number intercepts the beam instead and spreads it into a field as wide as 25x25 cm^2 maximum. In either mode, the beam is collimated by a primary circular

collimator in a material of high atomic number and further truncated into a field of maximum dimension 40x40 cm^2 at the isocenter by an adjustable rectangular collimator consisting in a set of two independent upper and lower jaws. Finally, in the electron mode, because of important scatter of electrons in the air between the jaws and the patient, the beam is last shaped by a rectangular applicator ending at 5 cm from the patient surface. In Varian linacs like the one used in this project, the applicator supports two rectangular trimmers made in an alloy of nickel and bismuth and a custom-made cerrobend or steel cutout. Between the two first collimators, the beam output and flatness are monitored by two transmission ionization chambers, which also end the irradiation when the prescribed dose has been delivered. The components of a Varian linac head in the electron mode are presented in Figure 1.3.
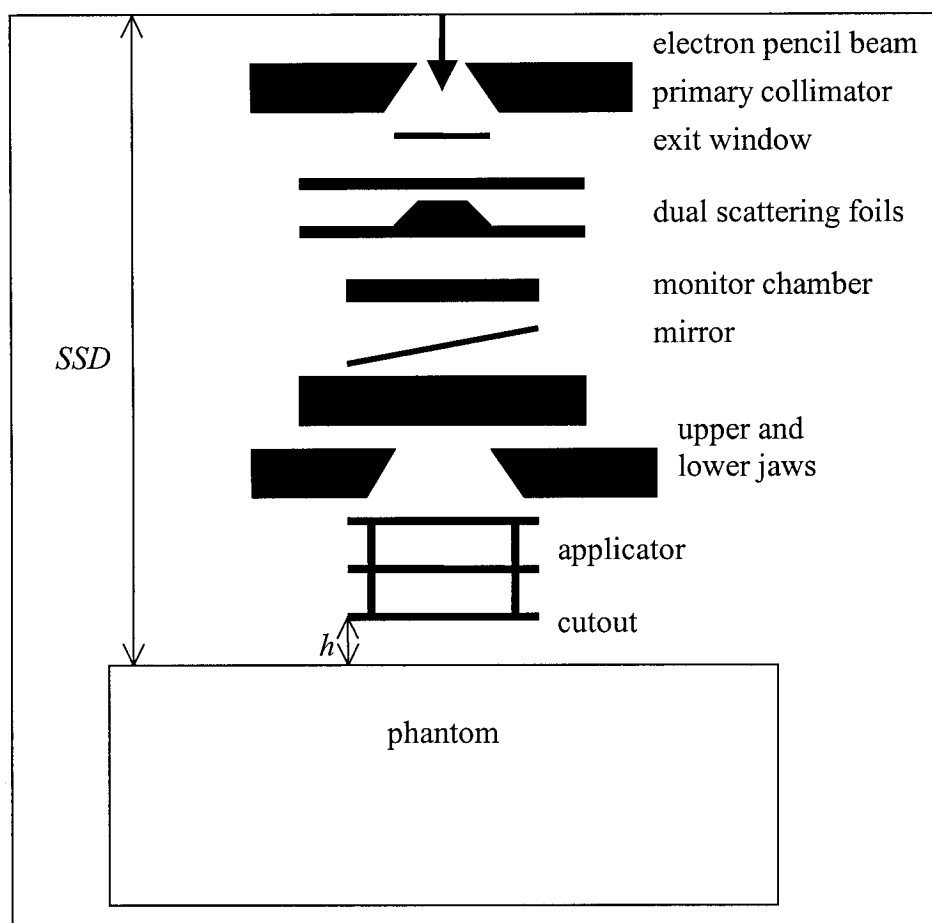
Figure 1.3: Schematics of a Varian high energy medical linear accelerator head in the electron mode. The height of the air gap between the electron cutout and the surface of the phantom, h, is equal to the source-to-surface distance (SSD) minus 95 cm.

5

1.2 Treatment planning

The notion of treatment planning encompasses the joint efforts of the radiation oncology department to treat the patient from the diagnosis until the actual delivery of the treatment. This section first summarizes the successive steps involved in electron beam treatment planning and then details the existing treatment planning systems and the potential impact of the Monte Carlo techniques in electron therapy treatment planning.

1.2.1 Treatment process

An external beam therapy treatment consists of the following steps. First, the diagnosed cancer is evaluated by various techniques ranging from medical examination, biopsy, to various imaging modalities such as diagnostic x-ray, mammography, Magnetic Resonance Imaging (MRI), Computed Tomography (CT), Positron Emission Tomography (PET), Single Positron Emission Tomography (SPECT). Thus, the type, volume and localization of the target and organs at risk with respect to skin markers and anatomical landmarks are determined and delineated by the oncologist. The latter prescribes a dose to the _planning target volume_[13] and sets upper limits on the doses to the surrounding critical structures. These dose values are input into the treatment planning system. A beam configuration (particle type, energy, orientation, beam collimation and modification) is proposed and the corresponding dose distribution in the patient is computed by the treatment planning system. The beam combination inducing the dose distribution that provides the better conformity to the target is selected by iteration. Next, the treatment itself is delivered, in daily fractions of typically 2 Gy for 3 to 6 weeks. Megavoltage portal images acquired with radiographic film, electronic portal imaging devices (EPID) or ultrasound allow for _in situ_ verification of the treatment position. Finally, a long term patient follow-up is conducted.

To support the treatment planning process, an image of the patient can be taken with a conventional simulator[4] which mimics the geometry and motion of an actual treatment unit but uses an x-ray tube instead of a megavoltage source. Simulators play a key role in the treatment simulation, verification and monitoring. The target can then be localized with respect to anatomical landmarks and skin markers. Dose distributions are calculated in a single plane containing the tumor, with corrections for patient contour

only. This 2D treatment planning technique is limited by poor contrast which renders the visualization of the tumor difficult and by the absence of heterogeneity corrections in the dose calculation. Computed tomography (CT) nowadays yields 3-dimensional images with a better soft tissue contrast and thereby allows for improved target localization and the potential to use heterogeneity corrections in the dose calculations based on the density of the CT data. Along with the CT images, simulation software can reconstruct the images in any plane, project the treatment field outline on the delineated patient structures and build a *digitally reconstructed planar radiograph* (DRR). DRRs show the desired set-up of the patient anatomy with respect to the treatment field and hence improve accuracy of beam placement.

The International Commission on Radiation Units and Measurements (ICRU)[14], recommends a ± 5% accuracy at the 1σ level in the absorbed dose delivery. In order to meet this goal, an accuracy of 2.5% should be achieved through the following steps[4]: determination of absolute dose at a reference point in water, acquisition of doses at various depths relative to dose at the reference point, calculation of dose distribution and irradiation. The final accuracy of the treatment also depends on the CT data acquisition and organ delineation. The treatment planning process mentioned above applies to photon beam therapy mostly. Indeed, due to the absence of a reliable treatment planning system for electron beam therapy, no such accuracy can be reached.

1.2.2 Electron treatment planning systems and the potential impact of the Monte Carlo technique

The accuracy of the treatment planning system (TPS) is critical to the treatment success. A TPS adds the contributions of the various beams involved in a treatment and corrects for surface contour and heterogeneities. Current data-based or analytical model-based TPSs achieve this task successfully for photon beams or broad electron beams in phantoms with slab geometry. However, for electron beams in more realistic geometries, they yield dose distributions near 3D heterogeneities with errors as high as 40% (in the extreme case of heterogeneities with low or high density with respect to the surrounding medium) as reported in the literature[15-18]. Moreover, TPSs fail at predicting the output in situations of lateral electronic disequilibrium, where the pencil beam spread exceeds the

range of laterally scattered electrons. Indeed, TPSs ignore the scatter from beam collimating devices and model very approximately the patient's heterogeneities. Accurate TPSs should include the effect of electron scattering and energy loss in all stages of beam definition and energy deposition.

The algorithms of choice for electron beam treatment planning are pencil beam algorithms. Electron beam TPSs like CadPlan 6.7.2 (Varian) use Hogstrom's pencil beam algorithm, based on the Fermi-Eyges solution to electron transport equation. Hogstrom[19] first proposed to approximate the spatial distribution of electron beams by a radially symmetric Gaussian. Lax[20] further suggested to better account for the spread of a pencil beam due to large angle scattering and range straggling by summing three Gaussians, improving dose calculation accuracy by 20%. The parameters of the Gaussians are deduced from pre-calculated Monte-Carlo kernels in homogeneous media. The pencil beams, appropriately[21] scaled according to the electron density of the medium retrieved from the CT data, are superimposed on the dose matrix. The hypothesis underlying this method is to treat all heterogeneities as semi-infinite slabs, which has been proven to be inappropriate for two- or three-dimensional heterogeneities[22,23] in the direction perpendicular to the beam axis, due to broadening of the pencil beam. Furthermore, conventional TPSs systematically report the dose to water rather than the dose to medium, which constitutes another significant approximation.

In this context, the Monte Carlo technique, no longer withheld by computing power issues, offers a serious potential for improving patient treatment by computing dose with better accuracy. The Monte Carlo algorithm calculates dose distributions through explicit radiation transport by using random number generators to sample from interaction cross sections and probability distributions. By explicitly simulating the particles emerging from the accelerator head to the patient, the Monte Carlo method provides a comprehensive and accurate dose calculation in the medium[14,24-27] obviating the need for approximations and justifying the apparition of Monte Carlo Treatment Planning Systems for clinical electron beams[28,29].

1.3 Rationale and structure of the thesis

The aim of this thesis is to investigate the ability of the Monte Carlo (MC) technique to plan electron treatments, with special emphasis on calculation of relative output factors versus cutout size (or cutout factors). A model for a Varian CL2300C/D linac was built using the EGSnrc/BEAMnrc[30] MC code and validated for dose calculation and prediction of cutout factors for regular fields. An EGSnrc user code for transport of particles through cutouts of arbitrary shapes was then developed. A graphical user interface was also designed to facilitate routine clinical use of the code. Finally, dose distributions in homogeneous, heterogeneous and anthropomorphic phantoms calculated by the Voxel Monte Carlo code (XVMC) and CadPlan 6.7.2 (Varian) were compared with measurements.

The chapter following this introduction summarizes the physical interactions of ionizing radiation with matter and some concepts of electron beam dosimetry. The equipment used as well as the experimental and simulation techniques followed are described in the third chapter. In the fourth chapter, the results obtained for the BEAM model, for the automated cutout calculator system and for the dose distributions in phantoms are presented and discussed, leading to the conclusion in chapter six, where some future work is also planned.

References:

[1] National Cancer Institute of Canada: Canadian Cancer Statistics 2003, Toronto, Canada, 2003

[2] Gouvernement du Québec, Ministère de la Santé et des Services Sociaux, "La radiothérapie au Québec, situation actuelle et perspectives", Comité de Radio-Oncologie du Conseil Québécois de Lutte contre le Cancer, mars 2000

[3] L. J. Old, "Immunotherapy for cancer", Sci. Am. **275** (3), 150-154 (1996)

[4] J. Van Dyk, *The Modern Technology of Radiation Oncology: A Compendium for Medical Physicists and Radiation Oncologists* (Medical Physics Publishing, Madison, Wisconsin, 1999)

[5] A. Sutton, "Researchers explore possible applications of nanotechnology in cancer treatment", OncoLog **48** (7/8) (2003)

[6] A. P. Alivisatos, "Less is more in medicine", Sci. Am. **285** (3), 66-73 (2001)

[7] C. A. Perez, L. W. Brady, J. L. Roti, Overview in *Principles and Practice of Radiation Oncology*, Eds C. A. Perez, L. W. Brady, Philadelphia PA: Lippincott-Raven, 1-78 (1998)

[8] M. Tubiana, J. Dutreix, A. Wambersie, *Radiobiologie*, Taylor & Francis, London-New York-Philadelphia (1990)

[9] ICRU Report No. 33, "Radiation Quantities and Units", International Commission on Radiation Units and Measurements, Washington, DC (1980)

[10] P. Rubin, S. McDonald, R. Qazi, *Clinical Oncology: a multidisciplinary approach for physicians and students*, Eds W. B. Saunders Company (1993)

[11] S. C. Klevenhagen, *Physics of Electron Beam Therapy*, Medical Physics Handbooks 13, Adam Hilger Ltd, Bristol, England (1985)

[12] N. Tapley, *Clinical Applications of Electron Beams*, Robert E. Krieger Publishing Company, Malabar, FL (1982)

[13] ICRU, "Prescribing, Recording, and Reporting Photon Beam Therapy", ICRU Report No. 50, International Commission on Radiation Units and Measurements, Washington, D.C. 1993

[14] ICRU, "Determination of absorbed dose in a patient irradiated by x or gamma rays in radiotherapy procedures ", ICRU Report No. 24, International Commission on Radiation Units and Measurements, Washington, D.C. 1976

[15] E. Mah, J. Antolak, J. W. Scrimger, J. J. Battista, "Experimental evaluation of a 2D and 3D electron pencil beam algorithm", Phys. Med. Biol. **34**, 235-249 (1986)

[16] J. E. Cygler, J. J. Battista, J. W. Scrimger, E. Mah, J. Antolak, "Electron dose distributions in experimental phantoms: a comparison with 2D pencil beam calculations", Phys. Med. Biol. **32** (9), 1073-1086 (1987)

[17] J. Seuntjens, A. Van der Plaetsen, H. Thierens, M. Piessens, "Comparison of measured and calculated dose distributions in lung after electron beam treatment of the chest wall", Med. Phys. **21** (12), 1959-1968 (1994)

[18] G. X. Ding, J. E. Cygler, G. G. Zhang, M. K. Yu, "Evaluation of a three-dimensional electron beam treatment planning system", Med. Phys. **26** (12), 2571-2580 (1999)

[19] K. R. Hogstrom, M. D. Mills, P. R. Almond, "Electron beam dose calculations", Phys. Med. Biol. **26** (3), 445-459 (1981)

[20] I. Lax, A. Brahme, P. Andreo, "Electron beam dose planning using Gaussian beams. Improved radial dose profiles", Acta Radiol. Suppl. **364**, 49-59 (1983)

[21] I. Lax, A. Brahme, "Electron beam dose planning using Gaussian beams. Energy and spatial scaling with inhomogeneities", Acta Radiol. Oncol. **24**, 75-85 (1985)

[22] I. Lax, "Inhomogeneity corrections in electron-beam dose planning. Limitations of the semi-infinite slab approximation", Phys. Med. Biol. **31**, 879-892 (1986)

[23] A. Brahme, "Current algorithms for computed electron beam dose planning", Radioth. Oncol. **3**, 347-362, (1985)

[24] K. R. Shortt, C. K. Ross, A. F. Bielajew, D. W. O. Rogers, "Electron beam dose distributions near standard inhomogeneities", Phys. Med. Biol. **1** (3) 235-249 (1986)

[25] A. A. Al-Beteri, D. E. Raeside, "Optimal electron-beam treatment planning for retinoblastoma using a new three-dimensional Monte Carlo-based treatment planning system", Med. Phys. **19** (1), 125-135 (1992)

[26] R. Doucet, M. Olivares, F. DeBlois, E. B. Podgorsak, I. Kawrakow, J. Seuntjens, "Comparison of measured and Monte Carlo calculated dose distributions in homogeneous phantoms in clinical electron beams", Phys. Med. Biol. **48** (15), 2339-2354 (2003)

[27] K. R. Hogstrom, "3D Electron Beam Dose Algorithms", in *3D Radiation Treatment Planning and Conformal Therapy*, J. A. Purdy, B. Emami, International Symposium Proceedings, Medical Physics Publishing (1995)

[28] J. E. Cygler, G. M. Daskalov, G. H. Chan, G. X. Ding, "Evaluation of commercial Monte Carlo electron treatment planning", Med. Phys. **31** (1), 141-153 (2004)

[29] C. M. Ma, E. Mok, A. Kapur, T. Pawlicki, D. Findley, S. Brain, K. Forster, A. L. Boyer, "Clinical implementation of a Monte Carlo treatment planning system", Med. Phys. **26** (10), 2133-2143 (1999)

[30] D. W. O. Rogers, B. A. Faddegon, G. X. Ding, C. M. Ma, J. Wei, T. R. Mackie, "BEAM: A Monte Carlo code to simulate radiotherapy treatment units", Med. Phys. **22** (5), 503-524 (1995)

Chapter 2. Physics of electron beam therapy

This chapter presents the physical background underlying electron beam therapy. The efficiency of electron beams at damaging cancerous tissues is a consequence of the energy they transfer to tissues through various interactions processes, which are presented in the first section of this chapter. Quantification of the energy transfers through the concept of dose, as detailed in the second part of this chapter, is necessary to any treatment planning process.

2.1 Interactions of electrons with matter

Electrons travelling through a medium engage in Coulomb interactions with the nuclear or electronic field of the atoms in the medium. These interactions, listed in a first part of this chapter, consist mainly in energy loss, a phenomenon estimated by the notion of stopping power as described in a second part; or in change of directions of travel of the electrons, events quantified by the scattering power of a material as defined in the third part. The type of interaction that an electron will undergo depends both on the incident electron energy and on the magnitude of its impact parameter b with respect to the atomic radius a as illustrated in Figure 2.1. The impact parameter is the distance of closest approach between the undisturbed path of the projectile and the target.
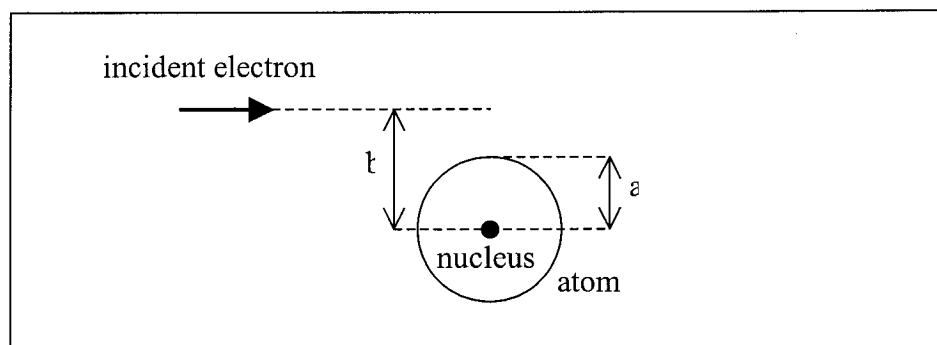
Figure 2.1: Diagram showing an electron traversing the Coulomb field of an atom of radius a with an impact parameter b, perpendicular distance between the electron path and the atom nucleus.

2.1.1 Energy loss mechanisms

Energy loss mechanisms are of special interest to us since radiotherapy relies on the notion of dose or energy deposited per unit mass medium. Energy can be transferred to the medium through collisions with the medium, as detailed firstly, or through emission of electromagnetic waves, as presented in a second part. Finally, the notion of stopping power that quantifies the energy loss is defined.

2.1.1.a Collisions

Collisions can be elastic or inelastic depending on whether the particle is only deflected or loses some energy as well. When the electron impinges on the medium at a large distance from a given atom (*i.e.* $b>>a$), it interacts with the atom as a whole in a soft collision. Although soft collisions only induce small energy losses, they happen frequently enough to account for half of the global energy loss that an electron experiences in a medium. Hard collisions occur between an electron and the orbital electrons of an atom (*i.e.* when $b\sim a$), and lead to significant energy transfers accounting for half of the overall energy loss through ionizations and excitations. Excitations consist in a transition of the orbital electron from its allowed orbit to a higher energy outer shell and require energies of a few eV only whereas in ionizations the orbital electron is ejected. In both cases, when the atom returns to its original state, it emits a characteristic x-ray. Rarely, Čerenkov radiation can also be released due to the polarization of the medium by fast electrons. When the energy transferred to the orbital electron overcomes the binding energy of the orbital electron, the latter is ejected, follows its own track as a δ-*ray* and carries away energy at a significant distance from the primary particle's track, leading to subsequent ionizations and excitations.

2.1.1.b Radiative interactions

Finally, the last type of energy loss occurs when the incident electron interacts with the Coulomb field of the atom's nucleus (*i.e.* when $b<a$). The incident electron is then usually deflected but in 2% of the cases, braking radiation or *bremsstrahlung* is emitted by the deceleration of the electron. Larmor wrote a relationship quantifying the

power P emitted by bremsstrahlung as a function of the speed of light c, the particle's charge q and acceleration a,

$$P = \frac{dE}{dt} = -\frac{q^2 \cdot a^2}{6\pi\varepsilon_0 c^3}. \tag{2.1}$$

According to Newton's second equation of motion along with Coulomb's law, the acceleration is proportional to the ratio of the atomic number of the medium over the mass of the incident charged particle. Therefore, bremsstrahlung occurs in a significant manner only for light charged particles such as electrons and positrons. Radiative interactions are also negligible in low Z media. Although bremsstrahlung photons can theoretically leave with energy between zero and the total energy of the incident photon, most of them leave with a low energy. As the angular distribution of bremsstrahlung emission is proportional to $sin^2 \theta / (1 - \beta \cdot cos^2 \theta)^5$, where θ is the angle between the acceleration of the charged particle and a unit vector connecting the charge with the point of observation, the direction of photon emission is normal for low energy photons like x-rays produced in an x-ray tube and forward for high energy photons like the one produced in a linac's target. Bremsstrahlung photons can then undergo their own interactions through photoelectric effect, Rayleigh and Compton scatter and pair production, the probability of each interaction depending mostly on the photons' energy and the atomic number of the medium. To be mentioned also is the rare possibility of γ-ray creation by annihilation of a positron with an electron in flight or at rest.

2.1.1.c Quantification of the energy loss with the stopping power

The average rate of kinetic energy dE lost by charged particles per unit path length dx defines the total mass stopping power, $(S/\rho)_{tot}$,

$$\left(\frac{S}{\rho}\right)_{tot} = \frac{1}{\rho}\frac{\overline{dE}}{dx} \quad \text{in} \quad \left[\frac{MeV \cdot cm^2}{g}\right]. \tag{2.2}$$

The division by the medium physical density ρ eliminates the dependence of the stopping power on the medium density, except for a small contribution due to the density effect. In the total mass stopping power, the collisional and radiative components are generally separated,

$$\left(\frac{S}{\rho}\right)_{tot} = \left(\frac{S}{\rho}\right)_{coll} + \left(\frac{S}{\rho}\right)_{rad} . \qquad (2.3)$$

This distinction is useful since these two sources of energy loss are effective at different locations, the energy lost by ionization being deposited close to the primary particle track whereas radiative interactions produce mass-less photons carrying energy far away from the interaction site. Moreover, radiative and collisional stopping powers depend differently on the medium atomic number and the particle's kinetic energy, as illustrated by Figure 2.2.
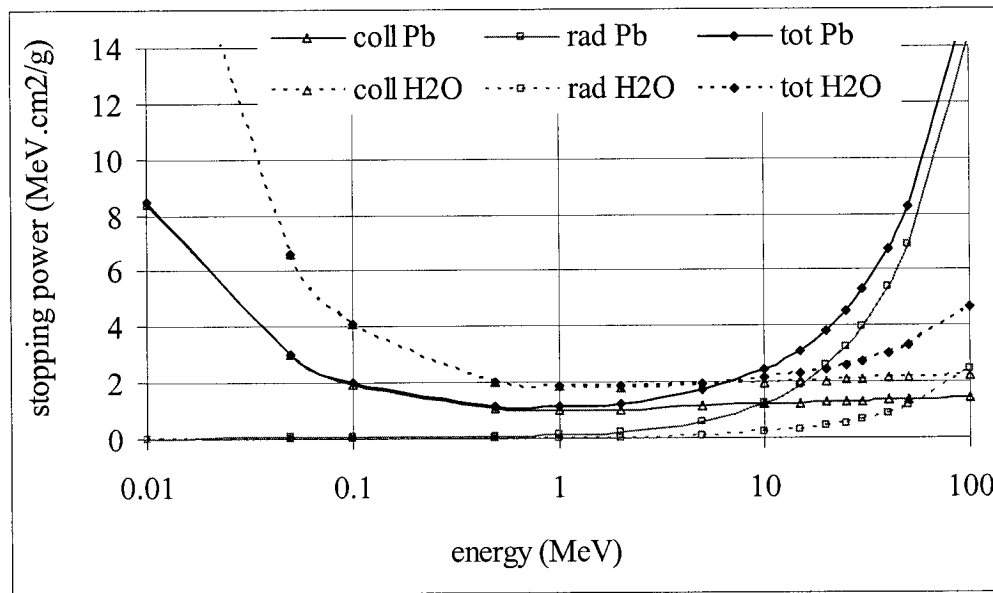
Figure 2.2: Plot of the collisional, radiative and total unrestricted stopping powers as a function of incident particle energy for water (Z=7.51) and lead (Z=82) according to data tabulated in ICRU 37[1].

> ➤ **Collisional stopping power**

In a collision, an electron transfers some of its kinetic energy to the orbital electron it interacts with. By convention, the maximum amount of energy that an electron can transfer to another electron is half its kinetic energy. In other words, the projectile will always leave the interaction site faster than the electron that it ejected if ionization even occurred. Berger and Seltzer[1] proposed a general expression for the collisional mass stopping power, $(S/\rho)_{coll}$,

$$\left(\frac{S}{\rho}\right)_{coll} = \frac{N_A.Z}{A}\left[\int_{W_0}^{W_c}\frac{d\sigma}{dW}W.dW + \int_{W_c}^{W_m}\frac{d\sigma}{dW}W.dW\right], \quad (2.4)$$

where N_A is the Avogadro number, Z and A are the atom and mass numbers of the medium, $d\sigma/dW$ is the differential cross-section for an inelastic collision resulting in an energy transfer W, W_0 is the binding energy of the atom, W_m is the maximum energy transfer possible and W_c is the smallest energy transfer allowing for emission of δ-rays. In other words, the cut-off energy W_c is the threshold separating soft collision from hard collisions. The first term of Equation 2.4 has been further developed by Bethe and Heitler[2] in the frame of quantum mechanics as,

$$\left(\frac{S}{\rho}\right)_{coll}(W \le W_c) = \frac{2\pi r_e^2 m_0 c^2 N_A}{\beta^2}\frac{Z}{A}\cdot z^2 \cdot \ln\left[\frac{2m_0 c^2\beta^2 W_c}{(1-\beta^2)I^2} - \beta^2\right], (2.5)$$

under the Born approximation, where the velocity of the incident electron overcomes by far the rotation velocity of the orbital electron in its shell. In this Equation 2.5, r_e is the classical electron radius of 2.82 fm, $m_0 c^2$ is the electron rest mass energy, β is the relativistic ratio of particle velocity v to the speed of light c, z is the charge of the incident particle and I is the mean excitation energy. This last quantity I represents the average energy required in a collision to modify the energy level of the orbital electrons in the medium. It is obtained in the first order by the empirical expression

$$I \approx 11.5\,(eV).Z \quad \text{in}\,[eV]. \quad (2.6)$$

The hard collision term derived from Møller cross section for electrons[3] and Bhabba cross section for positrons[4] added to Equation 2.5 results in the following expression for the mass collision stopping power for electrons and positrons,

$$\left(\frac{S}{\rho}\right)_{coll} = \frac{2\pi r_e^2 m_0 c^2 N_A}{\beta^2}\frac{Z}{A}\cdot\left[\ln\left(\frac{T^2}{I^2}\cdot\left(1+\frac{\tau}{2}\right)\right) + F^{\pm}(\tau) - \delta\right], (2.7)$$

where T is the incident particle kinetic energy, τ is the particle's energy in units of rest energy, δ is the density effect, and the F^- expression for electrons is given as,

$$F^-(\tau) = (1-\beta^2)\cdot\left[1+\frac{\tau^2}{8}-(2\tau+1)\cdot\ln 2\right]. \quad (2.8)$$

The density effect is a consequence of the polarization of the medium by the passage of a charged particle, which weakens the Coulomb field exerted by a given atom on its distant

counterparts and thereby reduces the stopping power. This effect, which increases with energy, is significant at energies above the rest mass energy of the incident particle and in dense materials, hence its denomination. Equation 2.7 highlights the dependence of the stopping power on the charge and energy of the incident particle, the independence on the particle's mass. Indeed, the stopping power first drops with increasing incident kinetic energy up to about three times the electron rest mass energy, where it reaches a plateau of 2 MeV.cm^2/g and slowly rises again. Furthermore, the stopping power shows a slow dependence on the atomic number of the medium. A shell correction can also be included in Equation 2.7 in order to correct the stopping power for the Born approximation, it is equal to 1% in the radiotherapy energy range and hence usually omitted, but it becomes significant at low electron energies.

> **Radiative stopping power**

Bethe and Heitler wrote the mass radiative stopping power as,

$$\left(\frac{S}{\rho}\right)_{rad} = \frac{1}{137} r_e^2 \frac{N_A Z^2}{A} (T + mc^2)\overline{B_r}, \qquad (2.9)$$

where B_r is a function varying slowly with energy from 16/3 for energies below 0.5 MeV to 15 for energies above 100 MeV[5]. The radiative stopping power has a quadratic dependence on Z and becomes therefore important for materials with high atomic number, as appears in Figure 2.2.

> **Restricted stopping power**

For calculation of dose deposited locally, energetic secondary particles that carry some energy away from the point of interest have to be excluded. Thus, the restricted collision stopping power is defined as the collision stopping power excluding energy transfers above a given threshold Δ. The choice for a threshold depends on the type of problem and it is typically set to 10 keV for gas filled ionization chambers. The restricted collision stopping power can be written as[1],

$$\frac{L^{\pm}}{\rho}(T,\Delta) = \frac{2\pi r_e^2 m_0 c^2 N_A}{\beta^2} \frac{Z}{A} \cdot \left[\ln\left(\frac{T^2}{I^2} \cdot \left(1 + \frac{\tau}{2}\right)\right) + G^{\pm}(\tau,\eta) - \delta \right], \qquad (2.10)$$

where $\tau = T/m_0 c^2$, $\eta = \Delta/T$ and G^- for electrons is

$$G^{-}(\tau,\eta) = -1 - \beta^2 + \ln[4\eta(1-\eta)] + (1-\eta)^{-1} + (1-\beta^2)[(2\tau+1)\ln(1-\eta) + \tau^2\eta^2/2]. \quad (2.11)$$

> **Range**

The range of a particle is the expectation value of the pathlength it follows until it comes to rest. The projected range is the expectation value of the farthest point of penetration of the particle in its initial direction. Under the assumption that the energy is lost gradually or Continuous Slowing Down Approximation (CSDA), the range R_{CSDA} of an electron of initial kinetic energy T_0 varies inversely with the total unrestricted stopping power S_{tot} as,

$$R_{CSDA} = \int_0^{T_0} \frac{dT}{S_{tot}(T)}. \quad (2.12)$$

The value of the range is strongly affected by processes of multiple scattering and energy straggling. The various concepts of ranges are illustrated in Figure 2.3.
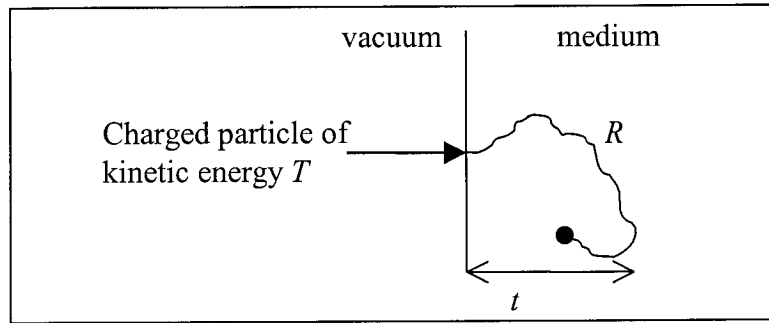
Figure 2.3: Illustration of the notion of range and projected range.

2.1.2 Scattering processes

A 10 MeV electron typically undergoes 100 000 interactions before coming to rest. Amongst these, hard collisions and nuclear Coulomb scattering in particular induce many small angle deflections, requiring statistical treatment of the scattering process. Scattering is analyzed by considering single scattering which results in a large angular deflection or multiple scattering involving numerous small-angles deflections.

2.1.2.a Scattering interactions

Deflections in the path of an electron can be caused by its interaction either with the Coulomb field of a nucleus or with the orbital electron of the medium. The probability P of scattering through an angle θ into an element of solid angle Ω is related to the density N of scattering centers (*i.e.* nuclei) per unit volume and the thickness x of the medium traversed through the differential cross-section for nuclear elastic scattering $d\sigma/d\Omega$ as,

$$P(\theta)d\Omega = \frac{d\sigma}{d\Omega} Nx \, d\Omega , \qquad (2.13)$$

with the cross-section expressed ignoring the finite nuclear size, the electron spin and screening of electrons, using the Rutherford formula as,

$$\frac{d\sigma}{d\Omega} = \frac{\pi e^4 Z^2}{2 m_0 v^4} \frac{\sin\theta}{\sin^4(\theta/2)} . \qquad (2.14)$$

For an electron of momentum p and speed relative to the speed of light β, traversing a thickness dx, the probability for nuclear scattering was written by Rossi[6] for small non-zero deflections as

$$P(\theta)d\Omega = 4\frac{NZ^2}{A} r_e^2 \left(\frac{mc}{\beta p}\right)^2 \frac{d\Omega}{\theta^4} . \qquad (2.15)$$

Practically, electron-electron scattering is responsible for all energy losses. Møller[3] wrote the differential cross section for scattering of electrons with orbital electrons considered free as,

$$\frac{d\sigma}{df} = 2\pi r_e^2 \frac{(T+1)^2}{T^2(T+2)} \left[\frac{1}{f^2} - \frac{1}{f(1-f)}\frac{2T+1}{(T+1)^2} + \frac{1}{(1-f)^2} + \frac{T^2}{(T+1)^2} \right], \qquad (2.16)$$

where T is the sum of the kinetic energies of the two electrons in electron rest mass units, f is the fractional kinetic energy of the electron with lowest energy.

2.1.2.b Quantification by the scattering power

The angular and spatial spread of a pencil electron beam scattering through matter are approximately Gaussian. The net angle resulting from multiple scattering is usually small. The mean square scattering angle, recommended by the ICRU report 21[7] to

describe the angular scattering power of a material, conveniently expresses the multiple scattering of an electron along a pathlength l in an absorber of density ρ as[6]

$$\frac{\overline{\theta^2}}{\rho l} = 16\,\pi N_A \frac{Z^2}{M_a} r_e^2 \left(\frac{m_0 c^2}{\beta pc}\right)^2 \log\left[196\,Z^{-1/3}\left(\frac{Z}{A_r}\right)^{1/6}\right]. \tag{2.17}$$

Moreover, the ICRU defines the mass scattering power T of a material of mass thickness ρl as,

$$\frac{T}{\rho} = \frac{1}{\rho}\frac{d\overline{\theta^2}}{dl}. \tag{2.18}$$

From Equations 2.17 and 2.18, it appears that the mass scattering power varies approximately as the inverse square of the electron kinetic energy and the square of the atomic number of the absorber, which, for example, helps determining the material for the scattering foils of a linac operating in the electron mode.

2.1.2.c Multiple scattering theory

The complex problem of electron multiple scattering has been approached by Moliere[8] and Goudsmit and Saunderson[9] who treated the angular distribution regardless of the lateral displacement and neglected the energy losses in the frame of single elastic scattering. Earlier, Fermi[10] applied the multiple scattering theory to multiple small scattering angles and forward scattering. Eyges[11] extended Fermi's theory to include the effects of energy degradation. Bruinvis[12] further extended the theory to include electron range straggling. A mean square scattering angle has been defined[10] to quantify the deflections for single scattering events as,

$$\overline{\theta^2} = \frac{\int\limits_0^{\theta_{max}} \theta^2 \left(\frac{d\sigma}{d\Omega}\right)_{eff} d\Omega}{\int\limits_0^{\theta_{max}} \left(\frac{d\sigma}{d\Omega}\right)_{eff} d\Omega}, \tag{2.19}$$

where $(d\sigma/d\Omega)_{eff}$ is the effective differential cross-section for scattering by elastic nuclear scattering and by hard collisions and θ_{max} is the maximum scattering angle in an interaction between an incident electron and the nucleus. The net scattering angle of an electron is deduced statistically from the single scattering angles having occurred on its path.

2.2. Dosimetry of clinical electron beams

This section first describes the concepts underlying electron dosimetry and summarizes the cavity theory which relates some of these concepts. The dosimetric characteristics of electron beams are then explained in a third section, followed by a special emphasis on the available methods for determination of electron beam cutout factors. Finally, the principle of dosimeters relevant to this work is summarized.

2.2.1. Dosimetric quantities

The non-stochastic quantity of particle fluence Φ is defined as the expectation value of the number of events N scored in a sphere of area da per unit area, while the energy fluence Ψ is the expectation value of the total kinetic energy carried by all $<N>$ particles E_K scored in a sphere of area da per unit area, or,

$$\Phi = \frac{d\langle N \rangle}{da} \quad \text{and} \quad \Psi = \frac{d\langle E_K \rangle}{da}. \tag{2.20}$$

In macrodosimetry, the dose D is defined as the net average energy ϵ imparted to medium per unit mass of tissue dm,

$$D = \frac{d\langle \epsilon \rangle}{dm} \quad \text{in [Gy] where } 1\,\text{Gy} = 1\,\text{J/kg}. \tag{2.21}$$

The absorbed dose is related to the differential electron fluence spectrum $d\Phi/dT$ through the unrestricted mass collisional stopping power $(S/\rho)_{coll}$ as,

$$D = \int_A^{T_0} \frac{d\Phi(T)}{dT} \left(\frac{S(T)}{\rho} \right)_{coll} dT, \tag{2.22}$$

where A and T_0 delimit the energy range of the electron fluence spectrum in the volume where the dose is scored.

2.2.2 Cavity theory

The reading of a dosimeter placed in a medium is related to the dose absorbed by the detector in its own material, which in the common cases of gas filled ionization chamber or thermoluminescent dosimeter is significantly different from the surrounding medium. The cavity theory bridges the gap between the dose absorbed by the detector

placed in the medium and the dose that would have been absorbed in the medium in absence of the detector in a volume equal to that of the detector's effective volume.

For a particle fluence constant through the scoring volume under charged particle equilibrium, the absorbed dose and the particle fluence for two media are related through,

$$D_{med1} = \Phi_{med1} \left(\frac{\overline{S}}{\rho} \right)_{coll,\ med1} \quad \text{and} \quad D_{med1} = \Phi_{med2} \left(\frac{\overline{S}}{\rho} \right)_{coll,\ med2} , \quad (2.23)$$

hence,
$$\frac{D_{med1}}{D_{med2}} = \frac{\Phi_{med1}}{\Phi_{med2}} \frac{(\overline{S}/\rho)_{coll,\ med1}}{(\overline{S}/\rho)_{coll,\ med2}} . \quad (2.24)$$

Equation 2.24 can be applied to the case where a small cavity is introduced into a medium under charged particle equilibrium, this is the objective of the Bragg-Gray cavity theory[13-15].

2.2.2.a Bragg-Gray cavity theory

Assuming that the cavity is small compared to the range of the charged particles crossing it, so that the cavity does not perturb the fluence (*i.e.* $\Phi_{med}=\Phi_{cav}$) and assuming that the dose in the cavity is uniquely deposited by the charged particles crossing it, the conversion of the dose in the cavity to the dose in the medium is simply given by the ratio of stopping powers by simplification of Equation 2.24,

$$\frac{D_{med}}{D_{cav}} = \frac{(\overline{S}/\rho)_{coll,\ med}}{(\overline{S}/\rho)_{coll,\ cav}} . \quad (2.25)$$

However, this relation neglects the contribution of secondary electrons created as the primary electron slows down. Spencer-Attix cavity theory extends Bragg-Gray theory to account for these.

2.2.2.b Spencer-Attix cavity theory

Under the same assumptions that define a Bragg-Gray cavity, except that secondary charged particles are now included in the fluence, Spencer and Attix[16] define an energy threshold Δ, equal to the energy of an electron whose range equals the mean chord length of the cavity. This threshold therefore differentiates between slow electrons depositing their dose locally and thus not contributing to the dose, and fast electrons able

to cross the cavity and deposit energy in the cavity. The conversion of the dose in the cavity to the dose in the medium becomes then,

$$\frac{D_{med}}{D_{cav}} = \frac{\int_{\Delta}^{T_0} (d\Phi^{\delta}/dT)_{med} \, (\overline{L_{\Delta}}(T)/\rho)_{med} \, dT + TE_{med}}{\int_{\Delta}^{T_0} (d\Phi^{\delta}/dT)_{med} \, (\overline{L_{\Delta}}(T)/\rho)_{cav} \, dT + TE_{cav}} \approx \frac{(\overline{L_{\Delta}/\rho})_{coll,\ med}}{(\overline{L_{\Delta}/\rho})_{coll,\ cav}}, \quad (2.26)$$

where $d\Phi^{\delta}/dT$ is the differential electron fluence spectrum including the secondary particles, L_{Δ} is the collisional stopping power restricted to the energy threshold Δ and TE is a track- end term defined by Nahum[17] to account for the energy deposition occurring at the end of the particle track. To account for the differences in fluence, a fluence perturbation correction factor, P_{cav}^{med}, is introduced in Equation 2.26 which becomes,

$$\frac{D_{med}}{D_{cav}} = \frac{(\overline{L_{\Delta}/\rho})_{coll,\ med}}{(\overline{L_{\Delta}/\rho})_{coll,\ cav}} P_{cav}^{med} (z). \quad (2.27)$$

P_{cav}^{med} is greater at low energies and for larger detectors. Its importance also depends on the atomic number and physical density of the cavity material relative to the medium for solid state detectors[18].

2.2.3. Electron beam characteristics

Useful plots are the central-axis relative ionization as a function of depth or percent depth ionization (PDI) and the central-axis relative dose as a function of depth or percent depth dose (PDD); PDI and PDD are normalized to their respective maximum values. The electron PDD starts with a high surface dose followed by a small build-up, then the dose falls off steeply until a plateau at a few percent of the maximum dose is reached; the bremsstrahlung tail consisting uniquely of photons. A few quantities of interest are defined on the electron PDD, as illustrated in Figure 2.4: z_{max} the depth of maximum dose, R_{90} depth of 90% dose called therapeutic range since it is used as the depth for dose prescription by radio-oncologists and for choice of beam nominal energy, R_{50} the depth of 50% dose used for beam characterization and finally R_p the practical range located at the depth of intersection of the slope of the PDD fall-off and of the bremsstrahlung tail.
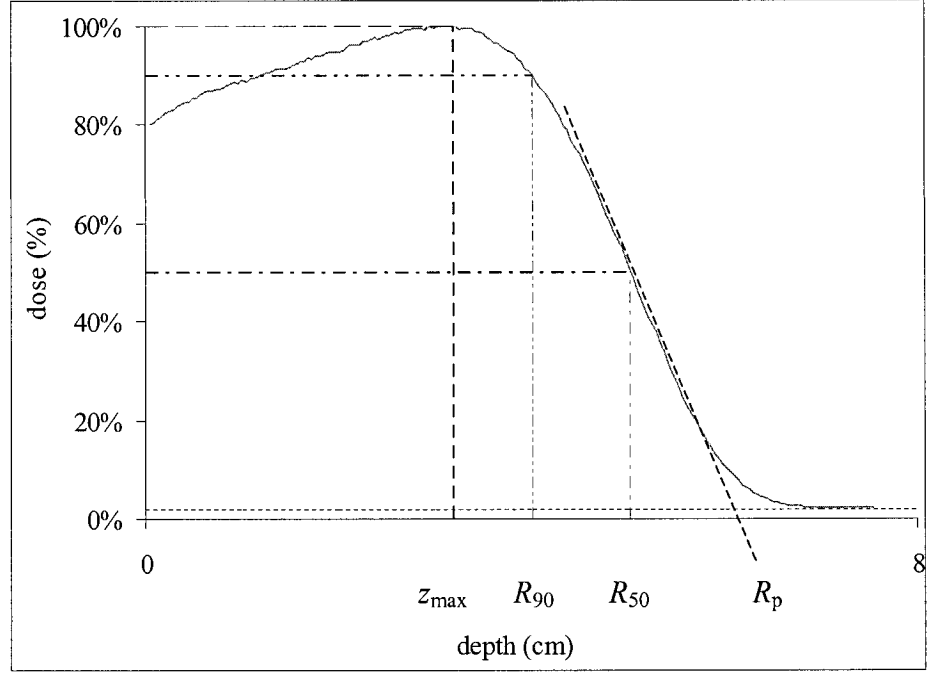
Figure 2.4: PDD of CL2300's 12 MeV electron beam with 10x10 cm² field size (SSD=100 cm).

2.2.3.a Energy specification

The energy of an electron beam can be specified in many ways. Amongst these, the nominal energy is the energy of the pencil beam impinging on the accelerator exit window as specified by the manufacturer. The most probable energy[7] at a given depth z, $E_{p,z}$, , and the mean energy at a given depth z, $\overline{E}z$, are both related to the practical range through Harder's relation[19],

$$E_{p,z} = E_{p,0} \cdot (1 - \frac{z}{R_p}) \quad \text{and} \quad \overline{E_z} = \overline{E_0} \cdot (1 - \frac{z}{R_p}), \qquad (2.28)$$

where $E_{p,0}$ the most probable energy at the surface and $\overline{E_0}$ mean surface energy, both expressed in MeV, can be determined respectively from the practical range R_p and the depth of 50% dose R_{50}, both expressed in cm, using the equations[20-22]

$$\overline{E_0} = 2.33 \ R_{50} \quad \text{or} \quad \overline{E_0} = 0.656 + 2.059 \ R_{50} + 0.022 \ R_{50}^2$$

$$\text{and} \quad E_{p,0} = 0.22 + 1.98 \ R_p + 0.01025 \ R_p^2 . \qquad (2.29)$$

24

2.2.3.b Energy dependence

The electron PDD depends on the energy of the incident beam as illustrated in Figure 2.5. The higher the energy, the higher the surface dose, the less steep the dose fall-off, the further R_{50} and R_p, the larger the bremsstrahlung tail. The dose contribution of bremsstrahlung photons ranges from 1% for 6 MeV to 6% for 22 MeV. The dose build-up for electrons is not only triggered by creation of secondary electrons as in the case of photon beams, but mainly by the increasing mean square scattering angle of the beam as it goes further in the medium, which comes down to an increase in the practical electron fluence. Low energy electron beams therefore exhibit a greater build-up, because scattering increases at lower energy. Another energy dependent characteristic is the depth of maximum dose. Indeed, as the energy increases, the depth of maximum dose first increases then slowly decreases. On the one hand, direct electrons with higher energy deposit their dose deeper on the central axis of the phantom, but on the other hand, the contribution of electrons scattered from the linac's head with the electron applicator is increasingly important at the surface as energy increases.
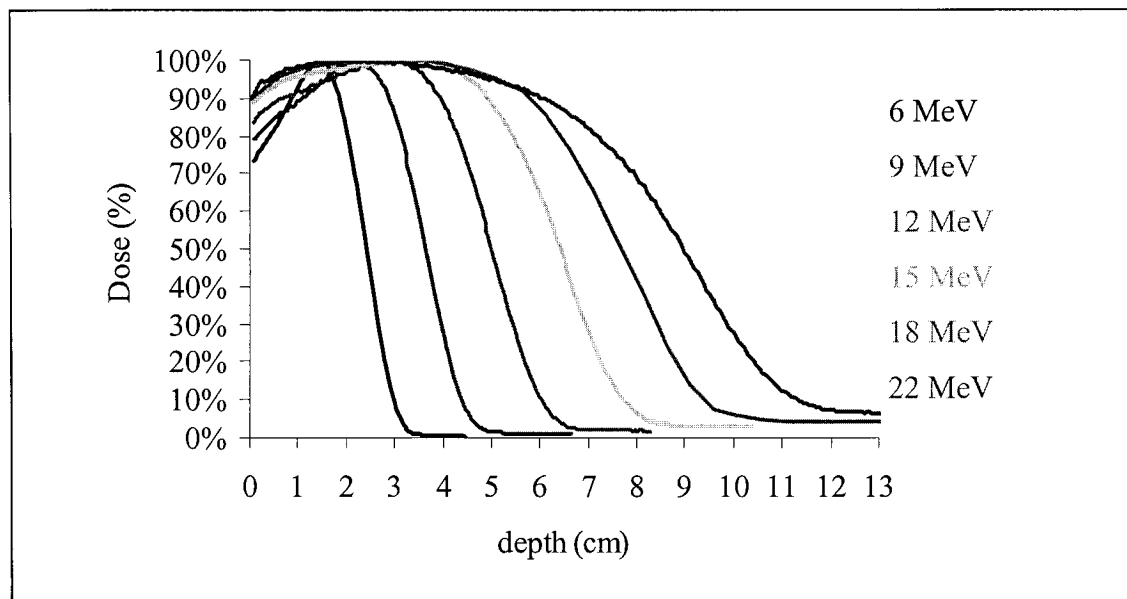
Figure 2.5: PDD for electron beams of 10x10 cm² field size at SSD=100 cm for all energies of the CL2300 C/D measured with a p-Si diode.

2.2.3.c Field dependence

The electron PDD also depends on the field size, as illustrated in Figure 2.6. For any field whose half dimension is larger than the range of laterally scattered electrons, the PDD looks similar due to lateral electronic equilibrium, where the electrons are entering and leaving the volume of interest in equal numbers. However, for fields whose half dimension is smaller than the range of laterally scattered electrons, lateral electronic equilibrium is disrupted and low energy electrons depositing their dose close to the surface become increasingly important, provoking the PDD to shift towards the surface as well as z_{max} and R_{90}. The surface dose also rises with narrower fields, because the electrons scattering out of the field are no longer compensated by in-scatter; indeed, irradiation does not extend to the regions where electrons with a range sufficient to scatter in, would originate from. The variation of PDD with field size is important for energies from 4 to 10 MeV and for fields with a dimension smaller than the initial energy divided by 2.5[23]. It is therefore useful to quantify the variation of the beam relative output factor as a function of the projected field size at a given source-to-surface distance (SSD) with the cutout factor, COF. According to TG-25[24], the cutout factor is defined as the ratio of the maximum central-axis dose for a given energy, field size and SSD over the maximum central-axis dose for the reference 10×10 cm^2 field at 100 cm for this energy,

$$COF(E,A,SSD) = \frac{D_{max}(E,A,SSD)/100\,\text{MU}}{D_{max}(E,10\times10\text{cm}^2,100\,cm)/100\,\text{MU}}. \qquad (2.30)$$

The COF is calculated on the central axis for centered cutouts, but for cutouts whose center is off-axis, the COF is measured along the vertical axis at the lateral position where the largest dose is deposited. Furthermore, the COF is usually measured at a SSD of 100 cm at which most electron beam treatments are given.

Furthermore, the electron PDD depends on the field shape. Harder[25] established formulas linking the dimensions of circular field of radius r and rectangular field of dimensions L and l to the side of an equivalent square field a_{eq},

$$a_{eq} = 1.792 \; r \quad \text{and} \quad a_{eq} = C \sqrt{Ll} \quad \text{for } L/l \leq 1.25 \;, \qquad (2.31)$$

with C=0.98 if L/l is small, C=0.93 if L/l=1.5 and C=0.84 if L/l=2.
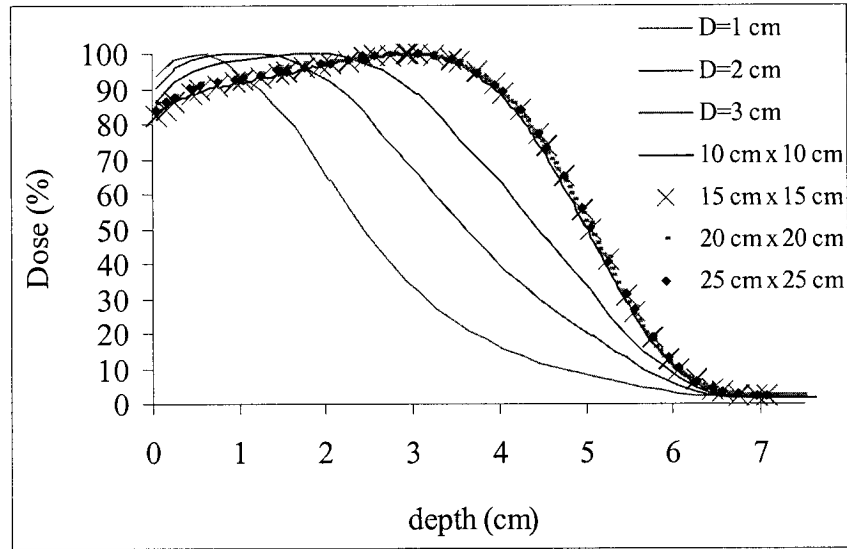
Figure 2.6: PDD for CL2300's 12 MeV electron beam for various field sizes at SSD 100 cm measured by the diode.

2.2.3.d Determination of electron beam cutout factors

Knowledge of the COF is necessary for all fields and systematic measurement can be time-consuming especially for small or irregular fields where the position of z_{max} is unknown. Therefore, active research has aimed at analytical determination of COF.

> ➤ **Empirical formula for regular fields**

Mills[26] first came up with a formula based on the multiple scattering theory expressing the COF for rectangular fields of dimension X×Y as the square root of the product of the measured COF of square fields of side X and Y,

$$COF\ (X,Y) = \sqrt{COF\ (X,X).COF\ (Y,Y)}.\qquad(2.32)$$

This "square-root method" produces results within 1% of the measured values for most fields. But, it overestimates the COF of large fields and does not account for the difference in the in-scatter originating from the X and Y jaws. The "1D method"[27] accounts for the jaws' asymmetry by using the measured COF of two rectangular fields, as

$$COF\ (X,Y) = COF\ (X,10).COF\ (10,Y) + CF\ (X,Y),\qquad(2.33)$$

where $CF(X,Y)$ is an empirical correction factor accounting for the difference in the collimator surface scattering electrons between the field of interest and the fields used for the calculation.

$$
\begin{aligned}
CF(X,Y) &= 0, \text{if } \Delta < 0 \\
CF(X,Y) &= C, \text{if } \Delta > 0 \\
\text{where } \Delta &= \sqrt{(X-10)(Y-10)}.
\end{aligned}
\tag{2.34}
$$

This approach is accurate within 1% except for large fields at lower energies and still requires a large amount of preliminary measurements. The "2D fit method"[28] provides a better fit over a wider range. It consists of optimized semi-empirical formula based on the multiple scattering theory,

$$
COF(X,Y) = k.erf\left(k_x \frac{X}{X_{ref}}\right).erf\left(k_Y \frac{Y}{Y_{ref}}\right) + \Delta\left(\frac{X}{X_{ref}}, \frac{Y}{Y_{ref}}\right),
\tag{2.35}
$$

where X_{ref} and Y_{ref} are the reference fields and Δ is a power series to correct for deviations from the measurements. All the above described methods apply to rectangular fields only. The rupture of the lateral electronic disequilibrium in small and irregular fields requires use of algorithms accounting more accurately for electronic interactions in order to determine cutout factors.

> ➤ **Algorithms**

For irregular fields, two routes have been followed: sector integrations and pencil beam-based algorithms.

Pencil-beam algorithms[29-31], although promising, do not predict COF very accurately for small or irregular fields. With the CadPlan pencil-beam algorithm based treatment planning system, Ding[32] *et al* obtained an agreement between calculated and measured cutout factors within 2% for large fields and 5% for small fields. Besides, CadPlan sets the upper limit for cutout factors to unity, which is inaccurate for fields where electrons scattered from the cutout contribute to the dose on the central axis.

Similarly to the Clarkson's method for photons[33], sector-integration methods[34-37] account for the lateral electronic disequilibrium, the change in electron fluence and the scatter from the edge of the cutout. Overall, these techniques provide results within 1% of the measured data for convex fields, but fail for concave shaped fields.

Therefore, the Monte Carlo technique seems to be the best method to determine accurate values of COF for any irregular field. So far, its ability to predict electron beam output factors within 2%[38-40] has been established for regular fields.

2.2.4. Electron dosimetry techniques

Dosimetry relies on two types of detectors: reference dosimeters capable of measuring the dose in absolute terms, and relative dosimeters. Relative dosimeters can measure the relative dose at points different from the reference point or the absolute dose after cross-calibration against an absolute dosimeter. The basic principles underlying the dosimeters used in this project are briefly described below.

2.2.4.a Ionization chambers

Gas-filled ionization chambers are the most commonly used dosimeters in radiotherapy thanks to their stability and precision. They are used under two main designs, cylindrical used for photon beams and high energy electron beams and parallel-plate recommended for low energy electron beams (below 12 MeV). The schematic design of a parallel-plate ionization chamber is illustrated in Figure 2.7.

The principle of the ionization chamber is based on collection by polarized measuring electrodes of the ions produced by interaction of the gas molecules with the primary and secondary electrons of the beam entering the sensitive volume of the chamber. The collected particles flow in a current i_+ or i_- depending on the sign of the polarization voltage. An electrometer provides the polarising high voltage to the electrodes and records the current or cumulated charge. The magnitude of the integrated charge Q is proportional to the dose absorbed by the cavity gas,

$$D_{gas} = \left(\frac{W}{e}\right)_{gas} \left(\frac{Q}{m_{gas}}\right)$$

(2.36)

where $(W/e)_{gas}$ = 33.97 eV/ion pair is the average energy required to release one ion pair in air and m_{gas} is the mass of gas in the chamber cavity, which is determined by calibration of the chamber in a reference Cobalt beam.

The role of the guarding electrodes is to deviate from the main current flow the leakage currents stemming from the contamination of insulators and to define the

collecting volume of the chamber. The signal increases with polarising voltage until saturation is reached when all ions are collected. The voltage is typically set so that the chamber operates at or near saturation. The sign of the polarising voltage has an impact on the measured reading. Indeed, a small "Compton" current i_C stems from photonic and electronic interactions with the collecting electrode and cables. In order to clear the effect of the Compton current, the true signal is taken as the average of the signal measured under a positive voltage I_+ and the signal measured under a negative voltage I_-, where

$$I_+ = i_+ + i_C \text{ and } I_- = i_- - i_C \text{ hence } i_+ = i_- = \frac{I_+ + I_-}{2} \qquad (2.37)$$
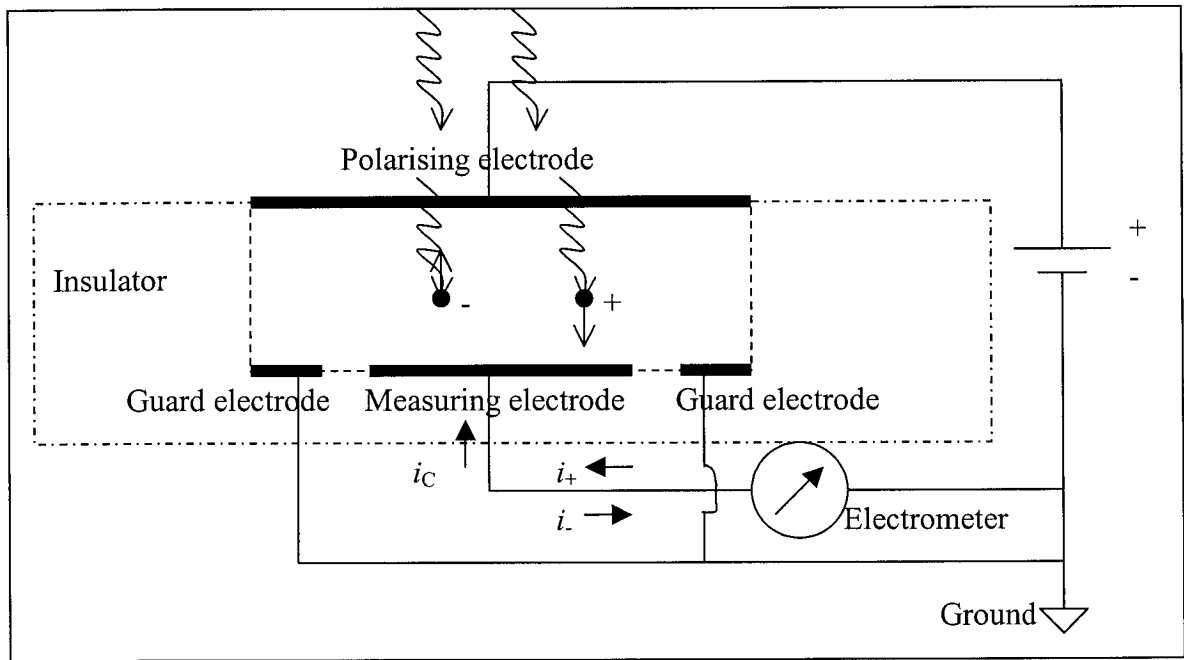
Figure 2.7: Schematics of a parallel-plate ionization chamber.

2.2.4.b Semi-conductors

Semi-conductor dosimeters are miniature silicon transistors called Metal-Oxyde Semiconductor Field Effect Transistor (MOSFETs) and diodes. Silicon diodes consist of a p-n junction diode. A strong electric field is established in the narrow transition zone between the p-type and n-type layers called the depletion zone. This depletion region is present even in the absence of a biasing voltage. Electron-hole pairs created by ionizing

radiation are therefore rapidly collected due to the electric field. In other words, irradiation of a semiconductor creates a current, collected by an electrometer.

A p-Si diode dosimeter has a p-type silicon and a counter-doped surface as in p-type diodes; their small dark current, small dimensions, high sensitivity (20 000 times larger than that of air-filled ionization chambers with the same collecting volume[23]) and favourable signal-to-noise ratio make them suitable detectors for dosimetry, particularly of clinical electron beams. Used without biasing voltage and in the short circuit mode, they provide a signal proportional to the dose, independently of the dose rate. Moreover, the relative ionization signal they provide can be taken directly as the relative dose, due the limited variation of the silicon-to-air stopping power ratio with depth for broad electron beams[41]. However, they can only be used as relative dosimeters because their sensitive volume is not well known and because their sensitivity changes with temperature and with repeated use due to radiation damage.

2.2.4.c Thermoluminescent dosimeters

Many crystals exhibit a thermoluminescent behaviour. This process is summarized in Figure 2.8. Indeed, crystals present allowed bands (valence and conduction) separated by a forbidden gap, due to their energy structure in discrete levels. Irradiation ejects an electron from the valence band into the conduction band. The subsequent hole in the valence band and electron in the conduction band travel respectively until they recombine or fall in a metastable state or trap. Such traps are usually artificially introduced in the crystal to enhance the thermoluminescence feature. Heat can then provide with the necessary energy for the trapped electron or hole to reach a thermoluminescence center and this transition releases radiation called thermoluminescence (TL). The probability of recombination is proportional to $e^{-E/kT}$ where E is the activation energy for the trap in Joules, T is the temperature in degrees Kelvin, and k is the Boltzmann constant (1.38×10^{-23} J/K). The emitted light can then be collected by a photomultiplier tube that converts the visible light into an electrical current that is further amplified and recorded.

The plot of the TL signal as a function of heating time is called *glow curve*, an example of which is shown in Figure 2.9. The integral of the TL signal as a function of

time is proportional to the dose absorbed by the detector. The glow curve typically exhibits a few peaks corresponding to the trapped energy levels. The peaks with short half-life such as peak 1 and 2 in Figure 2.9 (10 minutes and 10 hours respectively) are not suitable for dosimetry, hence the need of specific post-irradiation annealing to reduce the fading of those low-temperature electron traps without a significant effect on the main dosimetry peaks.
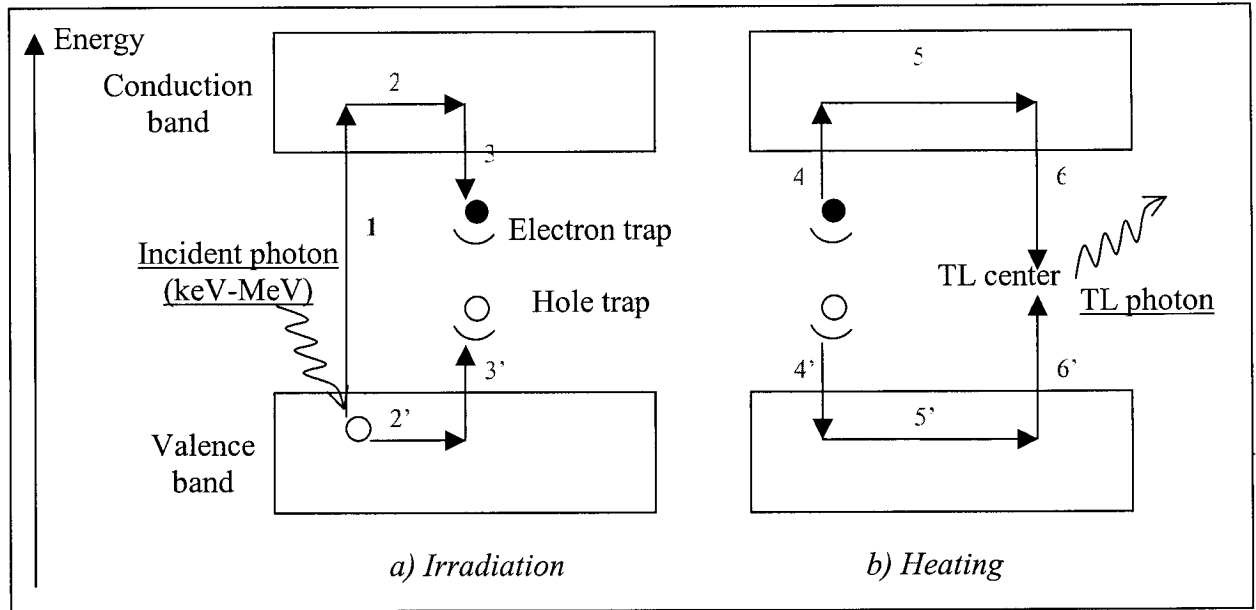
Figure 2.8: Model for thermoluminescence[42]. The full circles represent electrons and the empty circles represent holes.
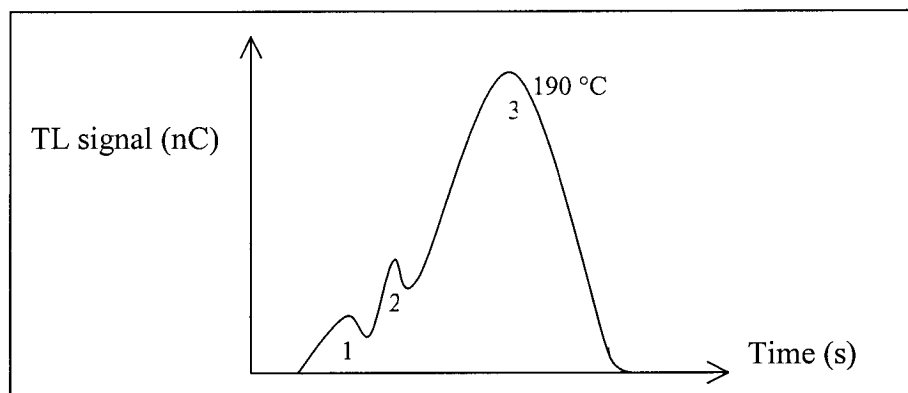
Figure 2.9: Characteristic glow curve of lithium fluoride[43].

The main advantage of TL as dosimeters is the relatively large signal emitted per unit mass for TLD, which allows the use of very small TLD chips near heterogeneities and in steep dose gradients where a high resolution is required. Literature presents conflicting results about the energy dependence of TLD. However, consensus is reached on the fact that the energy dependence of TLDs is critical for orthovoltage photon beams and high energy electron beams[44,45] with a signal for energies below 3 MeV 13% smaller than at energies above 25 MeV[46]. In other terms, the maximum variation in sensitivity with depth for LiF-100 is 5% in 5 MeV electron beams and 1% in 20 MeV[47], the energy dependence decreasing with the TLD size[48]. Despite the dependence of the TLD response on the energy of the electron beam, and the decrease of energy with depth in the phantom, an accuracy of a few percent[49] can be achieved in the acquisition of a complete depth-dose curve with TLDs. Moreover, the largest error occurs in the region of dose fall-off, since the expected larger error at depths close to the practical range of the electrons is compensated by a higher contribution of bremsstrahlung photons to the total electron dose.

Amongst the various types of phosphors available, noteworthy are lithium fluoride (LiF) doped with magnesium, lithium borate $Li_2B_4O_7$, calcium fluoride CaF_2, available under the form of powder or hot pressed chips or rods. The alkali halide LiF has been estimated[21] suitable for reproducible and accurate *ex* and *in vivo* dosimetry with its linear dose response at occupational dose levels, its wide useful dose range (10 μGy-10 Gy) and its non-dependence on dose rate. LiF has a physical density of 2.64 g/cm^3 and an atomic number of 8.2 close to that of tissue (7.64). Its main glow peak occurs at 195°C. It emits photons with wavelengths of the order of 3500-6000Å. Some drawbacks are the complicated annealing behaviour and relatively poor sensitivity.

References:

[1] ICRU, "Stopping Powers for Electrons and Positrons", ICRU Report No. 37, International Commission on Radiation Units and Measurements, Washington, D.C. (1984)

[2] H. Bethe, W. Heitler, "On the stopping of fast particles and on the creation of positive electrons", Proc. Roy. Soc. **A146**, 83-112 (1934)

[3] C. Møller, "Zur Theories des Durchgangs schneller Elektronen durch Materie", Ann. Phys. **14**, 568-577 (1932)

[4] H. J. Bhabba, "The scattering of positrons by electrons with exchange on Dirac's theory of the positron", Proc. Roy. Soc. **A154**, 195-206 (1936)

[5] F.H. Attix, *Introduction to Radiological Physics and Radiation Dosimetry*, (John Wiley & Sons, New York, 1986)

[6] B. Rossi, *High energy particles*, Englewood Cliffs NJ, Prentice Hall (1952)

[7] ICRU, "Radiation dosimetry: Electrons with initial energies between 1 and 50 MeV", ICRU Report No. 21, International Commission on Radiation Units and Measurements, Washington, D.C. (1972)

[8] G. Moliere, "Theorie der Streuung schneller geladener Teilchen II: Mehrfach-und Vielfachstreuung," Z. Naturforsch. **3a**, 78 (1948)

[9] S. Goudsmit, J.L. Saunderson, "Multiple Scattering of Electrons," Phys. Rev. **57**, 24 (1940)

[10] E. Fermi (1940) in B. Rossi, K. Greisen, "Cosmic ray theory", Rev. Mod. Phys. **13**,265-268 (1941)

[11] L. Eyges, "Multiple scattering with energy loss", Phys. Rev. **74**, 1534-1535 (1948)

[12] I. A. D. Bruinvis, W. A. Mathol, P. Andreo, "Inclusion of electron range straggling in the Fermi-Eyges multiple-scattering theory", Phys. Med. Biol. **34** (4), 491-507 (1989)

[13] W.H. Bragg, *Studies in radioactivity*, MacMillan and Co., London, (1912)

[14] L.H. Gray, "The absorption of penetrating radiation," Proc. Roy. Soc. **A122**, 647-668 (1929)

[15] L.H. Gray, "An ionization method for the absolute measurement of y-ray energy," Proc. Roy. Soc. **A156**, 578-596 (1936)

[16] L.V. Spencer, F.H. Attix, "A theory of cavity ionization," Rad. Res. **3**, 239-254 (1955)

[17] A. E. Nahum, "Water/air stopping-power ratios for megavoltage photon and electron beams", Phys. Med. Biol. **23**, 24-38 (1978)

[18] N. Mobit, G. A. Sandison, A. E. Nahum, "Electron fluence perturbation correction factors for solid state detectors in megavoltage electron beams: Monte Carlo simulations and experiments", Phys. Med. Biol. **45**(2), 255-265 (2000)

[19] D. Harder in *Symposium on High Energy Electrons (Montreaux)*, Eds A. Zuppinger and G. Poretti, Berlin, Springer, p260 (1965)

[20] NACP, "Electron beams with mean energies at the phantom surface below 15 MeV", Supplement to the recommendations of the Nordic Association of Clinical Physicists (1980), Acta Radiol. Oncol. Rad. Phys. **20**, 402-415, (1981)

[21] ICRU, "Radiation dosimetry: Electron beams with energies between 1 and 50 MeV" ICRU Report No. 35, International Commission on Radiation Units and Measurements, Bethesda, Maryland (1984)

[22] IAEA, "The Use of Plane Parallel Ionization Chambers in High Energy Electron and Photon Beams: An International Code of Practice for Dosimetry," Technical Report Series Vol. 381, International Atomic Energy Agency, Vienna (1997)

[23] S. C. Klevenhagen, _Physics of Electron Beam Therapy_, Medical Physics Handbooks 13, Adam Hilger Ltd, Bristol, England (1985)

[24] AAPM, "Clinical Electron-Beam Dosimetry", Task Group 25 Report, Med. Phys. **18**(1), 73-109 (1991)

[24] D. Harder, P. Schroder-Babo, A. Mandour, "Unified notation and fast computation of electron beam dose distributions", Private communication, (1982)

[25] M. D. Mills, K.R. Hogstrom, P. R. Almond, "Prediction of electron beam output factors", Med. Phys. **9**(1), 60-68 (1982)

[26] M. D. Mills, K.R. Hogstrom, R. S. Fields, "Determination of electron beam output factors for a 20-MeV linear accelerator", Med. Phys. **12**(4), 473-476 (1985)

[27] B. J. McParland, "A parametrization of the electron beam output factors of a 25-MeV linear accelerator", Med. Phys. **14**(4), 665-669 (1987)

[28] I. A. D. Bruinvis, A. Van Amstel, A. J. Elevelt, R. Van der Laarse, "Calculation of electron beam dose distributions for arbitrarily shaped fields", Phys. Med. Biol. **28**, 667-683 (1983)

[29] I. A. D. Bruinvis, W. A. F. Mathol, "Calculation of electron beam depth-dose curves and output factors for arbitrary field shapes", Radiother. Oncol. **11**, 395-404 (1988)

[30] B. J. McParland, "A method of calculating the output factors of arbitrarily shaped electron beams", Med. Phys. **16**(1), 88-93 (1989)

[31] G. X. Ding, J. E. Cygler, G. G. Zhang, M. K. Yu, "Evaluation of a three-dimensional electron beam treatment planning system", Med. Phys. **26** (12), 2571-2580 (1999)

[33] H. E. Johns, J. R. Cunningham, _The Physics of Radiology_, Ed C. C. Thomas, Springfield, Illinois, 1983

[34] F. M. Khan, F. C. Deibel, B. J. Gerbi, I. J. Das, "Dosimetry of irregularly shaped electron fields", Med. Phys. **14**, 473 (1987)

[35] D. Jones, P. Andre, J. T. Washington, M. D. Hafermann, "A method for the assessment of the output of irregularly shaped electron fields", Br. J. Radiol. **63**, 59-64 (1990)

[36] D. R. Choi, P. N. Mobit, K. E. Breitman, "The clinical implementation of a method for calculating the output factor and per cent depth dose for an electron beam", Phys. Med. Biol. **48**, 899-908 (2003)

[37] P. A. Jursinic, R. Mueller, "A sector-integration method for calculating the output factors of irregularly shaped electron fields", Med. Phys. **24**(11), 1765-1769 (1997)

[38] A. Kapur, C-M. Ma, E. C. Mok, D. O. Findley, A. L. Boyer "Monte Carlo calculations of electron beam output factors for a medical linear accelerator", Phys. Med. Biol. **43**, 3479-3494 (1998)

[39] G. G. Zhang, D. W. O. Rogers, J. E. Cygler, T. R. Mackie "Monte Carlo investigation of electron beam output factors versus size of square cutout", Med. Phys. **26** (5), 743-750 (1999)

[40] F. Verhaegen, C. Mubata, J. Pettingell, A. M. Bidmead, I. Rosenberg, D. Mockridge, A. E. Nahum "Monte Carlo calculation of output factors for circular, rectangular and square fields of electron accelerators (6-20 MeV)", Med. Phys. **28** (6), 938-949 (2001)

[41] AAPM, "AAPM's TG-51 protocol for clinical reference dosimetry of high energy photon and electron beams", Task Group 51 Report, Med. Phys. **26**, 1847-1870 (1999)

[42] A. F. McKinlay, _Thermoluminescence dosimetry_, Medical Physics Handbooks 5, Adam Hilger Ltd, Bristol, England (1981)

[43] J. R. Cameron, N. Suntharalingam, G. N. Kenney, _Thermoluminescent dosimetry_, The University of Wisconsin Press, Madison, 1968

[44] A. P. Pinkerton , J. G. Holt, J. S. Laughlin, "Energy dependence of lithium fluoride dosimeters and high electron energies", Phys. Med. Biol. **11**, 129 (1966)

[45] E. H. Crosby, P. R. Almond, R. J. Shalek, "Energy dependence of lithium fluoride dosimeters at high energies", Phys. Med. Biol. **11**, 131 (1966)

[46] J. G. Holt, G. R. Elderstein, T. E. Clark, "Energy dependence of the response of lithium fluoride TLD rods in high energy electron fields", Phys. Med. Biol. **20**(4), 559-570 (1975)

[47] N. Mobit, A. E. Nahum, P. Mayles, "The energy correction factor of LiF thermoluminescent dosemeters in megavoltage electron beams: Monte Carlo simulations and experiments", Phys. Med. Biol. **41**, 979-993 (1996)

[48] M. Olivares, F. Deblois, E. B. Podgorsak, J. P. Seuntjens, "Electron fluence correction factors for various materials in clinical electron beams", Med. Phys. **28**(8), 1727-1734 (2001)

[49] V. Robar, C. Zankowski, M. Olivares Pla, E. B. Podgorsak, "Thermoluminescent dosimetry in electron beams: energy dependence", Med. Phys. **23**(5), 667-673 (1996)

Chapter 3. Materials and Methods

The first part of this chapter is devoted to the Monte Carlo simulation techniques and particularly to their use in this work. Then, pencil beam algorithms applied to dose calculation will be presented, with a special emphasis on the algorithm underlying the CadPlan electron treatment planning system and its application in this work. Finally, the experimental techniques followed to measure dose profiles and dose distributions will be detailed.

3.1 Monte Carlo simulation techniques

Analytical solutions to electron and photon interactions are difficult to achieve due to their complexity. Therefore, probabilistic approaches such as Monte Carlo techniques appear advantageous for the accurate resolution of these problems. This section starts by a general description of the algorithm, followed by a presentation of the Monte Carlo codes used in this project. Finally, the methods followed in the simulations are detailed.

3.1.1 Principle of Monte Carlo techniques

Monte Carlo techniques may be applied in radiation transport to simulate extensively the random trajectories of individual particles by using a random number generator to sample from the known probability distributions that govern the physical interaction processes of photons, positrons and electrons in matter. A Monte Carlo radiation transport algorithm transports each original particle placed in the beam, as well as its offspring, according to the type of particle, its energy, its position in the geometry and its direction through a probabilistic selection of the type of interaction it can undergo. Along the path of the particle, selected physical quantities of interest are stored and after transport of a large number of particles, the average and the standard deviation of these quantities may be calculated. The main components of a Monte Carlo code consist of the cross-section data for all the interaction processes considered in the simulation, the

transport algorithm, the methods for geometry specification and determination of quantities of interest, and the data analysis tools.

3.1.1.a Particle transport

In radiation dosimetry, electrons and photons as well as a few positrons need to be transported. Particles are stored on a stack with their parameters such as the charge, energy, position and direction. A particle's history is defined from the beginning of its transport until both the original particle and its progeny are absorbed or exit the volume of interest.

> ### ➤ Photon transport algorithm

If the particle is a photon, it can undergo photoelectric effect, Compton or Rayleigh scatter, pair production and each one of these types of interactions are modeled in the transport algorithm The basic steps of transport are as follows. Given that the photon is in the volume of interest and has an energy larger than the photon energy cut-off for transport (PCUT), the distance to the next site of interaction, or step length, is sampled with the random number generator. The photon is then transported, the geometry being taken into account, and discarded if it leaves the volume of interest. On the contrary, if the photon is still in the volume of interest at the end of the step, the type of interaction it will undergo, including the energy and direction of any secondary particles emitted, is sampled from the interaction cross-sections and probability distributions. The secondary particles produced during the interaction are placed on the stack for further transport. At each photon step, it is possible to store the energy deposited in a given region.

> ### ➤ Electron transport algorithm

Two approaches to electron transport are available: ETRAN (Electron TRANsport) developed by Berger and Seltzer[1] in 1973 and EGS (Electron Gamma Shower) developed by Ford and Nelson[2] in 1978. Only the latter has been used in this work and will be described further.

While the transport of photons can be simulated on a step-by-step basis, the large number of electron interactions and the subsequent secondary knock-on electrons and excitation of atoms, necessitated the introduction of the condensed history technique[3]. In the condensed history technique, the path of an electron is broken into short, straight steps. For each step, the effects of the numerous electron interactions occurring (namely the large number of deflections due to elastic scattering treated by Moliere's or Goudsmit and Saunderson's multiple scattering theories and the large number of small energy losses treated under the continuous slowing down approximation (CSDA)) are grouped together. The overall deflection angle sampled from multiple scattering distributions is applied at the end of each step. Since electron paths are not straight in reality, a path length correction (PLC) is required to account for the curvature of the path, as well as a lateral displacement correction, making computationally expensive extremely small steps unnecessary. Berger[3] distinguished two classes of electron transport algorithms. Class I algorithms (such as that used in ETRAN) group the energy losses and angular deflections corresponding to individual events while the creation of secondary particles (knock-on electrons and bremsstrahlung photons) do not affect the energy and direction of the primary particle. On the other hand, class II algorithms, such as that used in EGS, correlate the energy and direction of the primary particle with the creation of secondary particles. Therefore, the class II algorithms are essentially more accurate than the class I ones. Both class I and class II models use energy cut-offs (ECUT) only, whereas class II models also use the energy thresholds AE and PE above which secondary particles are transported individually and the stopping powers restricted to these thresholds.

Practically, in a class II algorithm, the electron transport algorithm starts by reading the energy, position and direction of the electron on the top of the stack. If the electron energy is lower than the electron energy cut-off (ECUT) or if the electron is outside the geometry, it is discarded. Otherwise, the distance to the next discrete interaction site is sampled with the random number generator. An upper limit to the multiple scatter step size and a transport algorithm for a given position (usually varies with proximity to a region boundary) are specified by the user. The net deflection angle is sampled depending on the electron energy and applied to the trajectory. An energy corresponding to the step length times the linear collision stopping power restricted to the

energy threshold for creation of knock-on electrons (AE) is lost during the step. This transport is repeated step by step until the electron has reached the point of discrete interaction such as the emission of a bremsstrahlung photon or δ-ray. At this point, the interaction type is sampled as well as its energy and direction. The parameters of the secondary particle are stored on the particle's stack and the primary particle's energy and direction are modified accordingly.

3.1.1.b Statistics, efficiency and variance reduction techniques

The various sources of uncertainty on the results of the simulations can be classified as either statistical (type A) or systematic (type B). Programming errors, modeling inaccuracies due to approximations, round off and truncation errors and inaccuracies in the cross-section data belong to the type B uncertainty group and are usually not included when the uncertainty on the result is reported. For the evaluation of the statistical uncertainty on the results, an estimator of the true variance s^2 can be written in the event by event method[4] as,

$$s^2_{\langle x \rangle} = \frac{1}{N-1}\left[\frac{1}{N}\sum_{i=1}^{N}x_i^2 - \left(\sum_{i=1}^{N}\frac{x_i}{N}\right)^2\right], \tag{3.1}$$

where N is the number of independent events (*e.g.* histories), x_i is an estimate for each quantity of interest for each history, assumed to follow a normal distribution and $<x>$ is the average of the x_i values.

In the limit of a large number of histories for a normal distribution, the quantity Ns^2 can be considered as constant. Therefore, the computation time is determined by the number of histories simulated. This also leads to the following definition of efficiency ϵ of a Monte Carlo simulation as[5],

$$\varepsilon = 1/Ts^2, \tag{3.2}$$

where T the computing time needed to obtain the uncertainty s^2.

Variance reduction techniques improve the efficiency by selectively discarding particles that do not contribute to the scored quantities and increasing the number of particles that do. Amongst the variance reduction techniques available in the EGSnrc package, are the exponential transformation of path length, forced photon interactions,

cross-section enhancement, bremsstrahlung splitting, correlated sampling and range rejection of electrons. This latter technique discards electrons whose residual range is smaller than the distance to the closest boundary, their energy being deposited locally.

3.1.1.c Family of codes used

> **EGSnrc**

The Electron Gamma Shower EGSnrc[6-8] Monte Carlo code simulates the following physical processes:

i) Photoelectric effect with atomic relaxations after creation of a vacancy, including creation of Auger and Coster-Kronig electrons and emission of fluorescent photons from K, L, M shells

ii) Rayleigh scattering

iii) Compton scattering

iv) Pair/triplet production (the triplet production is not modeled explicitly but is accounted for in the total cross-section for pair production)

v) Positron annihilation in flight and at rest

vi) Bremsstrahlung production with EGS4 or NIST cross-sections

vii) Multiple-scattering with relativistic spin effect or screened Rutherford elastic scattering and single elastic scattering for short step sizes

viii) Møller and Bhabba treatment of inelastic scattering for electrons and positrons

The cross-section data required for transport in materials of Z between 1 and 100 can be created using **PEGS4**, for an energy range of a few keV to several thousand GeV. The cross-sections for photon interactions are based on the data of Storm and Israel[9], updated to XCOM[10] whereas the stopping powers are imported from the NIST database developed by Berger and Seltzer[11]. The mean excitation energy I for mixtures is taken as a weighted average of the log of the I values of elemental materials. The density correction is determined by Berger and Seltzer's ESTAR based on the formula of Sternheimer[12].

The EGSnrc package encompasses BEAMnrc, DOSXYZnrc, SPRRZnrc, FLURZnrc, CAVRZnrc user codes which are coded in mortran and can be run under the Unix operating system. The EGS program relies on the HATCH and SHOWER subroutines for listing of the cross-section data and probabilistic transport respectively. SHOWER itself relies on the subroutines HOWFAR, HOWNEAR[13] and AUSGAB, that will be further explained in the section 3.1.3. Two random number generators are available in the EGSnrc codes: RANMAR (previously used in EGS4) and RANLUX with optimization levels from 0 to 4 and a 10^{65} periodicity.

The **BEAMnrc**[14] user code allows for simulation of radiation beams from any radiotherapy source, in particular electron beams from linacs. The accelerator model is built by stacking individual component modules (CMs) perpendicularly to the central axis of the beam. The dimensions and materials of each CM are specified in an input file. The sources in BEAM can be a monoenergetic source, a spectrum or a group of particles collected in a former simulation. The BEAM code then produces phase space output of the beam at any specified plane in the simulation geometry, which contains the energy, charge, position, direction and a tag called LATCH which records the particle's history, for all particles in the plane. Various characteristics of the beam can be read from the phase space file using the utility script BEAMDP: particle and energy fluence versus position, energy spectrum and distribution, spatial and angular distribution, and mean energy distribution. The input file also contains transport parameters such as the electron and photon energy cut-offs (ECUT and PCUT) below which the particle is discarded, the threshold energy for creation of knock-on electrons or bremsstrahlung photons (AE and AP) which are usually taken equal to the corresponding energy cut-off. The transport parameters also include the type of algorithm used for electron step (ESA) and boundary crossing (BCA). In the EGS code, the available electron step algorithms are PRESTA-I and PRESTA-II, the boundary crossing algorithms are PRESTA-I or EXACT with a specified distance to the interface or "skin depth" within which electrons are transported in single scattering mode. In the vicinity of an interface, electron steps are shortened so that no part of the electron path crosses the interface, the curvature and lateral displacement being accounted for. As the electron further approaches the interface, the steps are reduced so that the path length correction associated with the step is almost

zero. When this is achieved, the lateral displacement correction is switched off. This is reversed when the electron has crossed the interface and moves away. Single scattering is used at interfaces because multiple scattering only holds in infinite media.

The phase space file obtained by BEAM can then be used as input in the user codes **DOSXYZ** / **DOSRZ** that calculate the dose deposited in a 3-dimensional voxel Cartesian or cylindrical geometry[15]. The dimensions of the voxels are completely variable and a specific material and density for each voxel can be defined by the user or derived from a CT density matrix. The dose distributions can be analyzed with the STATDOSE program for rebinning, error analysis and plotting of the dose along vertical or horizontal axes.

Restricted mass collision stopping power ratios can be calculated with the **SPRRZnrc** user code using a scoring-on-the-fly technique[16] in a cylindrical geometry. The approximation proposed by Nahum[17] is used to treat track-end terms. **FLURZnrc** can report fluence related quantities in a cylindrical geometry. **CAVRZnrc** allows for scoring quantities relevant in the study of ion-chamber like cylindrical geometries.

➤ XVMC

Voxel Monte Carlo (VMC)[18] is a fast Monte Carlo algorithm written for 3-dimensional dose calculations in rectangular phantoms with simplified electron transport, allowing for calculations 35 times faster than EGS4. It is applicable in the energy range 3-30 MeV and for low Z materials of densities ranging from 0 to 3 g/cm^3. VMC also relies on a few approximations including: reduction of the number of histories actually simulated by re-use of the same electron history in different regions of the phantom; or the restriction of the step size to a maximum limit for low energy electrons, which decreases the overall number of electron steps per history. The sources in VMC can be monoenergetic beams of particles, phase space data generated by BEAM simulations, spectra or beams models. VMC first transports the particles voxel by voxel in water; then the path length, energy losses, extent of electronic progeny and scattering angles are re-evaluated in the heterogeneous phantom. For example, the pathlength is scaled by the ratio of unrestricted stopping powers of the material in the voxel to that of water, so that the electron at the end of the step in water has the same energy as that it would have after

a step through the actual material of the heterogeneous phantom. This evaluation requires the knowledge of the scattering and stopping powers in each voxel. The CT number of the voxel is associated with the proper range of Hounsfield values corresponding to a given mass density. Stopping powers for each voxel are then deduced from a fitted plot of the mass stopping powers for any tissue normalized to that of water as a function of the material density normalized to that of water. Scattering powers are related to the ratio of mass densities, which are in turn related to the Hounsfield number of the CT images. The electron densities are extracted from the ICRU 46[19] data. A more recent version of the algorithm XVMC[20] also allows for photon transport and dose calculations.

3.1.2 Simulation methods

For all the simulations in this project, the number of histories used was sufficient to produce a 2% statistical uncertainty. The simulations were run on a cluster of 20 Pentium III 1.0 GHz PCs, each one having two processors.

3.1.2.a BEAM model of a Varian linac CL2300 C/D

In this study, a BEAM model was built for the linac CL2300C/D (Varian Oncology Systems, Palo Alto, CA) in the electron mode. The simulation geometry is shown in Figure 3.1.

The model involved the following CMs: PYRAMIDS, CONESTAK or BLOCK for the electron cutout depending on its shape and CHAMBER for the phantom. To be noted as well are the inclusion in the model of the tungsten shield between the mirror and the jaws as well as the reticle above the electron applicator, and finally the approximation of the monitor chamber as a single kapton slab. The pencil electron beam impinging on the primary collimator was simulated as a monoenergetic and monodirectional beam of radius of 0.5 mm. This source model seems to trigger reasonable results, even though a Gaussian beam of Full Width Half Maximum 1-2 mm is sometimes used[21]. The energy of the beam was first approximated by adding 20% to the mean surface energy E_0 as

calculated from IAEA TRS-381[22] based on the measured depth of 50% dose R_{50} for the 10×10 cm^2 field[†],

$$E_0(MeV) = 0.656 + 2.059R_{50} + 0.022R_{50}^2. \tag{3.3}$$

The energy was then fine-tuned by comparison of calculated and measured central-axis depth doses until these matched within 2% of the maximum dose at all depths and 1 mm of R_{50}. After this energy tuning, the geometry was simulated for each set of energy and electron applicators.

Primary collimator
Scattering foils
Monitor chamber
Mirror
Shield
Jaws

Reticle
1st Trimmer

2nd Trimmer

Phase space
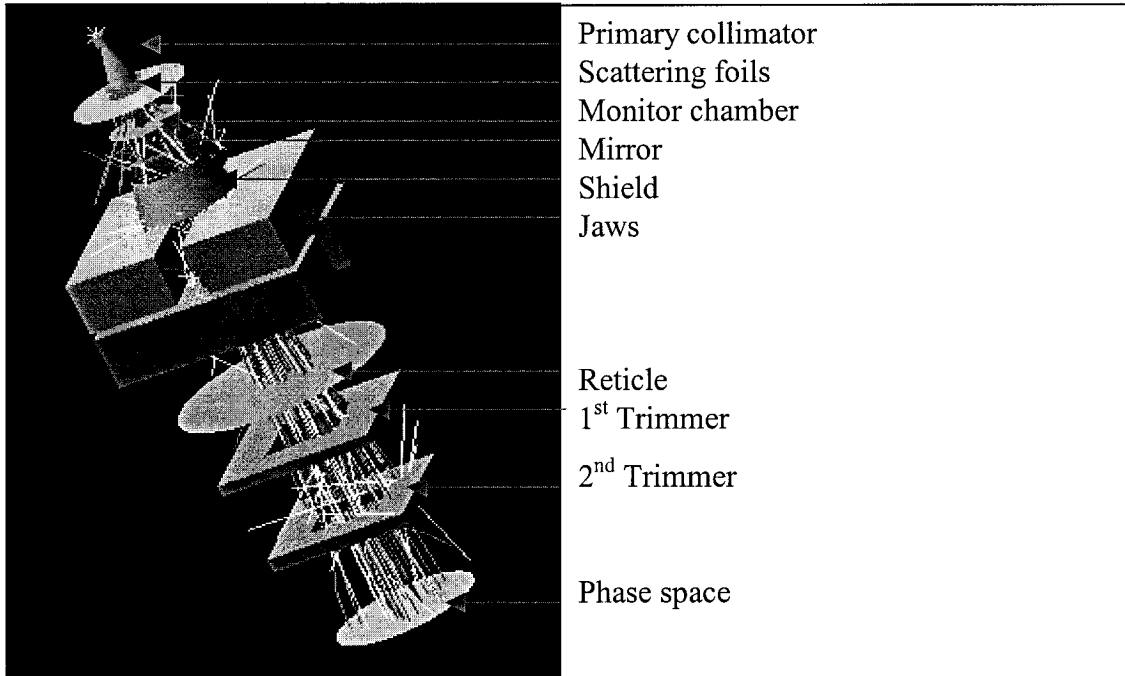
Figure 3.1: Geometry of the BEAM model built for a Varian linac CL230C/D until above the cutout as displayed by EGS_windows.

The transport parameters in BEAM were chosen conservatively in order to minimize the computing time. The total energy cut-offs were set to PCUT=AP=10 keV and ECUT=AE=700 keV which allowed an electron to travel by about 0.03 mm in tungsten, 3 mm in water and in 2.6 m in air. Older faster transport algorithms (ESA= PRESTA-I, BCA=PRESTA-I) were selected. The accuracy of simulations can be improved with the relativistic spin effect option turned on[23] which alters the depth of 50%

[†] All the field sizes mentioned correspond to the projected field dimension at the surface of the phantom, i.e. at 100 cm from the source, not to the actual physical size of the cutout.

dose in low *Z* materials. However, it was turned off in these simulations to allow later comparison with XVMC which does not have that feature. Electron range rejection was turned on in the upper part of the linac head (except for simulations for the low energy beams), with a threshold of 2 MeV allowing an electron to travel by 0.8 mm tungsten and 900 m in air. Bremstrahlung splitting and angular sampling, Rayleigh scattering, atomic relaxations, photoelectron angular sampling, Russian roulette and photon interaction forcing were turned off and the pair angular sampling was set to SIMPLE. The bremsstrahlung interactions were sampled from the Bethe-Heitler cross-sections. The cross-section data for all materials were available in a PEGS4 data file, built based on the ICRU 37[24] elemental data and density corrections along with the web version of the NISTIR-4999[11] report in order to incorporate the density effect in an identical fashion to that of ICRU Report 37.

Phase space files for 6, 9, 12, 15, 18, 22 MeV with applicators 6x6, 10x10, 15x15, 20x20, 25x25 cm^2 of the linac CL2300C/D were collected at a plane located exactly below the lowest scraper of the electron applicator, *i.e.* at 95 cm from the source. The number of particles in a phase space ranged from a few million to 30 million particles depending on the size, so as to keep a constant number of particles per unit area. The phase space was then used as input in the dose scoring EGS user codes DOSRZnrc/DOSXYZnrc for further simulation in the phantom.

3.1.2.b Determination of dose profiles with DOSXYZ

The user codes DOSRZnrc/DOSXYZnrc were used, respectively, for calculation of PDDs and profiles in homogeneous and heterogeneous phantoms. PDDs were calculated using DOSRZ with voxels of radius matching that of the detector (1.25 mm for the diode) and of thickness 2 mm to match the resolution of the measurements, whereas profiles were simulated using DOSXYZ with voxels of 2.5 mm in the direction of the profile, 1 cm in the horizontal direction perpendicular to the profile and 2 mm in depth at the depths of interest (z_{max} and R_{50}). The transport parameters chosen in the phantom were upgraded with respect to those used in the BEAM simulations as the dose needed to be obtained accurately using DOSRZ/DOSXYZ. The total energy cut-offs and thresholds were now set to PCUT=AP=10 keV and ECUT=AE=521 keV, which allows an electron

to travel by 2.5 μm in water. More accurate transport algorithms were chosen (ESA=EXACT with skin depth=3 cm and BCA=PRESTA-II). However, the spin effect was still turned off to allow comparison with XVMC.

3.1.2.c Determination of cutout factors with BEAM

The depth dose values obtained by BEAM simulations were used to calculate the cutout factors and the depths of maximum dose. After each depth dose curve was fitted and smoothed, the depth and value of the maximum dose were extracted. The number of incident particles corresponding to 100 MU for various field sizes and applicators with different jaw settings was assumed to be identical. This assumption allowed for determination of the cutout factor by a direct ratio of the maximum dose for the field of interest to the maximum dose for the reference field. The validity of this assumption was evaluated by estimating the amount of backscatter reaching the monitor chamber, thus reducing the number of incident particles corresponding to 100 MU. The monitor chamber in the linac CL2300 has thick windows but no backscatter plate between the chamber and the jaws and it is therefore reached by particles scattering backwards. However, the particles scattered from the cutout usually do not reach the chamber. Zhang[25] proved that the dose in the chamber per incident particle remained the same with varying cutout sizes as long as the applicator and corresponding jaw settings remained constant. But the particles backscattered from the jaws contribute to the charge in the monitor chamber and therefore the variation of the jaw opening with different electron applicators becomes critical for the determination of the output factor of a linac. The plot of the particle fluence below the monitor chamber in Figure 3.2 and the plot of the angular distribution of electron and photons in Figure 3.3 confirm the presence of backscattered particles.
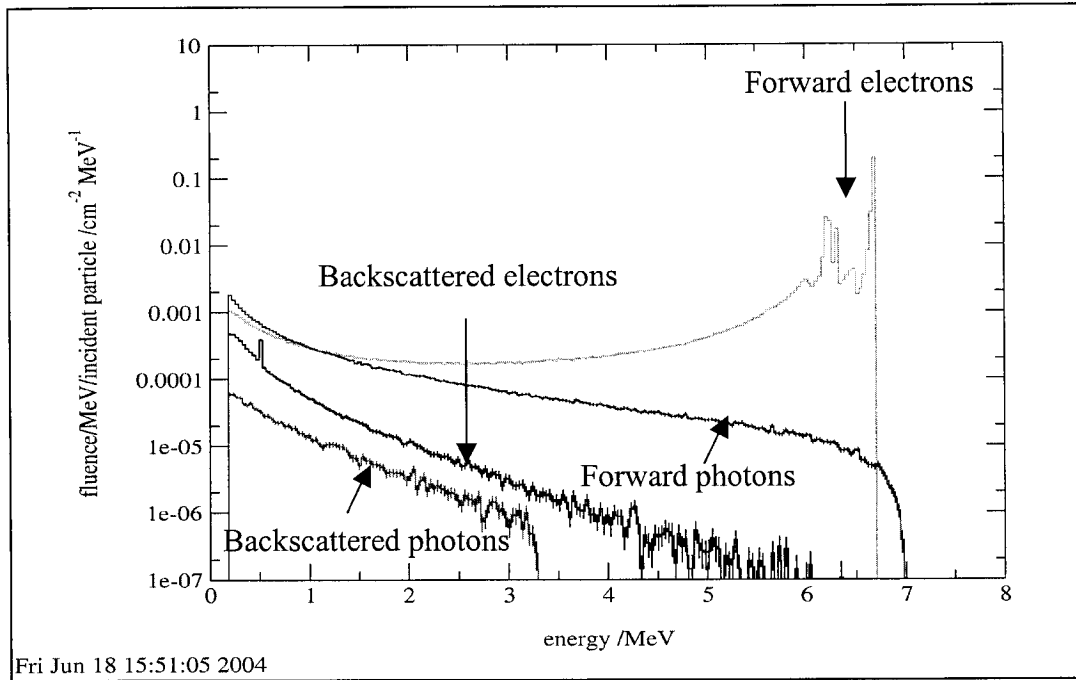
Figure 3.2: Graph of the particle fluence versus energy below the monitor chamber.
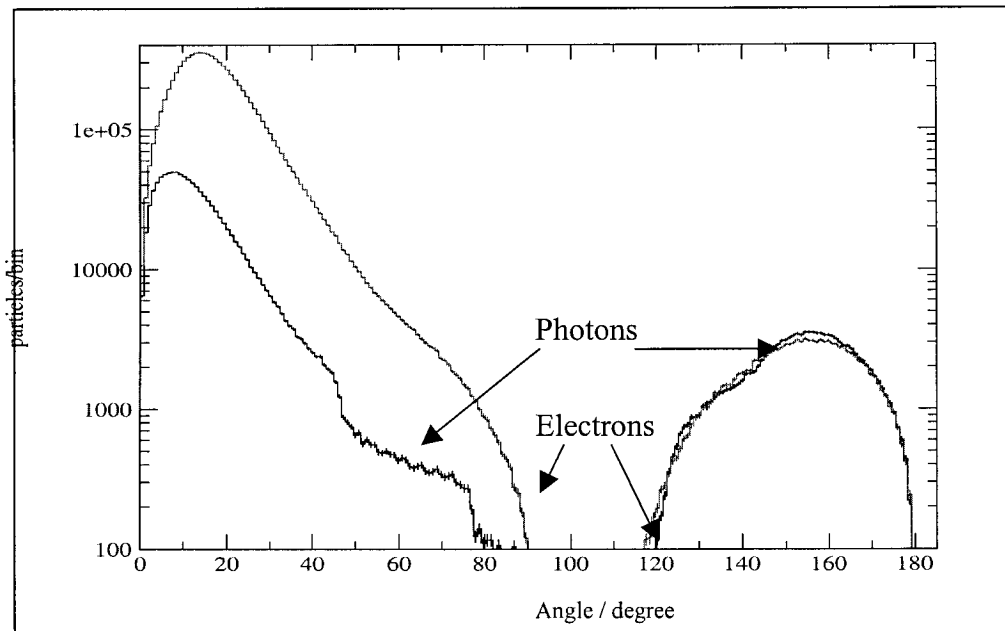
Figure 3.3: Graph of the angular distribution of particles below the monitor chamber.

To estimate crudely the importance of the backscatter, the dose was scored in our slab approximation of the monitor chamber after simulation with an identical number of

histories and the backscatter factor was established by normalizing the dose to the monitor chamber for a given field to the dose to the monitor chamber for the reference field (*i.e.* 10x10 cm^2 field obtained with the 10x10 cm^2 applicator). As expected, the backscatter was found to become closer to unity as the energy increased due to a lower importance of backscattering. For a 6 MeV beam, the backscatter factor for a 1x1 cm^2 field with applicator 6x6 cm^2 (with jaws set to 20x20 cm^2) was determined to be 0.987, compared with 0.993 for a 25x25 cm^2 field with applicator 25x25 cm^2 (with jaws set to 30x30 cm^2). At 12 MeV, a 4x4 cm^2 field with applicator 6x6 cm^2 (with jaws set to 11x11 cm^2) had a backscatter factor of 1.001 and a 25x25 cm^2 field with applicator 25x25 cm^2 and jaws opening 14x14 cm^2 has a backscatter factor of 0.994. These values for the backscatter factor agreed within 1.3% with the results reported in the literature for a more detailed model[26] and confirmed the validity of our assumption for the calculation of cutout factors.

3.1.2.d Dose calculations with XVMC

XVMC simulations were performed on CT images of the rectangular and anthropomorphic phantoms studied in this work. The radiation source used was a phase space collected 5 cm above the phantom, the gap between the phase space and the phantom being filled with air. The electron kinetic energy cut-off was set to 0.189 MeV. The simulations were run until a 2% statistical uncertainty on the results was achieved. The CT images were acquired with a slice thickness of 5 mm for rectangular slabs phantoms and of 3 mm for the head of the anthropomorphic phantom. To be noted as well is the acquisition of the CT image of the anthropomorphic phantom in presence of the thermoluminescent dosimeters in their respective measurement positions, in holders made out of medium equivalent material. The built-in treatment of CT data by XVMC was used without further conversion of the Hounsfield units into specific materials. This conversion ignores the atomic number of the materials involved.

For the rectangular phantoms, XVMC simulations were also run on corresponding mathematical phantoms in order to assess the impact of both the CT artifacts and the approximate conversion of the CT data into material on the dose calculations. The dimensions of the voxels of the mathematical phantoms were set to 5x5x2 mm^3,

considering that the resolution in depth was the only critical parameter in these phantoms with 1-dimensional heterogeneity. The mass densities of the materials entered in the mathematical phantom simulations with XVMC needed to be adjusted to compensate for the effect introduced by XVMC's disregard for the atomic number of the materials involved and for the fitted stopping power data. Such approximations are definitely critical for bone material whose atomic number is about 60% higher than that of water, they also play a role for solid water. (Throughout the thesis, the term *solid water* will be used to refer to the material Solid Water™ (Gamex-RMI, Middleton, WI)). Therefore, the mass densities of solid water and bone were determined iteratively by matching the resultant percentage depth dose in a homogeneous phantom to that determined with EGSnrc/DOSXYZnrc, as previously suggested by Doucet *et al*[27], the spin option being turned off. Mass densities used in XVMC for lung, solid water and bone were found to be 0.270 g/cm^3, 1.015 g/cm^3 and 1.820 g/cm^3 respectively corresponding to densities of 0.270, g/cm^3, 1.045 g/cm^3 and 1.840 g/cm^3 in DOSXYZnrc. The densities values used in DOSXYZ represent the average of the physical mass densities of the materials used in the phantom.

The CT images were manipulated prior to calculation with XVMC. The CT data from the CadPlan CART format were converted into an XVMC density matrix with a home-built C routine. In the CT conversion process, two or more adjacent voxels were averaged into one. The goal of this *compression* (as it will be referred to throughout the rest of this report) of the CT data is to save computing time. The impact of the compression factor was studied on the homogeneous solid water phantom by comparing the PDD obtained with different compression values to the PDD obtained for a mathematical phantom. As shown in Figure 3.4, the larger the compression value, the smoother the PDD and the better the agreement with the PDD of the mathematical phantom. In particular, the sudden drop in the dose after initial build-up due to inter-layer air gap is attenuated as the compression factor increases. On the other hand, the compression introduces an error in the surface dose due to the averaging of the density of the voxel at the surface of the solid water phantom with that of the adjacent air voxel above. This error at the surface worsened with an increasing compression factor. Therefore, as a compromise, a compression factor of 2 was chosen for all CT data in the

rest of the study. This resulted in a surface dose that was inexact but that could be obtained by extrapolation from the build-up region trend. Moreover, all PDDs simulated in CT images are shifted downstream by 1 mm with respect to the PDD simulated in a mathematical phantom. This discrepancy could be due to an inaccurate attribution of interaction data to the Hounsfield number of the CT. Or, some of this shift may owe to the narrow air gaps between slabs that appear on the CT images.
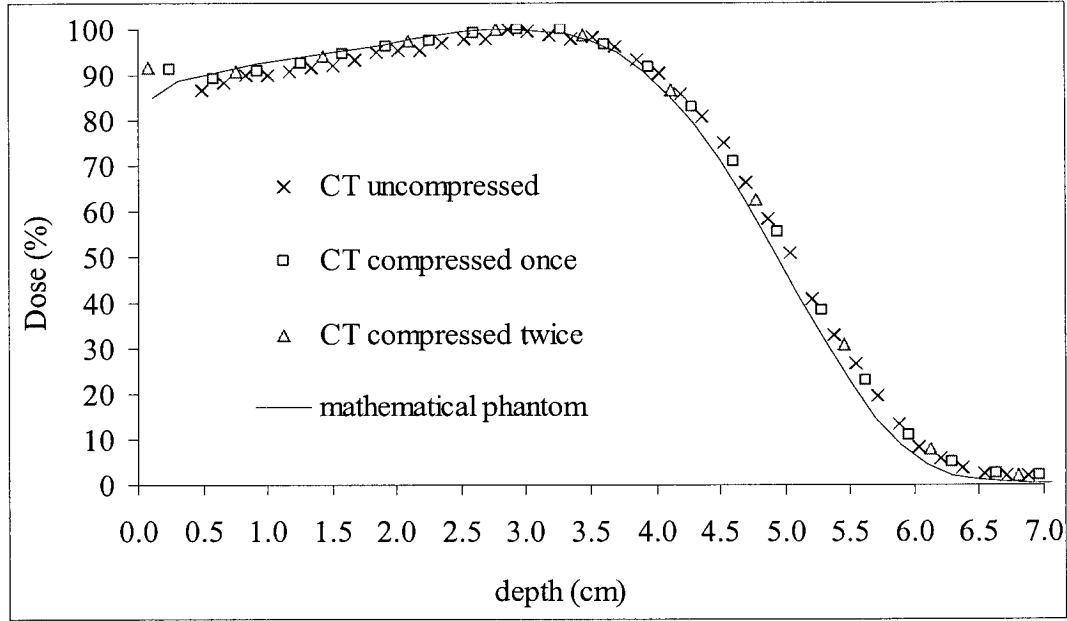
Figure 3.4: Effect of the compression value on the PDD in a homogeneous solid water phantom for 12 MeV, 10x10 cm² field. XVMC simulations performed in CT images, uncompressed (+), compressed once (□) and twice (△), are compared to XVMC simulations run in a mathematical phantom (continuous line).

A Matlab routine was then developed to read the XVMC and CadPlan dose matrices and plot the corresponding dose distributions overlaid with measurements. To make the dose distributions comparable to CadPlan's distributions and to measurements performed with 100 MU, it was necessary to determine how many particles correspond to 100 MU. Therefore, the dose to the medium calculated by XVMC in the heterogeneous phantoms was divided by the dose to solid water at z_{max} in solid water calculated by XVMC and multiplied by the calibrated dose to solid water for 10x10 cm² at z_{max}. The linac is calibrated to output 101.1 ± 2.0 cGy / 100 MU in water at z_{max} in a 10x10 cm² field impinging on a solid water phantom as measured with a PTW Farmer chamber. A

dose of 101.1 cGy in water is equivalent to a dose of 100 cGy in tissue and calibrating the linac to 100 cGy / 100 MU in tissue yields a simple relation between the MUs measured by the monitor chamber and the dose delivered. The output in solid water was then deduced from the output in water by multiplying by the ratio of Monte Carlo doses at z_{max} in solid water and in water. These doses were scored with DOSXYZ in a voxel whose dimensions imitated those of the chamber, as illustrated in Figure 3.5. This simulation was run to a 0.7% uncertainty and the calculated linac output in solid water at z_{max} of 96.2 ± 2.1 cGy / 100 MU.
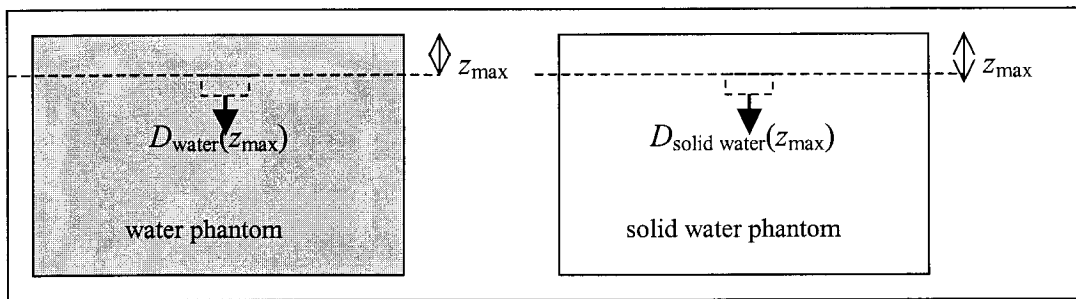
Figure 3.5: Geometry of phantoms in DOSXYZ simulations in homogeneous phantoms.

3.1.3 CUTOUT code for transport of particles through arbitrary cutouts

The BEAM code offers the BLOCK component module displayed in Figure 3.6 to simulate electron beam cutouts. However, this module does not allow for simulation of concave cutouts and the separation of the cutout into a few convex shapes is too labor intensive to be conceivable in a clinical setting. Therefore, to enable the use of Monte Carlo for simulation of clinical irregular fields, it appeared useful to write a code able to handle arbitrary cutout geometries and calculate clinically relevant parameters such as the cutout factor, the depth of maximum dose and depth dose curve.

The CUTOUT code, written in mortran, transports the particles contained in an input phase space corresponding to a given energy and applicator size, through a simulation geometry consisting of a first layer, the cutout itself, a second layer and a homogeneous phantom. The source used is a phase space file collected at the bottom of a BEAM simulation, 2 cm above the top cutout plate. Thus, 30 phase spaces corresponding to each combination of energy and applicator were collected. The geometry of the cutout simulations is illustrated in Figure 3.7.
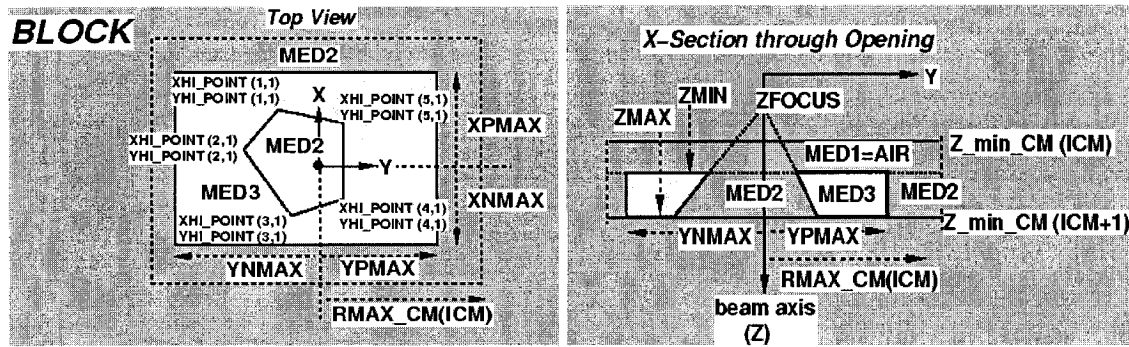
Figure 3.6: Geometry of the BLOCK component module in the BEAM code[15].
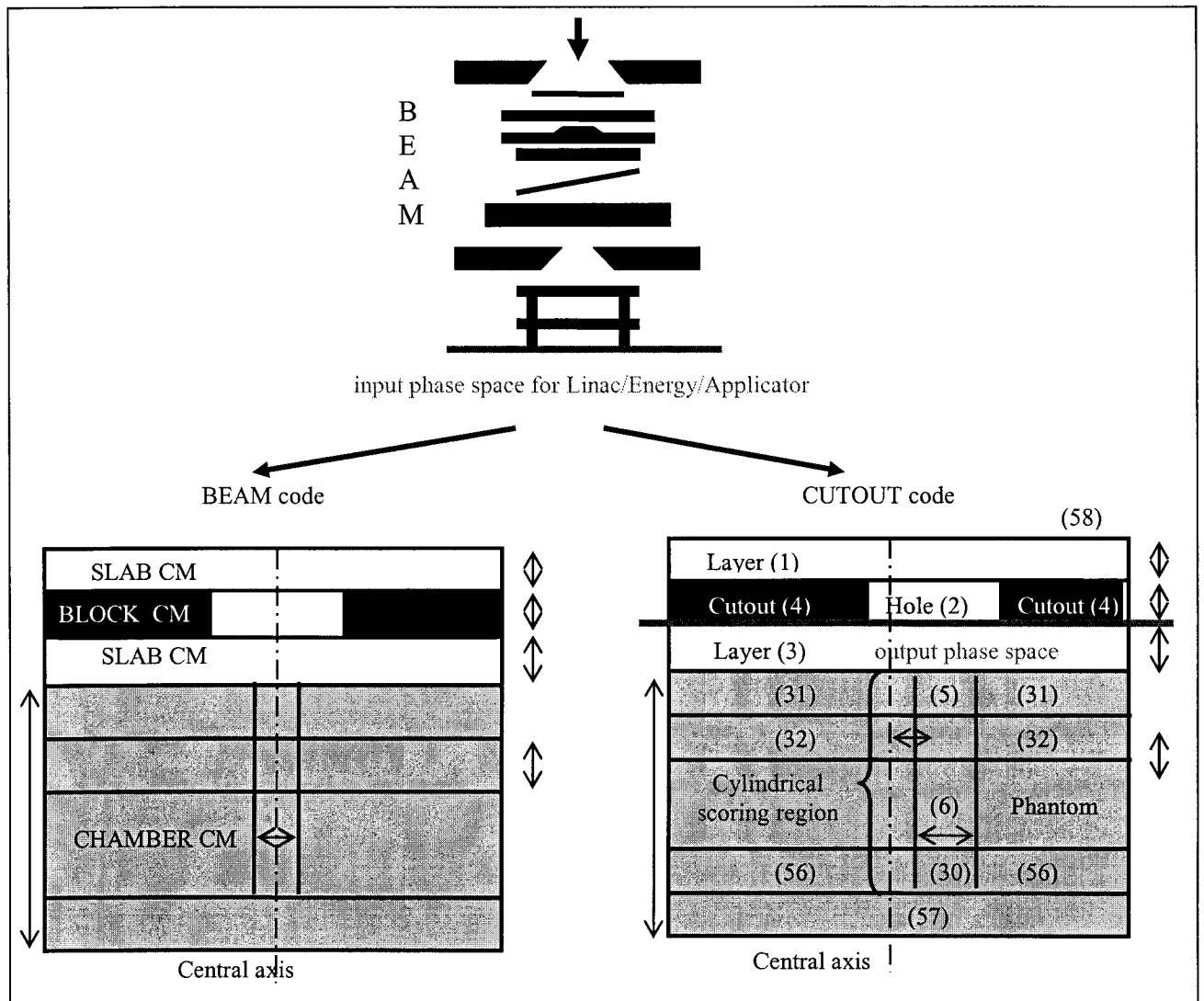
Figure 3.7: Simulation geometry of the CUTOUT code. Particles in a plane below the accelerator head simulated down to the cutout are collected in a phase space used as source input both in the CUTOUT code and BEAM. The values within brackets in the CUTOUT geometry correspond to the region number in the code.

Depending on the user's requirement, an output phase space file can be collected just below the cutout for further simulation in DOSXYZnrc and XVMC, or the dose deposited in the phantom by each particle can be scored in depth along the central axis or any other specified vertical axis. The maximum dose obtained for the cutout is then normalized to the maximum dose for the reference field and the cutout factor and z_{max} are output. The only limit on the geometry of the cutout is that its side walls that have to be vertical.

To make the program more user-friendly, a graphical user interface (GUI) was written in REALbasic 5.5. The flowchart in Figure 3.8 summarizes the organization of the system and the interactions between the code, the GUI and the input/output files.
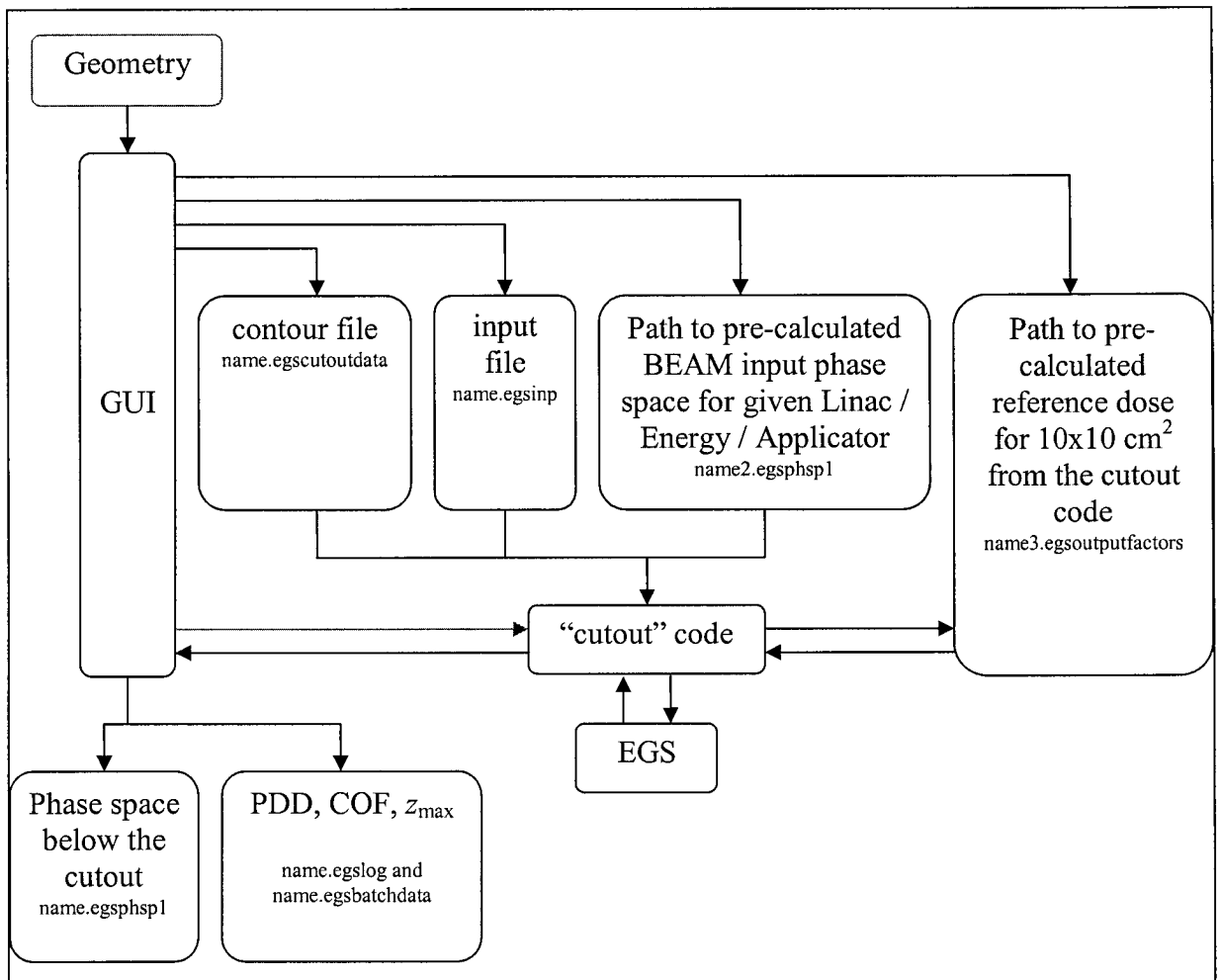
Figure 3.8: Flowchart describing the organization of the automated system with the interaction between the GUI, the mortran code itself and the input and output files.

All geometry parameters (dimensions and materials) are input by the user in the GUI, including a scaled contour of the cutout that can be digitized with the mouse on the computer screen. The Monte Carlo transport parameters can also be modified from the default parameters (set to conservative values) on a separate password-protected page reserved to "expert" users. With those data, the GUI creates an input file for the CUTOUT program marked by the extension ".egsinp", the structure of which is detailed in Table 3.1.

Line #	example	description	Variable name
1	CERROBEND700□#	Material of the cutout as named in the pegs file	MEDIA(J,1), J=1:24
2	AIR521ICRU□#	Material of the surroundings and cutout hole as named in the pegs file	MEDIA(J,2), J=1:24
3	H2O521ICRU □#	Material of the phantom as named in the pegs file	MEDIA(J,3), J=1:24
		For the 3 first lines, spaces need to be placed after the name so that overall it amounts to 24 characters, then a # is placed.	
4	0.189□	ECUT - 0.511 (MeV)	ecut
5	0.1□	PCUT (MeV)	pcut
6	0.3□	Distance from the input phsp to the upper plate of the cutout (cm) (=2-thickness_cutout in my case)	cutout_start
7	1.7□	Thickness of the cutout plate (cm) (It has to be less than 2 cm in my case)	zbound
8	5□	Distance between the cutout and the phantom (cm)	phant_start
9	0.2□	Thickness of the scoring region (cm) (It has to be larger than 0.2 cm)	thick_sc_reg
10	0.125□	Radius of the scoring region (cm) (It has to be larger than 0.04 cm) (It also has to be larger than half the minimum cutout extent.)	rad_sc_reg
11	30□	Total phantom thickness (cm) (It has to be at least 25 × thick_sc_reg + 5 (cm))	phantom_thickness
12	/login/egsnrc/cutout/phsp/CL23_6_10.egsphsp1□		
		Path to input phase space including the file name with extension All input phase spaces are placed in the "phsp" directory. Name convention for GUI: Linacname_Energy_ApplicatorSize.egsphsp1	filnam
13	200000000□	Number of histories to simulate	ncase
14	10000□	Number of particles in the buffer where read particles are stored	n_buffer
15	10000□	Number of particles in the buffer where transported particles are written	n_buffer_out
16	2□	calculate phsp after cutout (1), dose to voxel (2), or both (3)	icalc
18	/ login/egsnrc/cutout/phspout/CL23_6_10_777777_10x10.egsphsp1□		
		Path to input phase space including the file name with extension All output phase spaces are placed in the "phspout" directory.	output_file
19	0□	Ignore rebackscatter from the phantom (1) or not (0)	Iignore_bs
20	6□	Nominal energy of the electron beam (MeV)	IEnominal
21	###		
22	Physicist name #	Name of the physicist	
23	Patient last name #	Last name of the patient	
23	Patient 1st name #	1ˢᵗ name of the patient	
24	Patient ID #	7-digit patient Identification number (used to classify the case)	
22	Field name #	Name of the field (used to classify the case)	

Table 3.1: Structure of the input file for the CUTOUT user code. The first column shows the line number, the second is an example of what should be written, the third column the description of the data on each line and the fourth column the corresponding variable name. The symbol □ stands for a space. The last lines are printed in grey to show that those lines are read by the GUI but are not relevant to the CUTOUT code itself.

The GUI also writes a geometry file with the extension ".egscutoutdata". This file contains the number of points defining the contour and the x and y coordinates for each one of these points (which must be at least 0.028 cm away from each other); the point

where the user wants the dose to be scored in the phantom, (x, y = 0, 0 for the central axis) is also defined in this file in the first line. The GUI determines the path to the appropriate input phase space from a name convention based on the linac, energy and applicator selected (*e.g.* CL21a_12_15.egsphsp1 for the 12 MeV beam of the linac CL21ExA with the 25x25 cm^2 applicator). The GUI also sets the path to the file containing the dose and uncertainty data for the 10x10 cm^2 reference field as previously calculated by the CUTOUT code, these values are used to normalize the maximum dose for a certain field to determine the cutout factor. Such a file with extension ".egsoutputdata" is created for each combination of linac and phantom material.

Afterwards, upon user initiative, the GUI starts the execution of the CUTOUT program. The cutout code reads the input in the ".egsinp" and ".egscutoutdata" files. The code then transports the particles of the input phase space with calls to the HATCH and SHOWER of the EGSnrc package and home-developed AUSGAB, HOWNEAR, HOWFAR and INSIDE_CUTOUT subroutines, as detailed in the next paragraph. After all particles have been transported in 100 batches, the code creates an output file with the extension ".egslog" containing a summary of the input parameters, the dose results and messages that occurred during the execution. A file with the extension ".egsbatchdata" is written after every 1% execution and it allows for retrieving partial dose results even if the execution is aborted for some reason. The GUI uses this file to determine the status of the calculation. This system permits live visualization of the PDD as it is calculated; the run can then be aborted when the user judges the PDD is smooth enough and has a reasonable statistical uncertainty.

The HATCH routine builds the adequate cross-section tables corresponding to the materials in the PEGS file and specified energy thresholds. The SHOWER routine is initiated once per history to call the proper subroutines for photons, electrons and positrons; it samples a step length and interaction type for the particle transported from the probability distributions and interaction cross-sections using a random number generator.

The AUSGAB subroutine scores the quantities of interest. In our case, it writes the output phase space by calling the routines contained in the home-developed

"phsp_rw.c" code that groups the commands to open, write in and close a phase space file. AUSGAB also stores the amount of energy deposited during that step.

In HOWFAR, the pathlength *tval* of the particle from its current location to the next region boundary on its trajectory is calculated and compared to the step length. If the step length is larger than the pathlength, the particle can cross the boundary and the region number is updated to that of the new region. The possible offset of the center of the scoring region is accounted for in the section of HOWFAR that treats the particles in the layer just below the cutout (region 3). The coordinates of particles traveling forward are re-centered with respect to the offset point. Moreover, the particles moving backwards are discarded, when the user has chosen to ignore the phantom backscatter. Finally, in the section dealing with the particles located in the cutout plate layer, the program scans the segments defining the cutout contour and for each one, determines whether the angular sector it defines with respect to the particle intersects the particle's direction vector *v*. If so, this segment is stored as a segment of interest and the pathlength to the vertical and horizontal adjacent region boundaries associated to this segment of interest, respectively *tval* and *tval_cutout*, need to be considered. The minimum pathlength is stored as the final *tval*. Figure 3.9 illustrates this process.
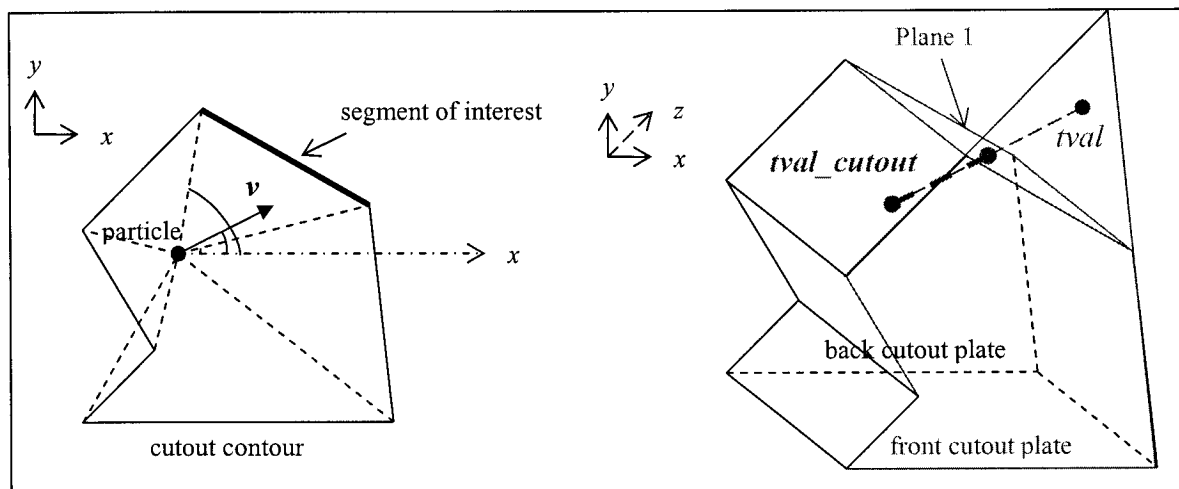
Figure 3.9: Illustration of the determination of the closest boundary by HOWFAR for particles in the cutout plate region (region 2 or 4). On the left, the determination of the segment of interest is described on a 2-dimensional drawing whereas the right drawing shows the calculation of "tval" in a 3-dimensional display. The distance between the particle and plane 1 along the particle's direction is called tval; and the distance between the particle and the plane of the front cutout plate along the particle's direction is called tval_cutout.

The subroutine HOWNEAR determines the distances from a particle's current location to the side, upper and lower region boundaries, in lines parallel to and perpendicular to the central axis and stores the minimum of these values as *tperp*, further used in HOWFAR, as illustrated in Figure 3.10.
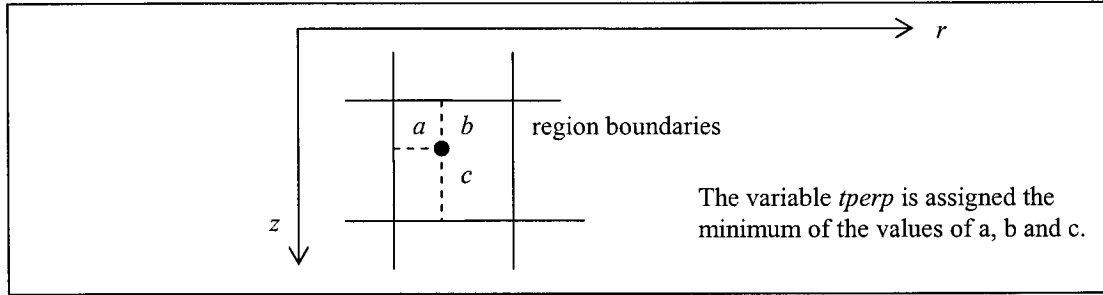
Figure 3.10: Illustration of the process of determination of the distances to the vertical and horizontal boundaries by HOWNEAR. The point figures the particle and the lines the region boundaries.

When the particle is in the cutout region, a subroutine INSIDE_CUTOUT (called by HOWFAR) determines whether the particle in the layer containing the cutout plate is in the cutout material or in the hole, in a process described in Figure 3.11.

The reference point O is set as the point having for coordinates the minimum x and minimum y of the cutout contour points, shifted by a given constant. The thick lines show the segments of interest on the contour for this configuration (tested by same method as in figure 3.10). The line joining O to M intersects these segments of interest in B, C, D and E. The distances from O to M, B, C, D and E, respectively r_M, r_B, r_C, r_D, r_E and r_E, are then compared.

$r_B < r_C < r_D < r_M < r_E$ so M $\in$ [DE]

Depending on the index of the intersection points between which the particle is located, the routine determines whether the particle is inside the cutout or not.

Figure 3.11: Illustration of the process followed by the routine INSIDE_CUTOUT to determine whether the particle (point) is inside the cutout or not.

3.2 Dose calculations with a pencil beam algorithm-based treatment planning system

The algorithms of choice for electron beam treatment planning are pencil beam algorithms that calculate the dose at a point by summing the dose contributions from all the Gaussian pencil beams constituting the field. The first part of this section describes the general principle underlying pencil-beam algorithms. Then, the pencil-beam of the treatment planning system CadPlan version 6.7.2 (Varian) is briefly summarized. Finally, the parameters set in CadPlan for this work are described as well as the fashion in which the results are exploited.

3.2.1 Principle of pencil beam algorithms

As summarized by Khan[28], pencil beam algorithms used in radiation beam therapy are based on the Fermi-Eyges theory to account for multiple Coulomb scattering. The spatial distribution of the electron fluence/dose of an elementary pencil beam penetrating a medium is nearly Gaussian at any depth under the small-angle approximation for the multiple scattering of electrons. The deviations from a pure Gaussian that could be caused by large angles are rare enough to be neglected overall, although this assumption leads to an underestimation of the dose at shallow depths and overestimation of the dose at larger depths. Thus, the dose d_p to a point *(x,y,z)* deposited by a pencil beam whose central axis passes through a point *(x',y',z')* is a function of the central-axis dose at depth *z* deposited by an infinitely broad beam with the same incident fluence at the surface as the pencil beam, $D_\infty(0,0,z)$, as well as a function of the mean square displacement of electrons by multiple Coulomb scattering, σ^2,

$$d_p(x,y,z) = \frac{D_\infty(0,0,z)}{2\pi\sigma^2(x',y',z)}.e^{-\frac{(x-x')^2+(y-y')^2}{2\sigma^2(x',y',z)}}. \tag{3.4}$$

The total dose at any point *(x,y,z)* in any field is the sum of the contributions of all pencil beams weighted by their relative strength at a given point *s(x', y')*,

$$D(x,y,z) = \iint_{field} s(x',y')d_p(x-x',y-y',z)dx'dy'. \tag{3.5}$$

The relative strength of a pencil beam at a given point is derived from pre-calculated Monte Carlo kernels in homogeneous media. The above expression cannot be calculated

analytically and requires the use of error functions. Thus, for an electron beam of rectangular cross-section (2a×2b), the spatial dose distribution assuming a uniform electron beam (s=1 at any point) is given by,

$$D(x,y,z) = \frac{D_\infty(0,0,z)}{4}\left(erf\ \frac{a+x}{\sigma_r(z)} + erf\ \frac{a-x}{\sigma_r(z)} \right)\left(erf\ \frac{b+y}{\sigma_r(z)} + erf\ \frac{b-y}{\sigma_r(z)} \right), \quad (3.6)$$

where

$$erf\ (x) = \frac{2}{\sqrt{\pi}}\int_0^x e^{-t^2}\,dt. \quad (3.7)$$

The values of the error function erf are tabulated in mathematical databases and $D_\infty(0,0,z)$ is usually determined from measured central-axis broad beam dose values.

The lateral spread σ increases with depth until it reaches a maximum beyond which the teardrop shaped isodose distribution shrinks drastically due to the large lateral excursions of electrons compared to their range. σ depends on the thickness and linear angular scattering power of the slab. According to Eyges' extension of Fermi's small-angle multiple scattering theory to any slab geometry, the lateral spread is correlated to the mass angular scattering power by

$$\sigma_x^2(z) = \frac{1}{2}\int_0^z \frac{\theta^2}{\rho l}(z').\rho(z').(z-z')dz', \quad (3.8)$$

where $\sigma_x^2(z)$ is the square of the projection on the xz plane of the lateral spread at depth z, $\theta^2/\rho l$ is the mass angular scattering power evaluated for an energy corresponding to the mean energy at depth z' according to Harder's formula and ρ is the density of the slab material. Equation 3.8 has been modified to account for secondary particles (knock-on electrons and bremsstrahlung photons), for energy straggling, for loss of electrons whose range is smaller than the lateral excursion and for large angle scatter. Amongst the correction factors, there is an empirically derived multiplication factor (1 to 1.3) that improves the accuracy of σ_x in the penumbra region. A proper conversion of planar fluence into dose is also included. The electron collision linear stopping power and linear angular scattering power of the slab material relative to that of water have been correlated[29] to the CT numbers to allow calculation of the effective depth and the lateral spread for inhomogeneous phantoms. But, the linear stopping power ratios are evaluated according to ICRU 21[30] at 10 MeV and assumed independent of energy. The applicability of this approximation is questionable[31] for human tissues.

The pencil beam algorithm accounts for the photon contribution to the dose. It deduces this contribution from the measured depth-dose curve for blocked fields. The dose in the phantom beyond the practical range is assumed to be deposited by photons only and the photon contribution at shallower depths is assumed to increase only with inverse-square correction.

Contour irregularity and air gaps are inherently accounted for, since pencil beams are calculated along ray lines originating from the virtual source and intersecting the contour at a given distance from the source, as illustrated in Figure 3.12.
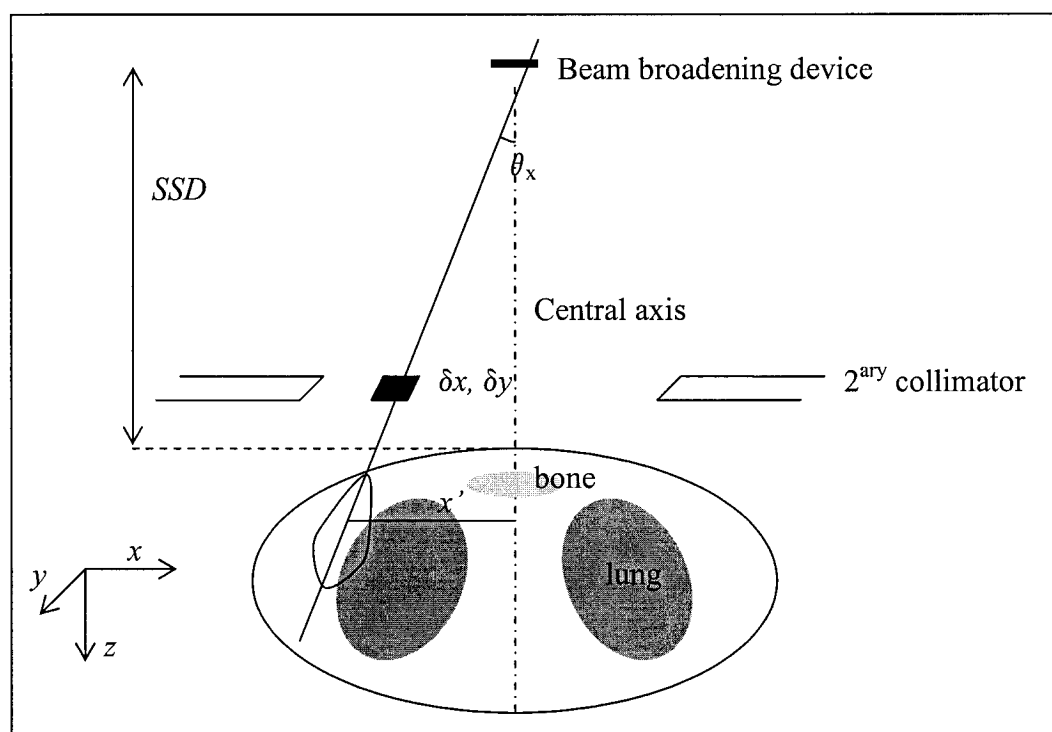
Figure 3.12: Schematic representation[28] *of Hogstrom's pencil beam algorithm for determination of dose distribution in a patient's cross-section in the xz plane of a clinical electron beam incident on a patient.*

For each pencil beam traversing the medium, the electron energy changes with depth only and the heterogeneities intersecting the central ray are extended temporarily into a semi-infinite slab. Due to this semi-infinite slab approximation, the pencil beam algorithm has been shown to fail[28] when the pencil beam spread exceeds the cross-section of the heterogeneity or when parts of the pencil beam traverse distinct heterogeneities at interfaces. Errors appear mostly in the shadow of thick heterogeneities with edges

parallel to the beam, due to a lack of scattering from the denser medium and due to a miscalculation of the particle range.

3.2.2 Pencil beam algorithm in CadPlan 6.7.2 (Varian)

The dose calculation algorithm implemented in CadPlan is based on a generalized pencil beam algorithm first developed by Lax[32]. Hyödynmaa[33,34] modified it, taking transversal slices and arbitrary field shapes into account but with a two-dimensional heterogeneity correction only. Hyödynmaa[35] further extended it to a three-dimensional form, which could handle non-coplanar fields, orthogonal slices and which performed three-dimensional heterogeneity corrections. The equations below have been quoted from the CadPlan guide[36]; some of them are printed in the revised form proposed by Hodefi[37].

The generalized pencil beam algorithm for high energy electron beams describes the radial dose distribution $D(r,z)$ of a pencil beam at depth z by a sum of m weighted Gaussians,

$$D(r,z) = \sum_{k=1}^{m} B_k(z).e^{-\frac{r^2}{b_k(z)r^2(z)}},$$
(3.9)

where B_k and b_k are the amplitude and the width factors of the Gaussian pencil beams, r the distance from the axis of the pencil beam and $\overline{r^2}(z)$ is the mean square radius of the beam at depth z. The mean square radius of the beam is calculated[38] iteratively based on the mean square scattering angle $\overline{\theta^2}$ and the covariance term $\overline{r\theta}$ as

$$\overline{r^2}(z) = \overline{r^2}(0) + \overline{r\theta}(0) + \overline{\theta^2}(0)z^2 + \int T(\overline{E_0})z^2.dz,$$
(3.10)

where T is the scattering power of air for the mean electron energy at the phantom surface $\overline{E_0}$. The angular variance $\sigma_\theta(z)$ is calculated as

$$\sigma_\theta(z) = \sqrt{z^2 \frac{\overline{\theta_0}^2}{2} + z^3 \frac{T}{6}}.$$
(3.11)

The relative fluence in air ϕ^{air} at the distance z_p where the pencil beam enters the patient is the average of two error functions of $\sigma_\theta(z)$, r_1 and r_2. As illustrated in Figure 3.13, r_1 and r_2 are the closest and next closest horizontal distances from the field edge to the fanline of interest at the level of the pencil beam entry into the patient,

$$\varphi^{air}(x, y, z_p) = \frac{1}{2}\left[erf\left(\frac{r_1(x, y, z_p)}{\sigma_\theta(z_p)\sqrt{2}} \right) + erf\left(\frac{r_2(x, y, z_p)}{\sigma_\theta(z_p)\sqrt{2}} \right) \right]. \qquad (3.12)$$
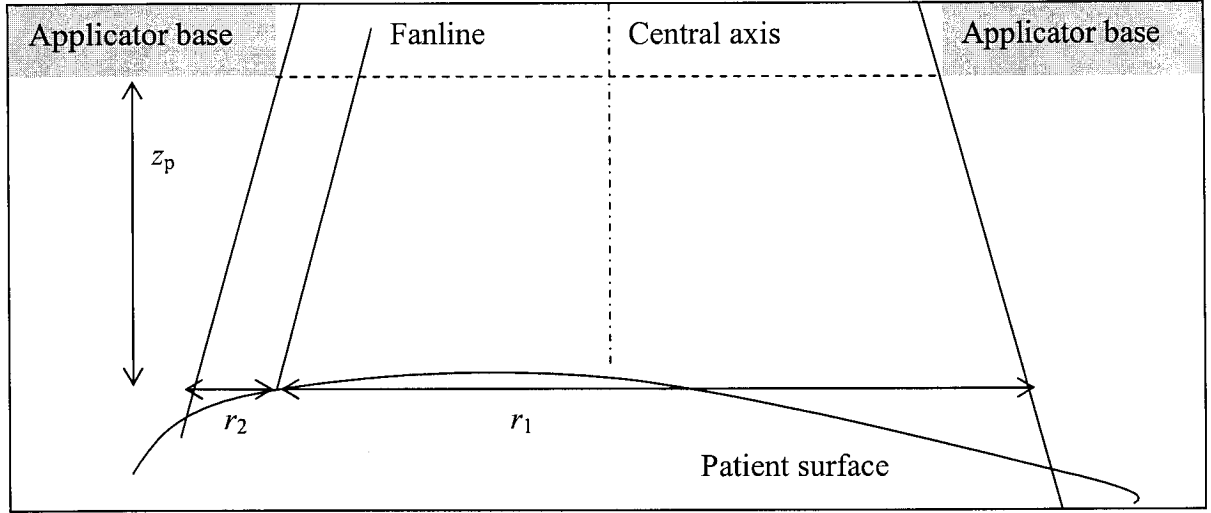
Figure 3.13: Illustration of the parameters used in the calculation of the fluence in air.

Then, the dose to a point (x,y,z) in a beam of incident field area A is obtained by convolving the Gaussian pencil beam by the particle fluence in air ϕ^{air}, the convolution being further weighted by the central-axis depth dose $P(z)$ as,

$$D(x, y, z) = \frac{P(z)\sum_{k=1}^{m} B_k(z) \int\int_A \varphi^{air}(x', y', z).e^{-\frac{(x-x')^2 + (y-y')^2}{b_k(z)r^2(z)\rho(z)}} dx'.dy'}{\pi r^2(z)\rho(z)\sum_{k=1}^{m} B_k(z)b_k(z)}. \qquad (3.13)$$

In this equation, $\rho(z)$ is the empirical reduction factor[39] accounting for range straggling, and is written as

$$\rho(z) = e^{-s^{12(1.5-s)}} \text{ where } s = 0.95 z/R_p. \qquad (3.14)$$

The depth dose $P(z)$ is described by the following equation

$$P(z) = P_0(z_{eff})\left[\frac{SSD_{vir} + z_{eff}}{SSD_{vir} + z} \right]^2, \qquad (3.15)$$

where $P_0(z)$ is the central-axis depth dose curve of a large field, SSD_{vir} is the virtual source to reference plane distance and z_{eff} is the effective depth. The heterogeneity

correction consists of rescaling the pencil beam in depth for heterogeneity along the fanline by the ratio of the total stopping powers, implemented by Lax and Brahme[40] as,

$$z_{\text{eff}} = \sum_{i=1}^{n} (z_i - z_{i-1}) \frac{S_{\text{tot},i}}{S_{\text{tot},w}}, \tag{3.16}$$

where z_{eff} is the effective depth, z_i is the depth of the ith layer, $S_{\text{tot},w}$ is the total stopping power of electron in water. The fluence in air is assumed to be uniform over the entire field area, except at the edges of the field where it is derived from Huizenga and Storchi's work[41].

3.2.3 Dose calculations with CadPlan 6.7.2

In this work, the version 6.7.2 of CadPlan was used to calculate isodose distributions on CT images of homogeneous, heterogeneous and anthropomorphic phantoms with a Varian CL2300 C/D 12 MeV electron beam of field size 10x10 cm^2 at a source to surface distance (SSD) of 100 cm. The CT images were the same as those used in the XVMC simulations.

The data input in the CadPlan station consisted of percent depth doses for open and blocked field as well as electron field size factors (*i.e.* ratios of the maximum dose for the field of interest over the maximum dose for the reference field) for CL2300 12 MeV electron beam. These values were determined by the clinical staff of the Montreal General Hospital from measurements performed with an IC-10 ionization chamber. CadPlan uses this data to model the beam at the bottom of the linac's head. Then, accessorizes are added; in our case, the electron cutouts were simulated using the "autoblock" component available in the CadPlan system. CadPlan yields the results under the form of a dose matrix. The thickness of the CT slice determines the dimension of the voxels in one direction. In the other two directions, the size of the voxels was set to 2.5 mm as a trade-off between accuracy and total volume of the phantom where the dose is actually calculated. Stopping power corrections were applied using the values of the report TG-21[42]. The effective depth correction explicated in Equation 3.16 was the only correction applied to account for heterogeneities. 100 MU were delivered and the dose calculated was not renormalized. The dose distribution only was calculated. Calculations

of cutout factors by CadPlan were not investigated considering they have been proven unreliable[37].

The dose matrix was exported from the CadPlan station and analyzed with a Matlab routine which permits to overlap the isodose distributions, profiles and PDDs with those obtained from XVMC as well as measured data. For easier comparison with measurements, the dose to water obtained by CadPlan was divided by the dose to solid water at z_{max} obtained by CadPlan and multiplied by the linac output in solid water for 10x10 cm^2 in solid water at z_{max}, 96.2 ± 2.1 cGy / 100 MU.

3.3 Equipment and experimental techniques

All measurements were performed with a linear accelerator CL2300C/D (Varian Oncology Systems, Palo Alto, CA) with the gantry exactly vertical above the phantom at a source-to-surface distance (SSD) of 100 cm. The collimator was rotated by 90°, the multi-leaf collimator was fully retracted and the collimator setting was automatically adjusted by the machine according to the electron applicator inserted. The dose rate was consistently set to 400 MU/min, in order to avoid issues of dependence of the detector response on the dose rate and fluctuations of the linac with the dose rate. The output of the linac was calibrated according to the recommendations of the TG-51 protocol[43] and set to deliver a dose of 101.1 ± 2.0 cGy to water per 100 monitor units (MU) at z_{max} for each energy with a 10x10 cm^2 reference field at an SSD of 100 cm.

3.3.1 Measurement of PDDs and profiles in homogeneous phantoms

PDDs and profiles were measured using a p-Si electron diode (Scanditronix, Uppsala, Sweden) scanned through a 60x60x60 cm^3 water tank with a Wellhöfer Dosimetrie acquisition system (Schwarzenbruck, Germany). The small collecting volume of the diode (2.5 mm diameter x 50 μm) along with a favorable signal-to-noise-ratio motivated the choice of the diode to measure profiles and PDDs especially for small fields or regions with steep dose gradients. Furthermore, the water-to-silicon stopping power ratio is relatively constant with depth for broad beams. It is therefore unnecessary to correct systematically the percent depth ionization (PDI) for its variations, except for

narrow fields[44] for which stopping power ratio variations were obtained in this work by Monte Carlo calculations. Moreover, Scanditronix p-Si diodes were proven[45] to exhibit the smallest dependence on the dose rate and source-to-detector distance of all commercially available diodes. As a consequence of accumulated dose, atoms can be displaced in the silicon lattice and create imperfections acting as traps. The sensitivity of the silicon detector worsens and becomes dependent on the dose rate of a pulsed linac. However, this radiation-induced damage appears mostly for detectors used in high energy photon beams[46], where neutrons are present due to photonuclear reactions initiated in the linac head by photons of energy above 10 MV. Considering that the p-Si diode used in this study is devoted to electron beam dosimetry, where the electron beams are contaminated mostly by low-energy photons, the radiation damage is expected to be limited. Nevertheless, the diode was compared to other detectors before use in our study. Schematics of the diode geometry are presented in Figure 3.14.
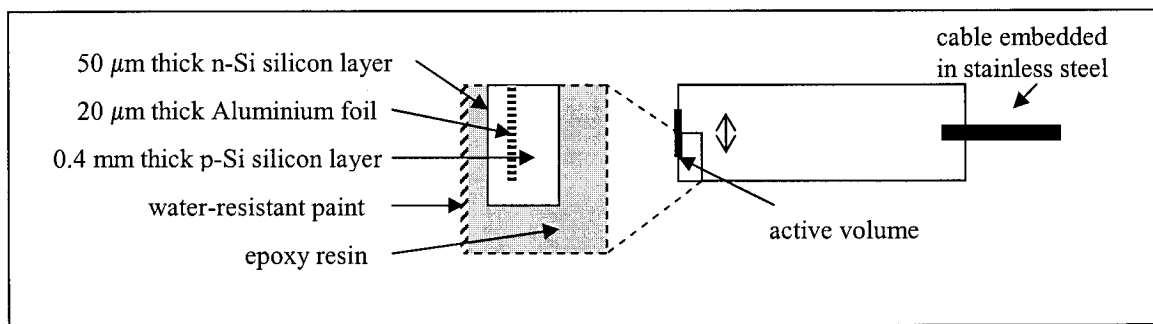
Figure 3.14: Schematics of the geometry of the electron diode p-Si.

Moreover, the effective volume and effective point of measurement of diodes are usually not precisely known. For this reason as well as because of the potential dose rate dependence, ICRU 35[47] and TG-25[48] recommend to compare the diode to other detectors, particularly through ionization chamber measurements of depth dose. Therefore, a PDD in a homogeneous water phantom was measured with the p-Si diode, a parallel-plate Roos chamber and a cylindrical chamber Exradin A12 for a 6 MeV electron beam of 10x10 cm^2. Diode measurements were shifted downstream to the effective point measurement of 0.55 mm as specified by the manufacturer and corrected for water-to-silicon stopping power ratio calculated using SPRRZ. The data measured with the

ionization chambers was shifted upstream according to the TG-51 recommendations and corrected for polarity effect and water-to-air stopping power ratio calculated according to Burns' formula[49],

$$\left(\frac{L}{\rho}\right)_{air}^{water}(z, R_{50}) = \frac{a + b(\ln R_{50}) + c(\ln R_{50})^2 + d(z/R_{50})}{1 + e(\ln R_{50}) + f(\ln R_{50})^2 + g(\ln R_{50})^3 + h(z/R_{50})} \tag{3.17}$$

where a=1.0752, b=-0.50867, c=0.088670, d=-0.08402, e=-0.42806, f=0.064627, g=0.003085 and h=-0.12460 and R_{50} and z are expressed in cm. As appears in Figure 3.15, the measurements match adequately, except in the build-up region where the diode underestimates the dose by 3% with respect to the ionization chambers. This result concurs with the findings of Shortt[50], namely the diode underestimates by a few percent the dose at shallow depths. Therefore, it is important to bear this issue in mind when analyzing PDDs measured with the diode.
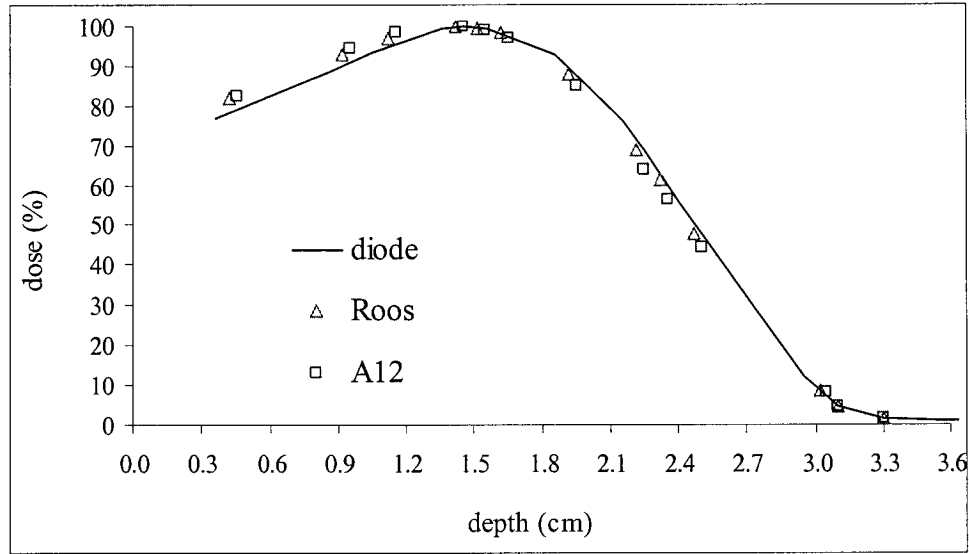
Figure 3.15: Comparison of the PDD for 6 MeV, 10x10 cm² as measured with a p-Si diode (continuous line), a Roos chamber (△) or an Exradin A12 chamber (□).

The diode was placed vertically in the beam for both PDDs and profiles to avoid any directional dependence of the detector's response to the radiation, although it is known to be small. The top of the diode was aligned with the water surface and the measurements were then systematically shifted downstream by 0.55 mm, approximately the water-equivalent thickness of the epoxy-resin layer which covers the collecting

volume. The PDDs and profiles were collected with an adaptive step length resulting in a resolution of 0.5 to 2 mm in regions of steep dose gradient and 3 to 5 mm in the bremsstrahlung tail.

The main source of uncertainty in these measurements lies in the inaccurate knowledge of the actual depth of measurement rather than dosimetry issues *per se*. The initial positioning of the diode to assess the depth origin was complicated by the surface tension of the water. Moreover, a drift in the scanning system was noted, which necessitated regular checks of the diode position with respect to the surface. Overall the uncertainty on the depth was estimated to 1 mm, which translates to an error of 1-3% of the dose maximum for doses in the plateau region and up to 8% for local doses in the fall-off region.

3.3.2 Measurement of cutout factors in homogeneous phantoms

Cutouts of various shapes and dimensions were constructed for this project. They were made out of a low melting temperature alloy called cerrobend which has an effective atomic number 74.8 and physical density 9.76 g/cm^3. The alloy consists of bismuth (50%), lead (26.7%), tin (13.3%) and cadmium (10%). With the knowledge that 1 cm of cerrobend stops 20 MeV electrons, the thickness of the cutouts was chosen of 1.7 cm to limit the amount of transmitted radiation to a few percent of the incident intensity. Cutout factors were measured using the same p-Si electron diode as that used to measure the PDDs and profiles, in the water tank at an SSD of 100 cm. Based on preliminary knowledge of the depth of maximum dose deduced from the measured PDDs for a given field, the central axis was systematically rescanned in depth with a resolution of 1 to 2 mm until the depth of maximum dose was precisely determined. The charge collected at z_{max} for a 100 MU irradiation averaged over 4 irradiations was normalized to the corresponding signal for the reference field of 10x10 cm^2 obtained with a 10x10 cm^2 steel insert in the 10x10 cm^2 applicator. The charge obtained in the reference field was systematically re-read immediately after the measurement of the charge for the field of interest so that the measurements were unaffected by a possible short-term dependence of the diode response on accumulated dose. Variations of the water-to-silicon stopping power ratio with depth were ignored. The leakage of the diode over the irradiation time

was negligible compared to the signal. For cutouts not centered on the central axis of the beam, profiles were acquired to determine the lateral position where the maximum dose was delivered and then, the percent depth dose was measured along a vertical line intercepting that off-axis point, as illustrated in Figure 3.16.
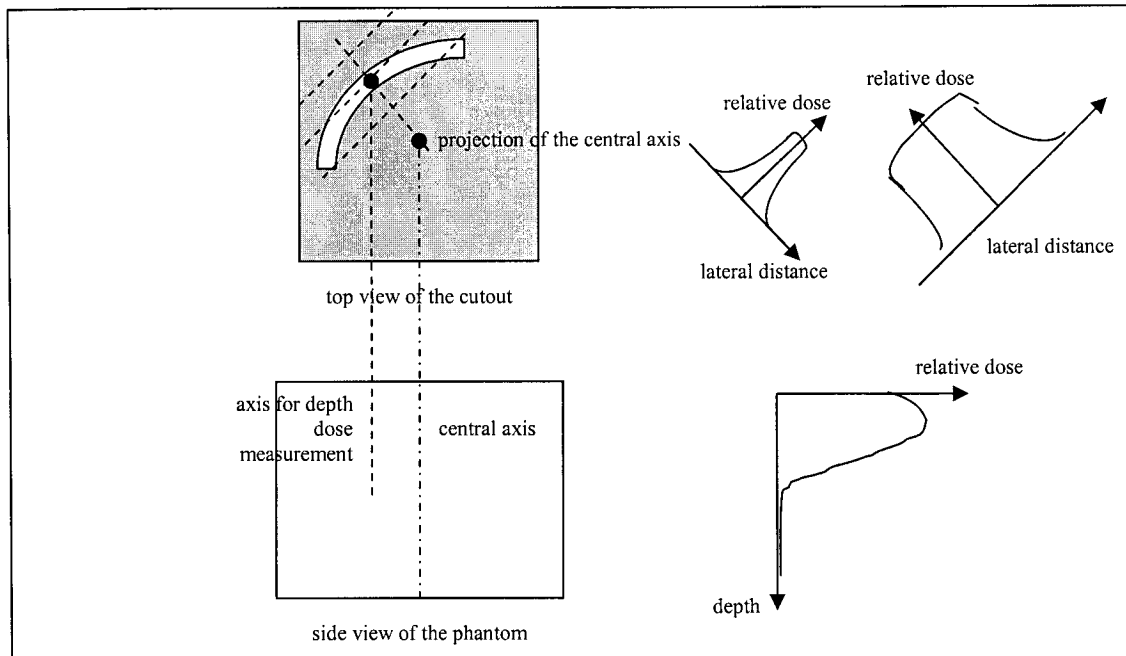
Figure 3.16: Schematic illustration of the measurement of the cutout factor for off-axis cutouts.

3.3.3 Measurement of dose distributions in heterogeneous phantoms

In this section, the equipment including phantoms and detectors is first described, then the manipulations performed with the TLDs are presented, finally the method for conversion of the dose to the detector to the dose to the medium is detailed.

The effect of the variation of the linac output was accounted for by correcting for the difference between the average output during the calibrations and the output during the measurement. Furthermore, to facilitate the comparison with simulations, the measured dose to medium in the heterogeneous phantoms was divided by the dose to solid water at z_{max} obtained by calibration and multiplied by the linac output in solid water for 10x10 cm^2 in solid water at z_{max}, 96.2 ± 2.1 cGy / 100 MU.

All phantoms are irradiated with 100 MU of a 12 MeV electron beam of dimensions 10x10 cm^2 at an SSD of 100 cm with a dose rate of 400 MU/min.

3.3.3.a Experimental set-up

The dose inside two rectangular phantoms with a 1-dimensional heterogeneity and an anthropomorphic phantom was measured using LiF thermoluminescent dosimeters of the type TLD-700 (chips) and TLD-100 (rods) respectively (Harshaw Chemical Company, Solon, OH). The small dimensions of the detectors (3.2x.3.2x0.15 mm^3 and 6x1x1mm^3 respectively) ensure a high resolution near and inside the heterogeneities. All phantom irradiations were performed with a 10x10 cm^2 beam of energy 12 MeV. 12 MeV is an energy commonly encountered in clinical head and neck cases with a practical range of 6.2 cm and R_{50} of 3.9 cm. Using this energy to irradiate our phantoms has the consequence that the beam extends beyond the depth of the heterogeneities allowing to study their effect.

The rectangular phantoms with a 1-dimensional heterogeneity contained a 3 cm thick layer of bone or lung embedded in solid water at 1 cm depth, with 21 cm back-up material to provide sufficient backscatter, as illustrated in Figure 3.17. Measurements in the anthropomorphic phantom are performed in the head of the Alderson Rando phantom (Vertec, Aldermaston, UK), a picture of which can be seen in Figure 3.18. The uncertainty in the positioning of the TLDs in this phantom was estimated to about ±1.5 mm.
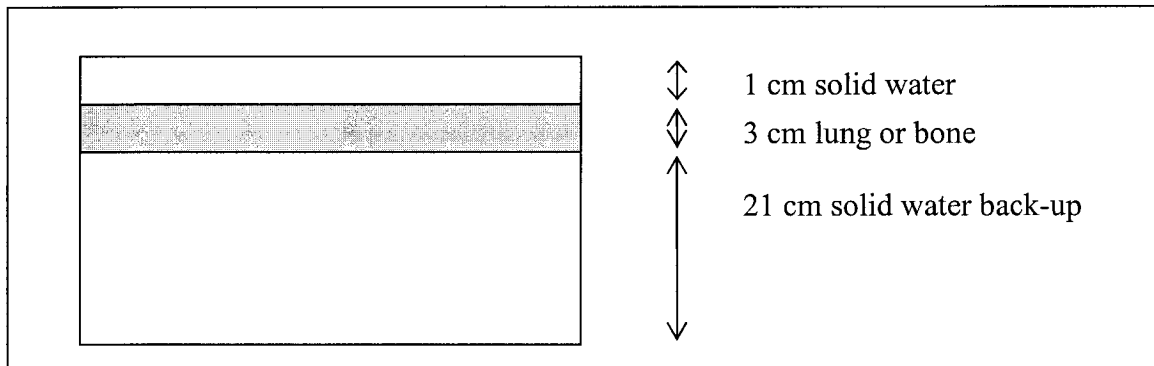
Figure 3.17: Geometry of the heterogeneous phantoms.

70
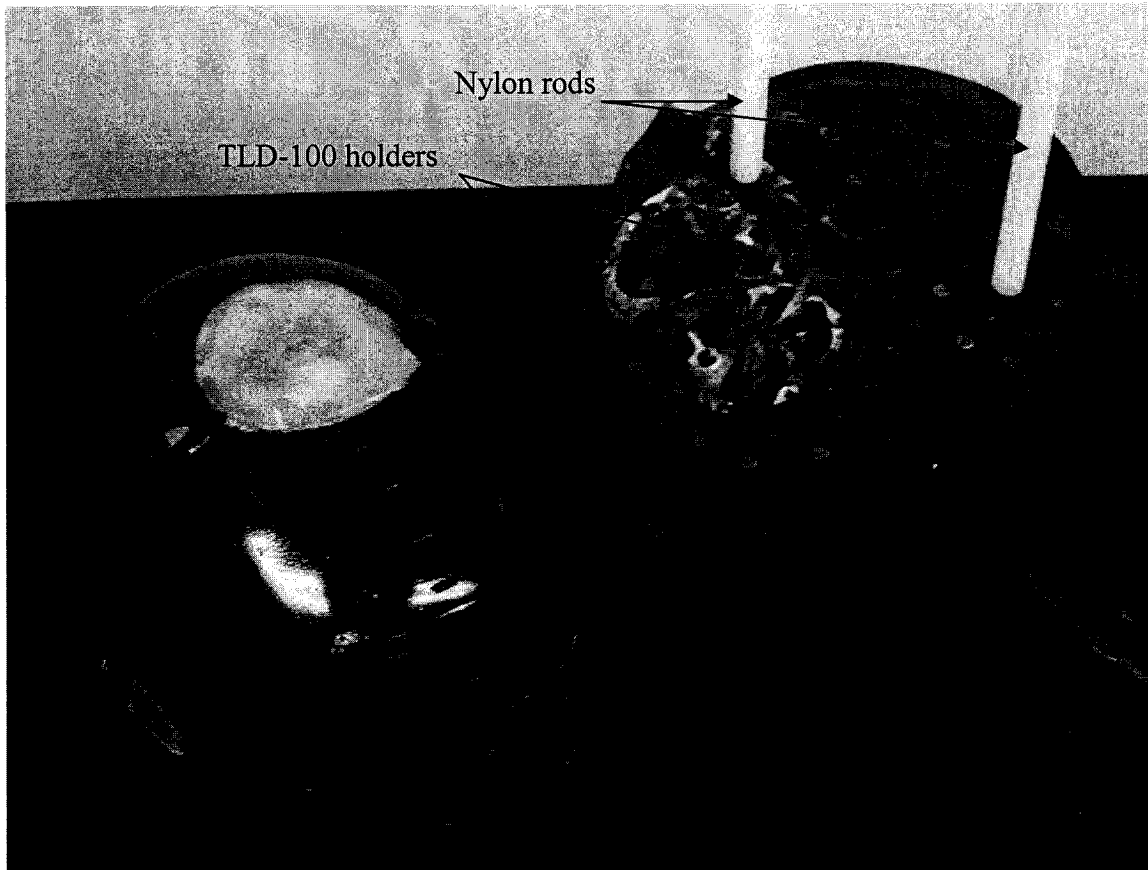
Figure 3.18: Photograph of the head of the Alderson Rando anthropomorphic phantom with the TLD holders.

The physical density and composition of the materials provided by Gamex-RMI (Middleton, WI) listed in Table 3.2 were used in the Monte Carlo simulations. The TLDs are made of lithium fluoride (Li: 26.76%, F: 73.24%, ρ=2.635 g/cm^3). TLD-700 contains approximately 99.99% of ^{7}Li and 0.01% of ^{6}Li. Consequently, TLD-700 is sensitive to gamma and beta radiation, whereas TLD-100 is also sensitive to thermal neutrons due to the presence of 0.5 % of ^{6}Li which has a large cross-section for thermal neutrons capture.

material	H	C	N	O	Cl	Ca	Physical density (g/cm^3)
Lung (RMI-455)	8.62	68.87	2.26	17.62	0.11	2.52	0.27
Solid water^{TM} (RMI-457)	8.09	67.22	2.40	19.84	0.13	2.32	1.045
Bone (RMI-450)	3.10	31.26	0.99	37.57	0.05	27.03	1.84

Table 3.2: Percentage composition by weight and physical density of the phantom materials

3.3.3.b Measurement procedure

Prior to each irradiation, the TLDs were annealed at 400°C for 1 hour followed by 100°C for 2 hours and cooled at room temperature, in order to remove all stored charges. The TLDs were then irradiated in the phantom at an SSD of 100 cm with a 12 MeV electron beam of dimension 10x10 cm^2. Sufficient time (40 hours for TLD-700 and 16 hours for TLD-100) was allowed between irradiation and reading to let the low temperature peaks of the glow curve vanish. The TLDs were read using a Harshaw QS 3500 TLD reader (Harshaw Chemical Company, Solon, OH). The read-out cycle consisted of the following steps: the TLDs are first preheated to 50°C for 10 seconds, then heated to 300°C for 30 sec at a heating rate of 12°C/sec, then annealed at 300°C for 10 sec and finally cooled back to the initial 50°C. The experimental protocol is summed up in Figure 3.19.
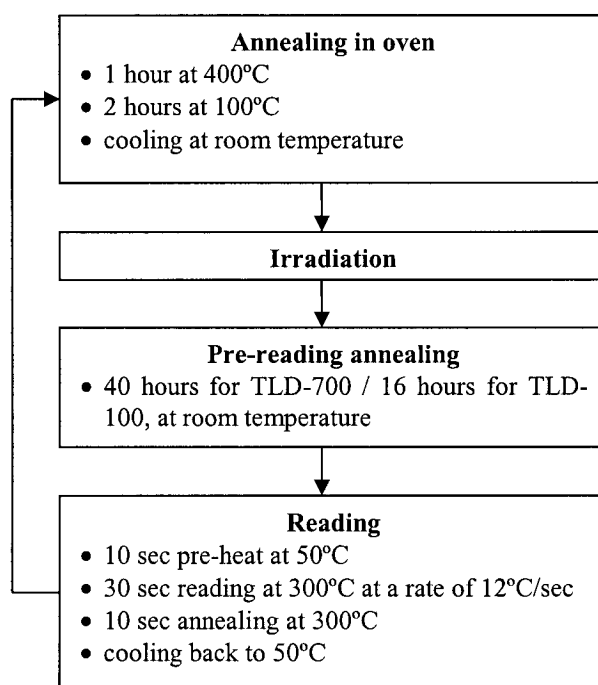
Figure 3.19: Irradiation and read-out protocol for TLD experiments.

The linearity of the TLDs' response to radiation was investigated by averaging the reading of 4 TLDs to doses ranging from 0 to 200 cGy after irradiation in calibration conditions. As confirmed by Figure 3.20, the detectors have a linear response to radiation up to 130 cGy. Beyond 130 cGy, the response of the detector becomes supra-linear,

therefore irradiation was limited to 100 MU in all experiments, which corresponds to 101.1 ± 2.0 cGy in water at z_{max} for a 10x10 cm^2 reference field.
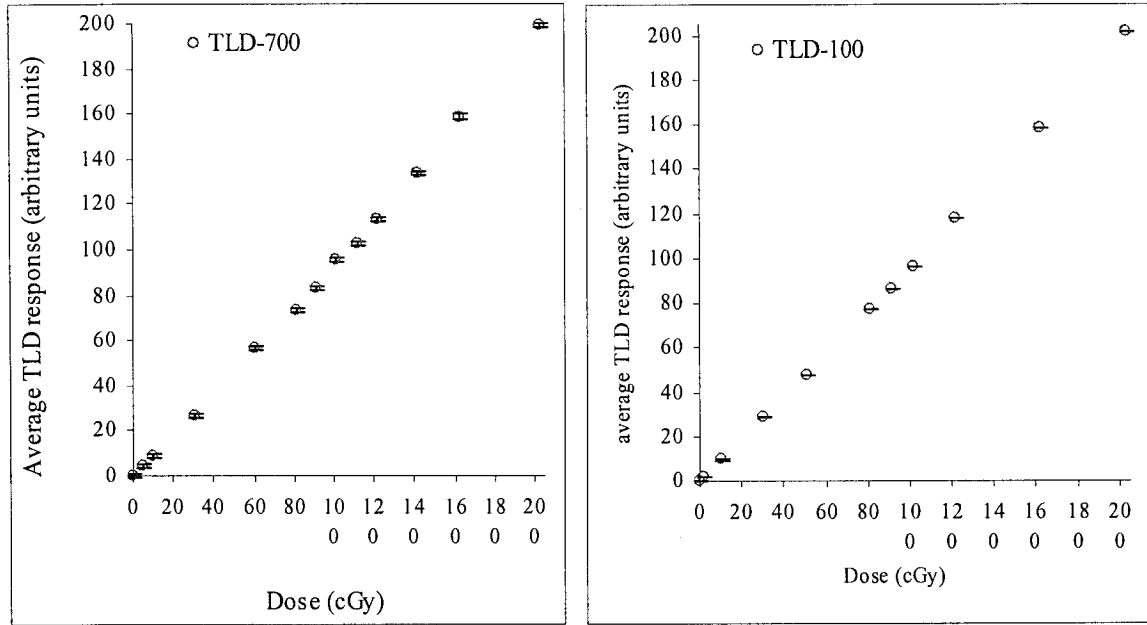
Figure 3.20: Linearity of the response to absorbed dose of TLD-700 (left) and TLD-100 (right).

The reproducibility of the TLDs was tested by performing multiple calibrations consisting of irradiation of a homogeneous solid water phantom with the TLDs placed at z_{max} (2.8 cm for 12 MeV). The signal of each TLD in response to the same dose is expected to have random statistical fluctuations of 2% or more over time according to the manufacturer. However, the average standard deviation of the TLD readings reached 4.1% for TLD-700 and 1.5% for TLD-100. This lack of reproducibility is circumvented by systematically renormalizing the dose measured at a TLD by the average dose received by four control TLDs irradiated in the calibration conditions during each experiment. The variation of the sensitivity of the TLD with repeated irradiations was examined by plotting the reading of five individual detectors as a function of cumulated dose, as presented in Figure 3.21. A similar behavior was observed for the other TLDs. The observed decrease of up to 15% in the TLD response could be attributed to radiation-induced and manipulation-induced damage of the detector material. To circumvent this

problem, each TLD was assigned an individual calibration factor N determined from two calibrations performed respectively before and after each PDD measurement.
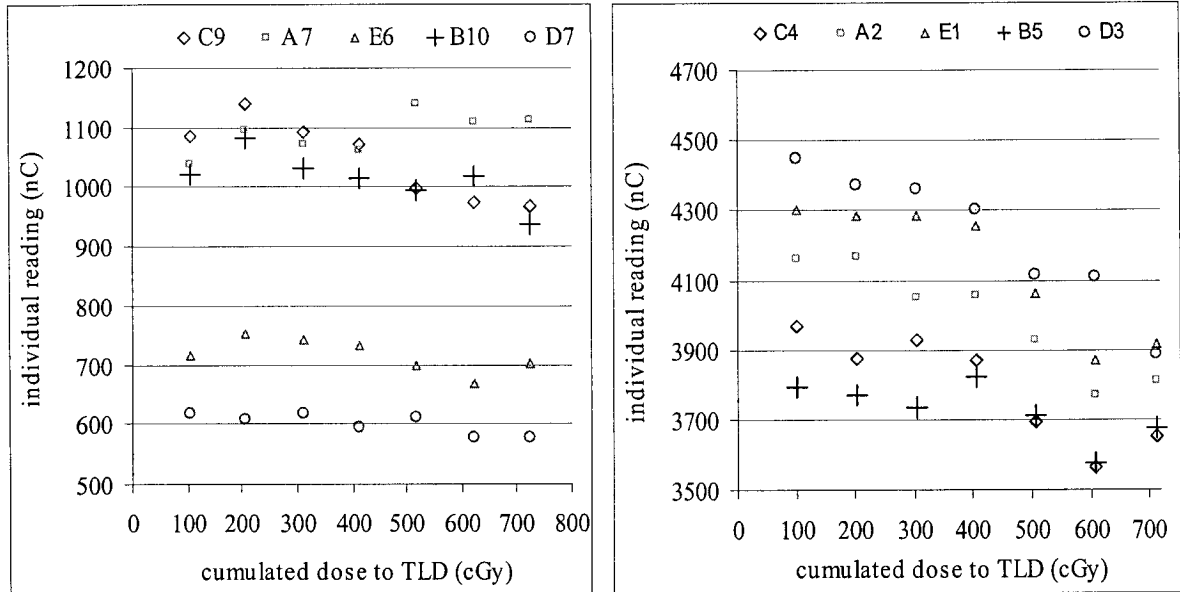
Figure 3.21: Sensitivity of the reading to cumulated dose for TLD-700 (left) and TLD-100 (right) for random TLDs.

All points on the central-axis depth dose in the rectangular phantoms are the average of the doses absorbed by eight TLDs (two experiments with four TLDs each kept at the same depth), whereas the points from the dose distribution in the anthropomorphic phantom are obtained by averaging the results of four experiments. Furthermore, all dose values were corrected for the potential difference between the dose per 100 MU given on the day of the experiment compared to that given during calibration as determined by measurement of the dose at z_{max} under calibration conditions with a PTW Farmer chamber. This correction amounted to less than 0.8% in all cases.

3.3.3.c Conversion of dose to detector to dose to medium

For the measurements in heterogeneous phantoms, a conversion of the measured data from dose to the dosimeter to dose to the phantom material itself is essential. Due to their small size relative to the range of the electrons, TLDs behave as cavities[51,52] and the

dose to the medium should be deduced from the dose to TLD by applying the Bragg-Gray cavity theory described in section 2.1.4.

> ➢ **General equation**

The dose to the medium is obtained from the reading through the calibration factor as well as stopping power ratio and fluence corrections. The dose to medium is converted from the dose to detector using the Spencer-Attix cavity theory, as follows,

$$D_{med}(z) = D_{det,\,med}(z) \cdot \left(\overline{L/\rho}\right)_{med}^{det}(z) \cdot \Phi_{med}^{det}(z) , \qquad (3.18)$$

where $D_{med}(z)$ is the dose to the medium at the depth z, $D_{det,med}(z)$ is the dose to the detector in the medium at depth z, $\left(\overline{L/\rho}\right)_{med}^{det}(z)$ is the restricted mass collision medium-to-detector stopping power ratio at depth z and $\Phi_{med}^{det}(z)$ is a term correcting for the electron fluence perturbation introduced by the presence of the detector in the medium at depth z. The dose to the detector is deduced from the reading of the TLD at z, $R_{det,med}(z)$, through the calibration factor N_{det} in the following fashion,

$$D_{det,\,med}(z) = R_{det,\,med}(z) \cdot N_{det} \qquad (3.19)$$

and
$$N_{det} = \frac{D_{det,\,sw}(z_{max})}{R_{det,\,sw}(z_{max})}, \qquad (3.20)$$

where $D_{det,sw}(z_{max})$ is the dose to the detector in the homogeneous phantom at depth of calibration z_{max} and $R_{det.sw}(z_{max})$ is the reading of the TLD after calibration. According to Equation 3.18, the dose to the detector in the homogeneous phantom at z_{max} is linked to the dose in the homogeneous phantom at the same depth $D_{det,sw}(z_{max})$ by

$$D_{det,\,sw}(z_{max}) = \frac{D_{sw}(z_{max})}{\left(\overline{L/\rho}\right)_{det}^{sw}(z_{max}) \cdot \Phi_{det}^{sw}(z_{max})} \qquad (3.21)$$

and
$$D_{sw}(z_{max}) = R_{det,\,sw}(z_{max}) \cdot N_{sw} , \qquad (3.22)$$

where N_{sw} is the calibration factor and $\Phi_{det}^{sw}(z_{max})$ is the phantom to detector fluence ratio at z_{max}.

$$D_{med}(z) = N_{det} \cdot R_{det,med}(z) \cdot \left(\overline{L/\rho}\right)_{det}^{med}(z) \cdot \Phi_{det}^{med}(z) \qquad (3.23)$$

$$D_{med}(z) = N_{sw} \cdot R_{det,med}(z) \underbrace{\frac{\left(\overline{L/\rho}\right)_{det}^{med}(z) \cdot \Phi_{det}^{med}(z)}{\left(\overline{L/\rho}\right)_{det}^{sw}(z_{max}) \cdot \Phi_{det}^{sw}(z_{max})}}_{\substack{\text{Stopping power} \quad \text{Fluence perturbation} \\ \text{ratio correction} \quad\quad \text{correction}}} \qquad (3.24)$$

➤ Determination of the fluence perturbation correction

The fluence perturbation correction in the slab phantoms was obtained with the DOSXYZnrc user code by simulating the geometry of the calibration phantom and of the heterogeneous phantom in the presence and in the absence of the TLD, as illustrated in Figure 3.22. It was then calculated as the ratio of the dose to the medium at depth z, $D_{med}(z)$, to the dose to the TLD in the medium, $D_{det,med}(z)$, corrected by the restricted collision medium-to-TLD stopping power ratio, $(\overline{L/\rho})_{det}^{med}(z)$ at the same depth z,

$$(P_{flu})_{det}^{med}(z) = \frac{D_{med}(z)}{D_{det,med}(z) \cdot (\overline{L/\rho})_{det}^{med}(z)} .$$ (3.25)
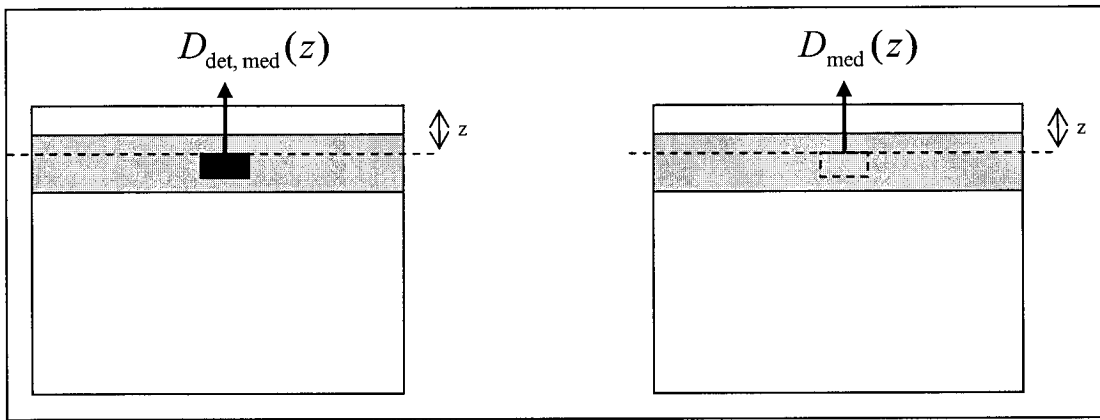
Figure 3.22: Geometry of phantoms in DOSXYZnrc simulations of TLD measurements in calibration and heterogeneous phantoms.

The fluence perturbation correction is neglected in the solid water phantom. However, it is important to correct for fluence perturbation in phantoms with lung and bone heterogeneities[53], because of larger attenuation of the beam in the denser TLD material, especially when a large heterogeneity is situated in a region of high dose gradient, like in the cases studied in this work. The fluence perturbation corrections thus obtained for the lung and bone slab phantoms are plotted in Figure 3.23, as well as the stopping power ratio corrections calculated as described in the next section. No fluence perturbation correction was applied to the TLD-100 measurements in the Alderson Rando phantom. This is due to the fact that, at present, we do not have a defined procedure to calculate ratios of restricted medium-to-dosimeter stopping powers, for phantoms derived from CT images.

➢ **Determination of the stopping power ratio correction**

The medium-to-lithium-fluoride stopping power ratio for the slab phantoms was calculated with the Monte Carlo user code SPRRZnrc in the homogeneous phantom without detectors. The cylindrical scoring region was designed so that its surface area is equivalent to the area of the rectangular TLD chip. The energy threshold for production of secondary particles (AE) and the electron kinetic energy cut-off (ECUT) were set to 235 keV for TLD-700 and 931 keV for TLD-100, energy required by the electrons to travel in solid water by the average chord length of the detectors. The average chord length (6 mm for TLD-700, 4 mm for TLD-100) is obtained by quadrupling the ratio of the volume over the surface area of the detector, as suggested by Weinberg and Wigner[54]. The variation of stopping power ratio correction versus depth in phantom, shown in Figure 3.23, amounted to +5% in lung and -9% in bone, whereas it was constant to within 0.2% for Solid Water™. As pointed out, no correction was applied for fluence or medium-to-LiF stopping power ratio in the anthropomorphic phantom.
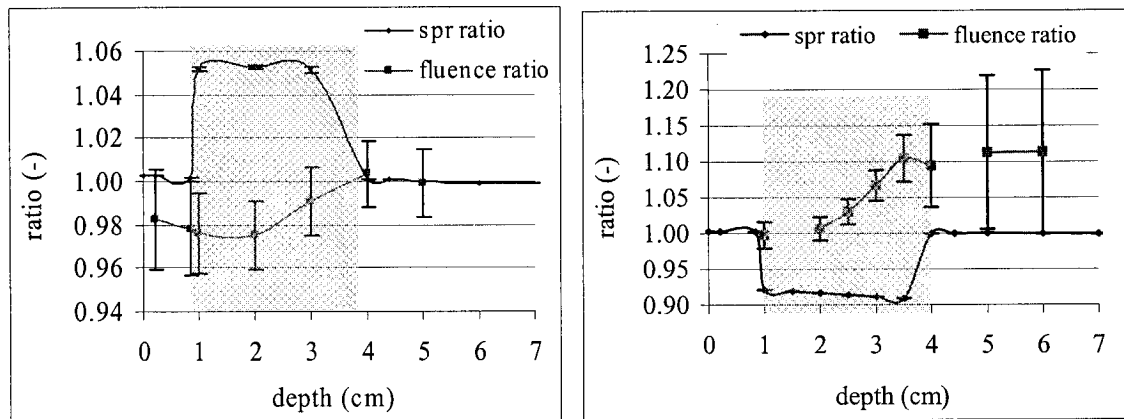
Figure 3.23: Medium-to-LiF fluence perturbation correction (■) and stopping power ratio (●) normalized to the corresponding value of the solid water-to-LiF ratio for TLD-700 in the lung phantom (left) and the bone phantom (right).

References:

[1] M. J. Berger and S.M. Seltzer, "ETRAN, Monte Carlo code system for electron and photon transport through extended media", *Documentation for RSIC Computer Code Package CCC-107* (Oak Ridge Natl. Lab., Oak Ridge, Tennessee, 1973)

[2] R. L. Ford, W. R. Nelson, "The EGS Code System (Version 3)", SLAC Rep. 210 Stanford University, Stanford, California (1978)

[3] M. J. Berger, "Monte Carlo calculation of the penetration and diffusion of fast charged particles", Methods Comput. Phys. **1**, 135-215 (1963)

[4] B. R. B. Walters, I. Kawrakow, D. W. O. Rogers, "History by history statistical estimators in the BEAM code system", Med. Phys. **29** (12), 2745-2752 (2002)

[5] D.W.O. Rogers and A.F. Bielajew, "Monte Carlo Techniques of Electron and Photon Transport for Radiation Dosimetry" in *The Dosimetry of Ionizing Radiation*, Ed Academic Press, New York (1990)

[6] I. Kawrakow, "Accurate condensed history Monte Carlo simulation of electron transport. I EGSnrc, the new EGS4 version," Med Phys **27** (3), 485-498 (2000)

[7] I. Kawrakow, D. W. O. Rogers, "The EGSnrc System, Status report" from Advanced Monte Carlo for Radiation Physics, Particle Transport Simulation and Applications: Proceedings of the Monte Carlo 2000 Conference, Lisbon, 23-26 October 2000, Springer, Berlin, 2001. Eds A. Kling, F. Barao, M. Nakagawa, L. Travora, P. Vaz

[8] I. Kawrakow and D.W.O. Rogers, "The EGSnrc Code System: Monte Carlo Simulation of Electron and Photon Transport," NRCC Reports PIRS-701, NRC Canada (2001)

[9] E. Storm and H. Israel, "Photon cross-sections from 1 keV to 100 MeV for elements $Z=1$ to $Z=100$", *At. Data Nucl. Data Tables* **7**, 565-681 (1970)

[10] F. Hobeila, J. P. Seuntjens, "Effect of XCOM photoelectric cross-sections on dosimetric quantities calculated with EGSnrc", in *Standards and codes of practice in medical radiation dosimetry*, Vol. 1, International Atomic Energy Agency, Vienna (2003)

[11] M. J. Berger, J. S. Coursey, M. A. Zucker, "ESTAR, ASTAR and PSTAR: Computer Programs for Calculating Stopping-Power and Range Tables for Electrons, Protons, and Helium Ions (version 1.21)", NIST Report NISTIR-4999, Washington, DC (1992) and online: http://physics.nist.gov/Star, National Institute of Standards and Technology, Gaithersburg, MD (1999)

[12] R. M. Sternheimer, "Density effect for the ionization loss of charged particles in various substances", Atom. Data and Nucl. Data Tables **30**, 261-271 (1984)

[13] A. F. Bielajew, "HOWFAR and HOWNEAR: Geometry Modeling for Monte Carlo Particle Transport," NRCC Reports PIRS-0341 (1995)

[14] D. W. O. Rogers, B. A. Faddegon, G. X. Ding, C. M. Ma, J. Wei, T. R. Mackie, "BEAM: A Monte Carlo code to simulate radiotherapy treatment units", Med. Phys. **22** (5), 503-524 (1995)

[15] D.W.O. Rogers, C. M. Ma, G. X. Ding, B. Walters, "BEAM Users Manual", National Research Council of Canada Report No. PIRS-0509A, (NRCC, Ottawa, Canada, 1995) available online at http://www.sao.nrc.ca/inms/irs/BEAM/users_manual/beamnrc_um/

[16] A. Kosunen, D. W. Rogers, "Beam quality specification for photon beam dosimetry", Med. Phys. 20, 1181-1188 (1993)

[17] A. E. Nahum, "Water/air stopping-power ratios for megavoltage photon and electron beams", Phys. Med. Biol. **23**, 24-38 (1978)

[18] I. Kawrakow, M. Fippel, K. Friedrich, "3D electron dose calculation using a Monte Carlo algorithm (VMC)", Med. Phys. **23** (4), 445-457 (1996)

[19] ICRU, "Photon, Electron, Proton, and Neutron Interaction Data for Body Tissues", ICRU Report No. 46, International Commission on Radiation Units and Measurements, Washington, D.C. (1992)

[20] M. Fippel, "Fast Monte Carlo dose calculation for photon beams based on the VMC electron algorithm", Med. Phys. **26** (8), 1466-1475 (1999)

[21] G. X. Ding, "Energy spectra, angular spread, fluence profiles and dose distributions of 6 and 18 MV photon beams: results of Monte Carlo simulations for a Varian 2100EX accelerator", Phys. Med. Biol. **47**, 1025-1046 (2002)

[22] IAEA, "The Use of Plane Parallel Ionization Chambers in High Energy Electron and Photon Beams: An International Code of Practice for Dosimetry," Technical Report Series Vol. 381, International Atomic Energy Agency, Vienna (1997)

[23] D. W. O. Rogers, I. Kawrakow, B. Walters, "Revised relationship between R_{50} and E_0 for electron beams", Conf. Proc. Of the IEEE 2000 (2000)

[24] ICRU, "Stopping Powers for Electrons and Positrons", ICRU Report No. 37, International Commission on Radiation Units and Measurements, Washington, D.C. (1984)

[25] G. G. Zhang, D. W. O. Rogers, J. E. Cygler, T. R. Mackie, "Monte Carlo investigation of electron beam output factors versus size of square cutout", Med. Phys. **26** (5), 743-750 (1999)

[26] F. Verhaegen, R. Symonds-Tayler, H. H. Liu, A. E. Nahum, "Backscatter towards the monitor ion chamber in high-energy photon and electron beams: charge integration versus Monte Carlo simulation", Phys. Med. Biol. **45**, 3159-3170 (2000)

[27] R. Doucet, M. Olivares, F. DeBlois, E. B. Podgorsak, I. Kawrakow, J. Seuntjens, "Comparison of measured and Monte Carlo calculated dose distributions in homogeneous phantoms in clinical electron beams", Phys. Med. Biol. **48** (15), 2339-2354 (2003)

[28] F.M. Khan, "Dose Distribution Algorithms for Electron Beams", Chapter 6 part B of _Treatment Planning in Radiation Oncology_, F.M. Khan and R.A. Potish (William and Wilkins, Baltimore, 1998)

[29] K. R. Hogstrom, M. D. Mills, P. R. Almond, "Electron beam dose calculations", Phys. Med. Biol. **26** (3), 445-459 (1981)

[30] ICRU, "Radiation dosimetry: Electrons with Initial Energies Between 1 and 50 MeV", ICRU Report No. 21, International Commission on Radiation Units and Measurements, Washington, D.C. 1972

[31] J. E. Cygler, J. J. Battista, J. W. Scrimger, E. Mah, J. Antolak, "Electron dose distributions in experimental phantoms: a comparison with 2D pencil beam calculations", Phys. Med. Biol. **32** (9), 1073-1086 (1987)

[32] I. Lax, "Development of a generalized Gaussian model for absorbed dose calculation and dose planning in therapeutic electron beams", _Ph.D._ Thesis, Stockholm University (1986)

[33] S. Hyödynmaa, "Three-dimensional implementations of the generalized Gaussian pencil beam algorithm for electron beam, dose planning", _Ph.D._ Thesis, Technical Research Centre of Finland, Publications 74, Espoo (1991)

[34] S. Hyödynmaa, "Dose computation for irregular and blocked electron beams with the generalized Gaussian pencil beam ", _Proc. 1st European CadPlan users' meeting_, Luzern, November 14-15, 1991

[35] S. Hyödynmaa, "Electron beam dose computation using generalized Gaussian pencil beam algorithm with 3-D heterogeneity correction and arbitrary field shapes", _Proc. Xth International Conference on the Use of Computers in Radiation therapy_, Manchester, 1994

[36] Varian Treatment Planning Systems, *CadPlan, External Beam Modelling Physics*, Varian Medical Systems, Inc., Varian Oncology Systems (1999)

[37] D. Hodefi, "Evaluation of CadPlan for electron beam treatment planning", M. Sc. Thesis, 2004

[38] A. Brahme, I. Lax, P. Andreo, "Electron beam dose planning using discrete Gaussian beams. Mathematical background", Acta Radiol. Oncol. **20**, 147-158, (1981)

[39] I. Lax, A. Brahme, P. Andreo, "Electron beam dose planning using Gaussian beams. Improved radial dose profiles", Acta Radiol. Suppl. **364**, 49-59 (1983)

[40] I. Lax, A. Brahme, "Electron beam dose planning using Gaussian beams. Energy and spatial scaling with heterogeneities", Acta Radiol. Oncol. **24**, 75-85 (1985)

[41] H. Huizenga, P. R. M. Storchi, "The in-air scattering of clinical electron beams as produced by accelerators with scanning beams and diaphragm collimators", Phys. Med. Biol. **32**, 1011-1029 (1987)

[42] AAPM, "A protocol for the determination of absorbed dose from high-energy photon and electron beams", Task Group 21 Report, Med. Phys. **10** (6), 741-771 (1983)

[43] AAPM, "AAPM's TG-51 protocol for clinical reference dosimetry of high energy photon and electron beams", Task Group 51 Report, Med. Phys. **26** (9), 1847-1870 (1999)

[44] A. Kapur, C. M. Ma, "Stopping-power ratios for clinical electron beams from a scatter-foil linear accelerator", Phys. Med. Biol. **44**, 2321-2341 (1999)

[45] A. S. Saini, T. C. Zhu, "Dose rate and SDD dependence of commercially available diode detectors", Med. Phys. **31** (4), 914-924 (2004)

[46] D. Wilkins, X. A. Li, J. Cygler, L Gerig, "The effect of dose rate dependence of p-type silicon detectors on linac relative dosimetry", Med. Phys. **24** (6), 879-881 (1997)

[47] ICRU, "Radiation dosimetry: Electron beams with energies between 1 and 50 MeV" ICRU Report No. 35, International Commission on Radiation Units and Measurements, Bethesda, Maryland. (1984)

[48] AAPM, "Clinical Electron-Beam Dosimetry", Task Group 25 Report, Med. Phys. **18** (1), 73-109 (1991)

[49] D. T. Burns, G. X. Ding, D. W. O. Rogers, "R_{50} as a beam quality specifier for selecting stopping-power ratios and reference depths for electron dosimetry", Med. Phys. **23** (3), 383-388 (1996)

[50] K. R. Shortt, C. K. Ross, A. F. Bielajew, D. W. O. Rogers, "Electron beam dose distributions near standard heterogeneities", Phys. Med. Biol. **31** (3) 235-249 (1986)

[51] J. G. Holt, G. R. Elderstein, T. E. Clark, "Energy dependence of the response of lithium fluoride TLD rods in high energy electron fields", Phys. Med. Biol. **20** (4), 559-570 (1975)

[52] B. R. Paliwal, P. R. Almond, "Applications of cavity theories for electrons to LiF dosemeters", Phys. Med. Biol. **20** (4), 547-558 (1975)

[53] E. El-Khatib, J. Antolak, J. Scrimger, "Evaluation of film and thermoluminescent dosimetry of high-energy electron beams in heterogeneous phantoms", Med. Phys. **19** (2), 317-323 (1992)

[54] I. Weinberg, A. Wigner, "*Physical Theory of Neutron Chain Reactions*", University Chicago Press, 1958, p 715

Chapter 4. Results and discussion.

The first part of this chapter is devoted to the validation of the BEAMnrc model built for the linac CL2300 C/D (Varian) at an SSD of 100 cm. Then, the in-house EGSnrc user code CUTOUT developed for transport of particles through irregularly shaped cutouts is validated for the prediction of cutout factors and depths of maximum dose and for the determination of depth dose curves at an SSD of 100 cm. In a third section of this chapter, the implementation of the automated Monte Carlo system for calculation of cutout factors is presented. Finally, isodose distributions calculated by XVMC and CadPlan are compared to TLD measurements.

4.1 Validation of BEAMnrc model for a Varian linac CL2300 C/D

A BEAMnrc model for the linac CL2300 C/D in the electron mode was built for its six nominal energies (6, 9, 12, 15, 18 and 22 MeV) and five electron applicators (6x6, 10x10, 15x15, 20x20 and 25x25 cm^2). It was validated against measurements performed with a p-Si diode in a homogeneous water phantom at an SSD of 100 cm for calculation of central-axis percent depth dose curves, profiles and cutout factors for a large selection of fields.

4.1.1 Central-axis depth dose curves

The model was validated by comparison of the simulated PDDs with measurements at an SSD of 100 cm for a 10x10 cm^2 reference field[†] at all energies and is further verified for other field sizes. Figure 4.1 shows the good agreement between the simulated PDDs and the diode measurements within 2% relative to the maximum dose for each energy and 1 mm at the depth of R_{50}. Nevertheless, the model yields a dose higher than the diode measurements by 2.8% in the build-up region for all energies, the effect worsening with increasing energy. In section 3.3.1, the diode was shown to

---

[†] All the field sizes mentioned are specified as the dimension of the field projected at the surface of the phantom, *i.e.* at 100 cm from the source, not to the actual physical size of the cutout.

underestimate the dose in the build-up region by 2% compared to both ionization chambers Roos and Exradin A12. Comparison of the model prediction for a broad 6 MeV electron beam with the measurements performed with those ionization chambers and the diode in a Solid Water™ phantom, as depicted in Figure 4.2, proves an excellent match between the MC simulation and the measurements. The dose proposed by the model for the build-up region can therefore legitimately be trusted.
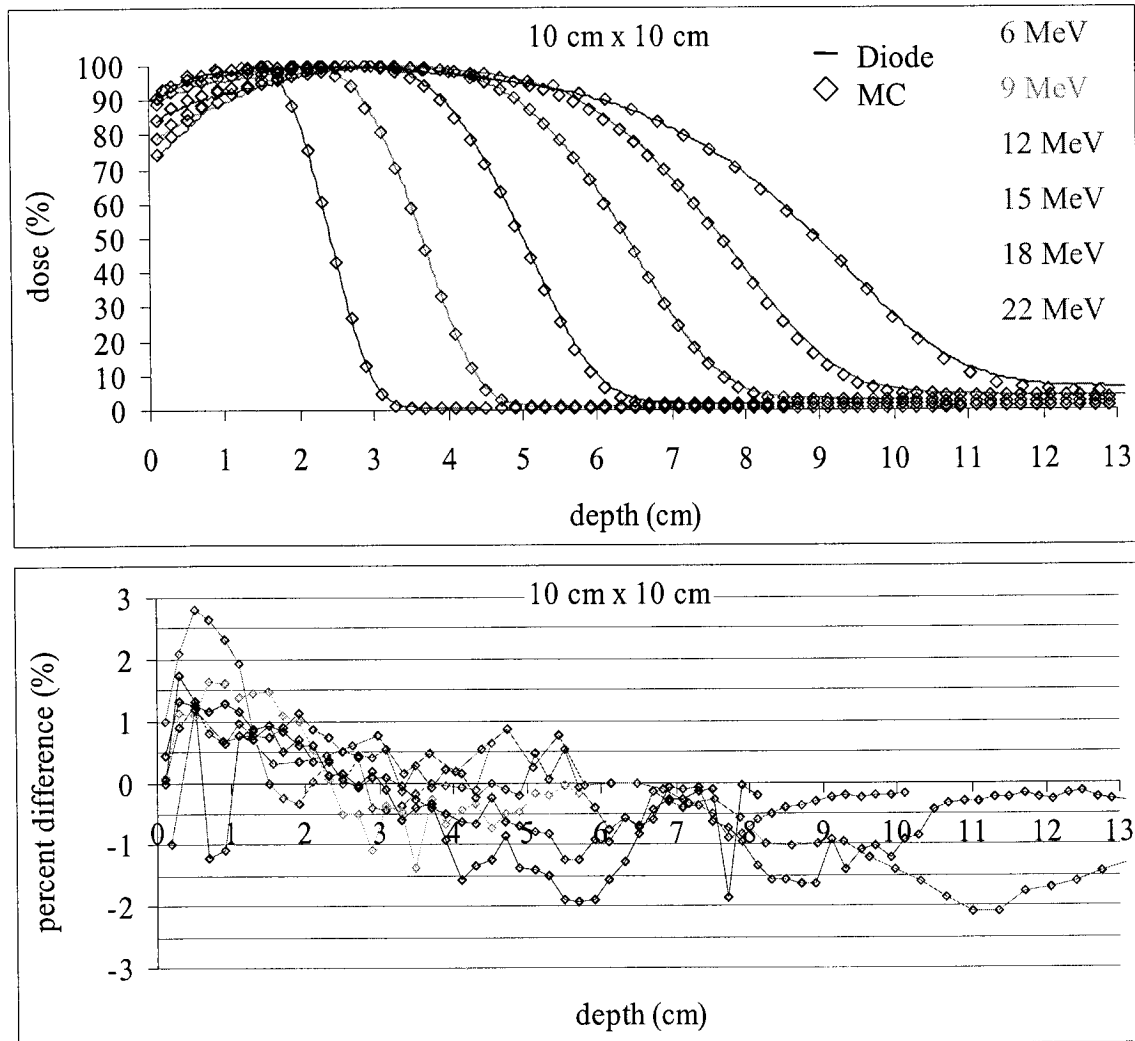
Figure 4.1: Validation of the BEAM model for calculation of central-axis percentage depth dose curves for 10x10 cm^2 electron beams of energies 6, 9, 12, 15, 18 and 22 MeV of the linac CL2300C/D (SSD=100 cm). The Monte Carlo simulations (◊) for PDDs (top) are in good agreement with the diode measurements (continuous line), as shown by the corresponding percent difference, (D$_{MC}$-D$_{diode}$)x100 (bottom).
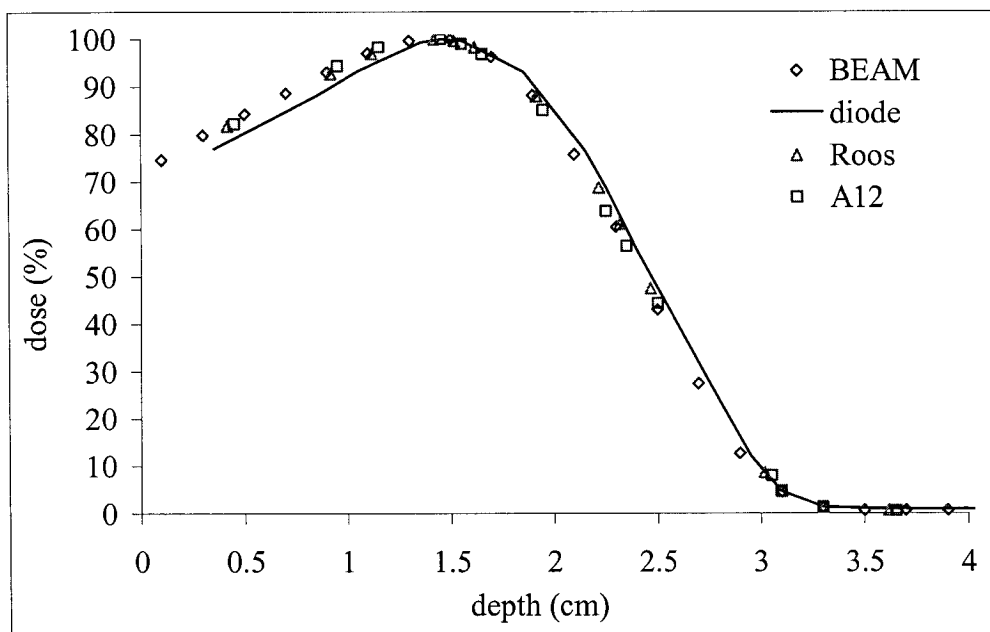
Figure 4.2: Comparison of the PDD for a 6 MeV electron beam with a field size of 10x10 cm² measured by a Roos chamber (△), an Exradin A12 chamber (□) and a p-Si diode (continuous line). The BEAM simulations (◊) are in excellent agreement with the measurements performed with both ionization chambers.

For small electron fields, where the lateral electronic equilibrium is disrupted, the MC model adequately predicts the narrowing of the build-up region. The agreement between MC simulations and diode measurements remains excellent, within experimental and statistical uncertainties, as depicted in Figures 4.3 and 4.4. A similar agreement was obtained with all fields and energies tested. A large recycling rate is at the origin of the noise in the BEAM data in Figure 4.4.
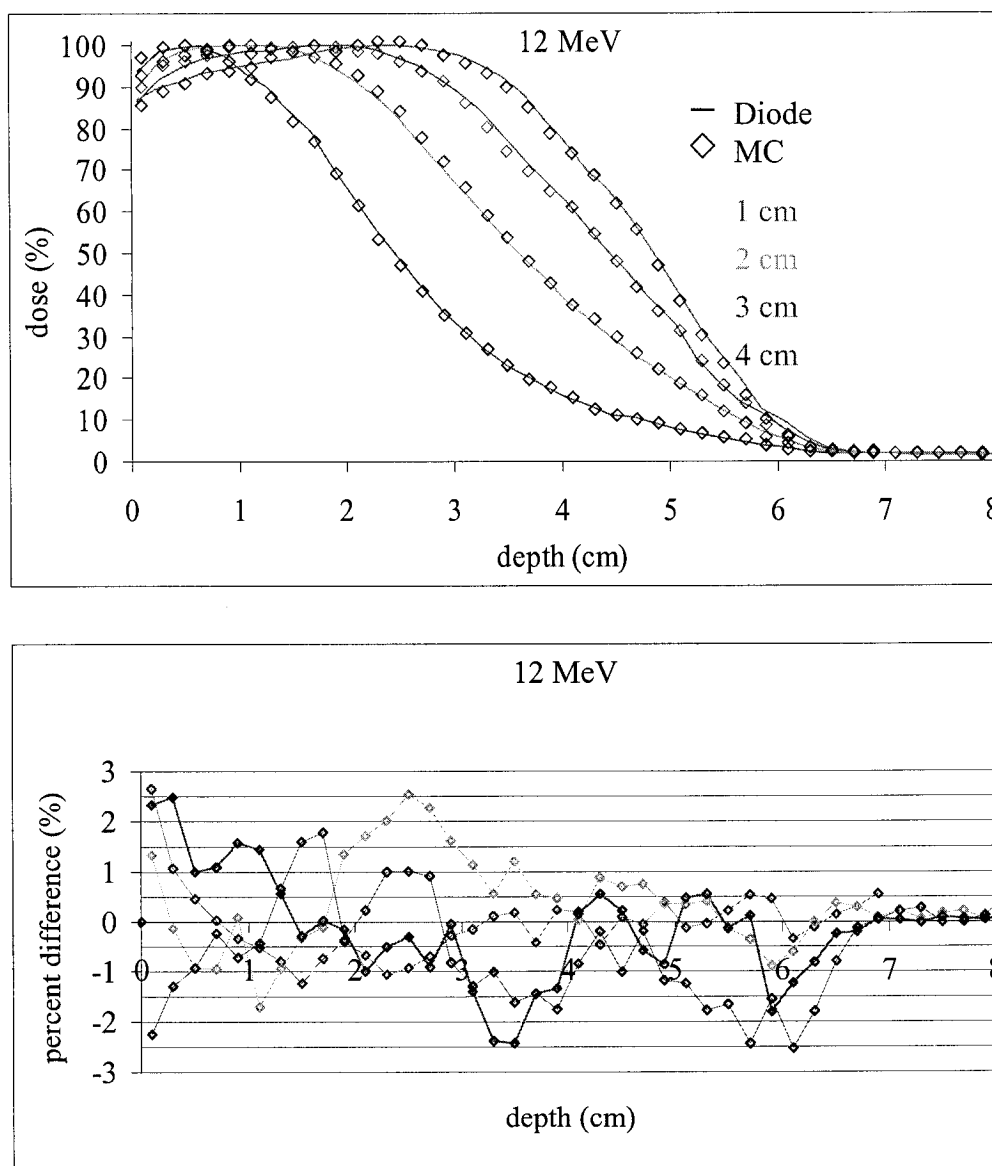
Figure 4.3: Central-axis percentage depth dose curve (top) for a 12 MeV electron beam for a circular field of 1, 2, 3 and 4 cm diameter, as simulated by BEAM ($\Diamond$) and measured by the diode (continuous line) and corresponding percent difference between simulations and measurements, $(D_{MC}-D_{diode})x100$ (bottom).
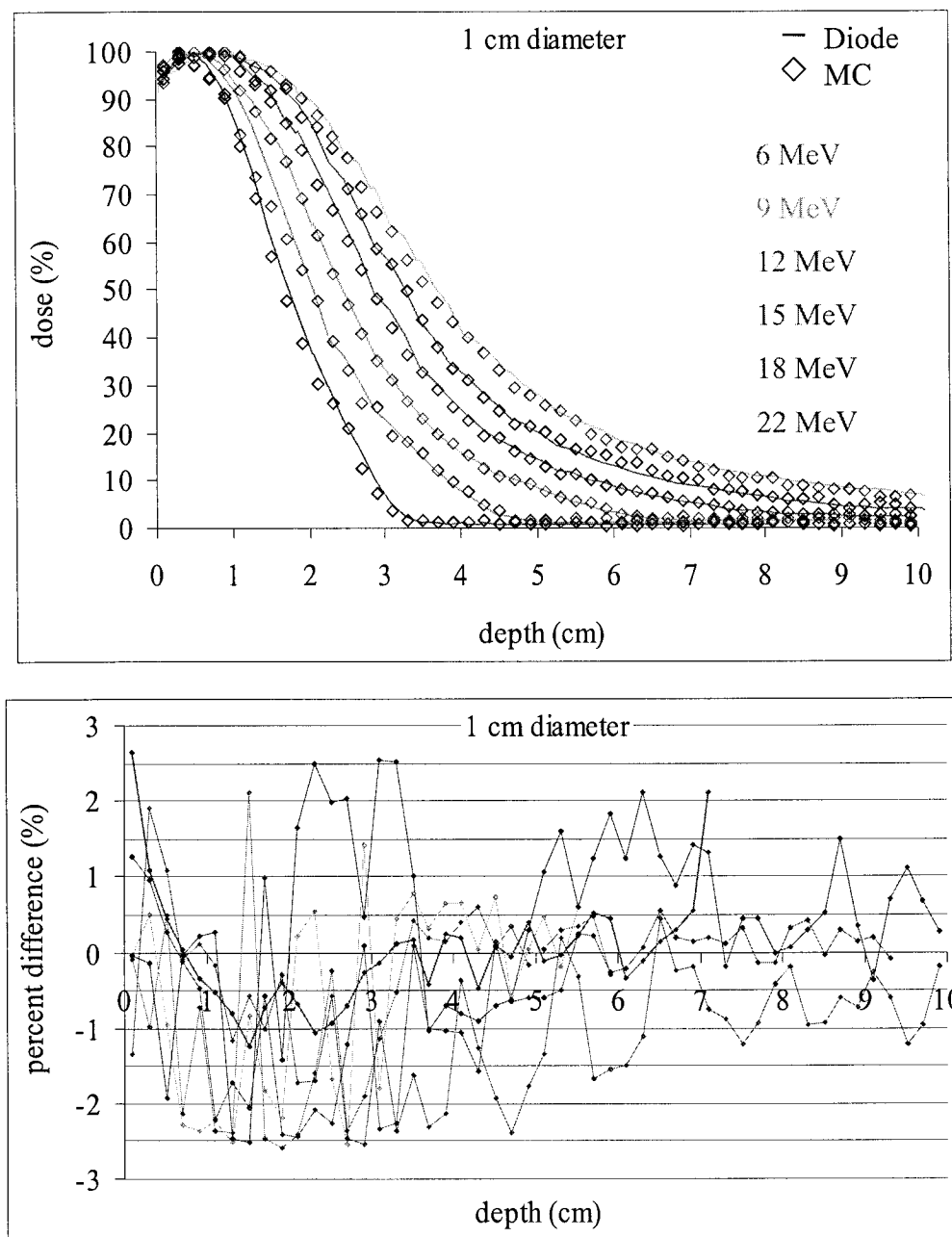
Figure 4.4: Central-axis percentage depth dose curve for circular fields of diameter 1 cm (top) for energies 6, 9, 12, 15, 18 and 22 MeV, as simulated by BEAM (◊) and measured by the diode (continuous line). The percent difference between simulations and measurements, (D_{MC}-D_{diode})x100, is depicted in the bottom graph.

4.1.2 Profiles

The comparison of simulated and measured profiles at the depth of maximum dose and at R_{50} for a 10x10 cm^2 field at all energies leads to the same degree of

agreement as was achieved for the central-axis depth dose, as appears in Figure 4.5. However, the model underestimates the dose by about 4% at the edge of the beam in the region of 95% dose. This difference appears for energies equal to or higher than 15 MeV. It might be attributed to the modelling of the primary beam as a monoenergetic circular beam of 0.5 mm radius. But, tests with a Gaussian beam of Full-Width Half Maximum of 1 mm did not improve the shape of the profiles. The divergence of the beam might need to be increased further. Although this discrepancy is not critical to our project which is mostly concerned with the dose on the central axis, the prediction of the dose at the beginning of the penumbra should be improved in the future.
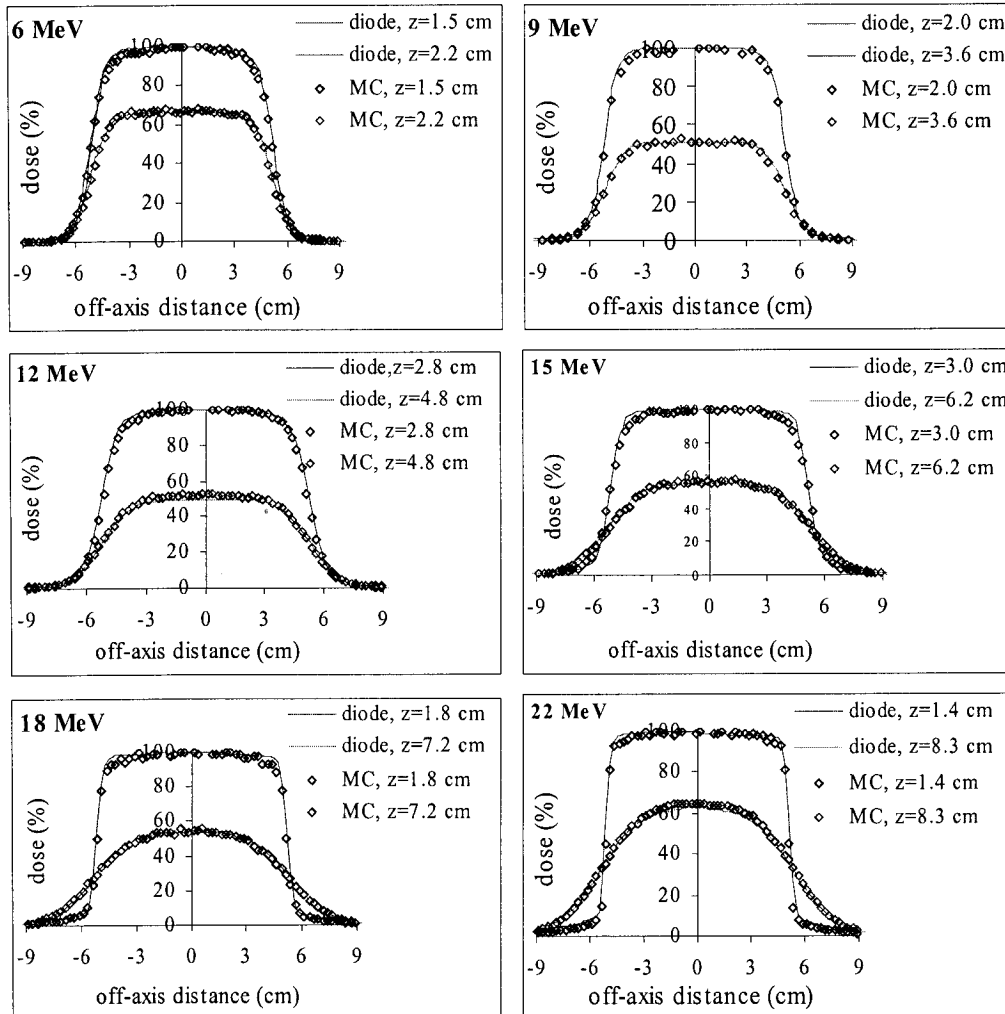
Figure 4.5: Profiles at z_{max} and R_{50} for 10x10 cm² for 6, 9, 12, 15, 18 and 22 MeV electron beams, as simulated by BEAM ($\Diamond$) and measured by the diode (continuous line).

The profiles obtained by MC simulations for various fields with a 12 MeV electron beam in Figure 4.6 follow the same trend as the profiles for 10x10 cm^2 at all energies. The agreement between the MC simulations and the measurements is excellent, except at the dose fall-off in the penumbra for broad beams (larger than 6x6 cm^2) where the model underestimates the dose by 2 to 5%.
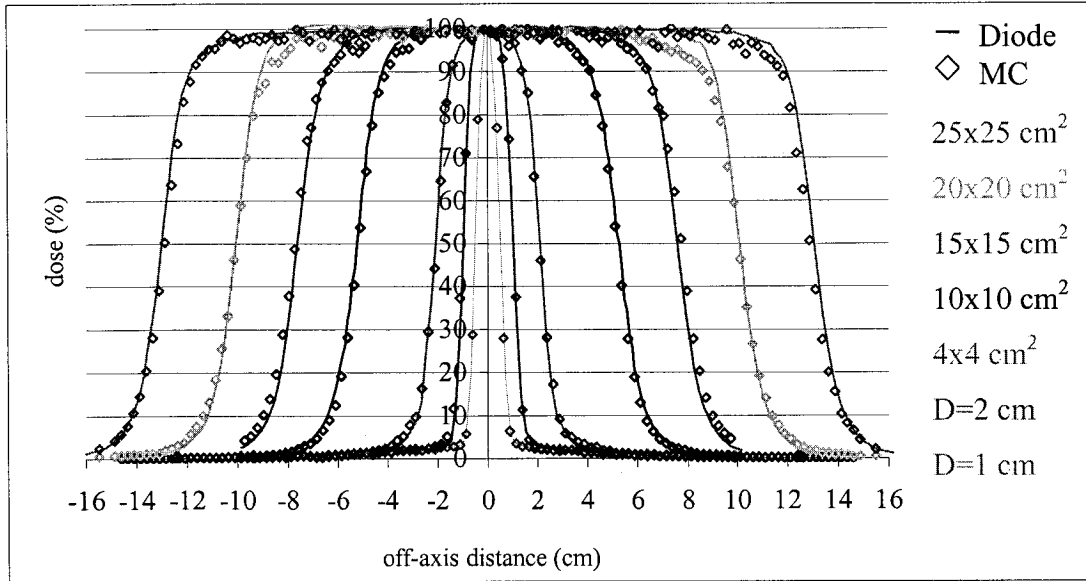
Figure 4.6: Profiles at z_{max} for field sizes of diameter 1 cm, diameter 2 cm, 4x4 cm^2, 10x10 cm^2, 15x15 cm^2, 20x20 cm^2 and 25x25 cm^2 for a 12 MeV electron beam, as simulated by BEAM ($\Diamond$) and measured by the diode (continuous line).

4.1.3 Cutout factors and depth of maximum dose

After the model has been validated for determination of the spatial variation of the relative dose, its ability to predict relative dose variation with changing field sizes and electron energies is evaluated. The values obtained by BEAM simulations and measurements for the depth of maximum dose z_{max} and the cutout factors COF can be compared in Tables 4.1 and 4.2 respectively. The simulated and measured cutout factors coincide within 2.5% and the depths of maximum dose match within 3 mm. z_{max} is difficult to establish acceptable accuracy for high energies and broad beams due to the width of the plateau of maximum dose. To be mentioned as well is the choice of the dimensions of the simulation scoring region that should match the size of the detector, especially for narrow beams. When the radius of the scoring region is too large compared

to that of the diode, the volume averaging effect leads to underpredicted cutout factors compared to measurements.

In this section, the model built using the EGSnrc/BEAM MC code has been validated against diode measurements. The agreement between simulated and measured values is within experimental uncertainty (2.5%-3 mm) for relative depth dose curves and dose profiles as well as for cutout factors. Phase space data collected with this model is therefore considered reliable to be used as input in the CUTOUT and XVMC codes.

4.2 Validation of the CUTOUT code

The EGSnrc CUTOUT user code has been written to transport particles through cutouts of arbitrary shapes and yield the corresponding depth dose curve, cutout factor (COF), z_{max} and phase space below the cutout.

4.2.1 Cutout factors and depths of maximum dose

Tables 4.1 and 4.2 summarize the results for z_{max} and COF, obtained by CUTOUT simulations, by BEAM simulations and by diode measurements for various field sizes and all energies. Figure 4.7 depicts the recurrence of the percent differences in the COF for the results obtained. The agreement between BEAM simulations and measurements was discussed previously in section 4.1.3. The COF simulated by CUTOUT and those measured with the diode agree within 2.5% for fields larger than 2 cm. For narrower beams, the CUTOUT code underestimates the cutout factors by up to 13%. The discrepancy itself might be attributed to a volume averaging effect on the scoring region. The minimum 2 mm thickness allowed for the scoring region might have been too large, allowing too many side-scattered electrons to reach the scoring region. In order to understand this discrepancy better, it would be useful to use other detectors such as the Markus chamber and GafChromic film to measure the COF of small fields. Finally, the CUTOUT code also overestimates the COF for the 20x20, 20x3 and 25x25 cm^2 fields at energy 6 and 12 MeV. An error in the input phase space for the 20x20 and 25x25 cm^2 applicators for these energies is suspected and will necessitate further investigation. Overall, the simulated and measured z_{max} match within 3 mm. As expected, the difference

in z_{max} is smaller for small fields or broad low energy beams which present a narrower region of maximum dose.
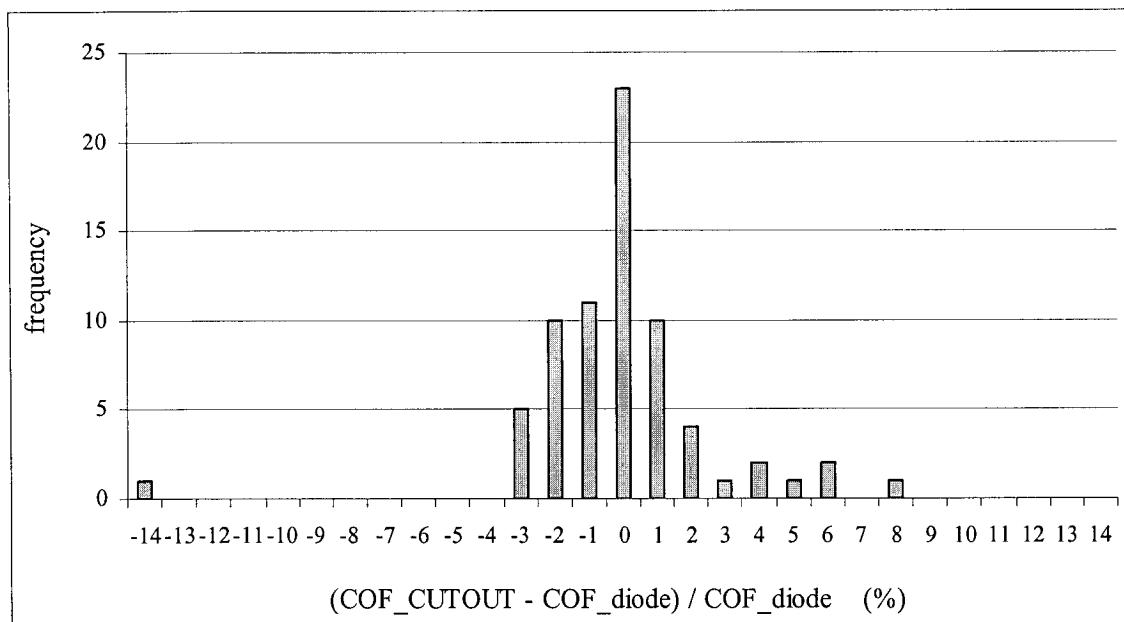
Figure 4.7: Frequency of the percent difference values obtained in the comparison of the simulated and measured cutout factors (Table 4.2).

cutout (cm)	CUTOUT code z_max (cm)						BEAM code diff (cm)=zmax_CUTOUT-zmax_BEAM						Measurement diff (cm)=zmax_CUTOUT-zmax_diode					
	6 MeV	9 MeV	12 MeV	15 MeV	18 MeV	22 MeV	6 MeV	9 MeV	12 MeV	15 MeV	18 MeV	22 MeV	6 MeV	9 MeV	12 MeV	15 MeV	18 MeV	22 MeV
25x25	1.3	2.2	2.9	3.1	2.5	2.3	0.2	0.2	0.0	-0.4	0.4	0.2	-0.2	-0.2	0.0	0.0	0.2	0.0
20x20	1.5	2.3	3.1	3.2	2.5	2.5	0.2	0.0	0.2	0.4	0.0	0.0	0.0	0.0	0.0	0.1	0.2	0.2
15x15	1.5	2.3	3.1	3.3	3.1	2.5	0.2	0.2	0.2	0.0	0.0	0.0	0.0	0.0	0.0	0.2	0.0	-0.1
10x10	1.5	2.3	2.9	3.1	2.6	2.7	0.2	0.2	0.0	0.0	0.1	0.3	0.0	-0.1	-0.2	0.0	0.2	-0.1
D6	1.5	2.3	2.9	3.1	2.3	2.2	0.0	0.2	-0.2	0.2	-0.2	-0.1	-0.1	0.2	0.0	0.0	0.3	0.3
4x4	1.3	1.9	2.5	2.3	1.9	1.3	-0.1	-0.2	0.0	0.0	-0.2	0.2	-0.3	-0.3	0.0	-0.1	0.2	0.2
D4	1.5	1.9	2.1	1.9	1.9	1.7	0.2	0.0	0.0	-0.2	0.0	0.0	0.1	-0.3	0.3	0.2	0.0	0.1
D3	1.3	1.7	1.9	1.7	1.7	1.9	0.2	0.0	0.2	0.0	-0.2	0.2	0.2	-0.1	-0.1	-0.2	-0.1	0.2
D2	0.9	1.1	1.3	1.7	1.3	1.2	0.0	0.2	0.0	0.2	-0.2	0.2	0.0	0.2	-0.1	0.3	0.0	0.2
D1	0.3	0.3	0.3	0.5	0.7	1.0	0.2	0.2	0.2	0.2	0.2	0.0	-0.1	-0.2	-0.1	-0.2	0.0	0.4
20x3	1.3	2.1	2.1	2.3	2.0	2.0		0.0	0.2	0.2	0.2	0.2	-0.2	0.0	0.0	0.0	-0.3	0.2
10x2	1.3	1.5	1.7	1.9	1.5	1.7	0.2	0.2	0.3	0.0	-0.1	0.2	-0.1	-0.3	-0.1	-0.1	-0.3	0.1
	1.3	1.9	1.7	1.7	2.2	2.0	-	-	-	-	-	-	-0.2	0.1	-0.1	0.0	0.2	0.3
	1.3	1.7	2.2	2	1.8	1.7	-	-	-	-	-	-	-0.1	-0.2	0.1	0.1	0.1	0.2

Table 4.1: Depths of maximum dose for a selection of energies and fields. The values obtained by the CUTOUT code are in the left third of the table, whereas the differences between the depths of maximum dose obtained by CUTOUT and the values obtained by BEAM are displayed in the central part of the table. In the right third of the table, the differences between the depths of maximum dose obtained by CUTOUT and the values measured with the diode are presented.

cutout (cm)	CUTOUT code COF 6 MeV	9 MeV	12 MeV	15 MeV	18 MeV	22 MeV	BEAM code % diff=(COF_cutout - COF_BEAM) / COF_BEAM 6 MeV	9 MeV	12 MeV	15 MeV	18 MeV	22 MeV	Measurement % diff=(COF_cutout - COF_diode) / COF_diode 6 MeV	9 MeV	12 MeV	15 MeV	18 MeV	22 MeV
25x25	1.085 (0.2)	0.970 (0.3)	1.023 (0.2)	0.953 (0.3)	0.935 (0.3)	0.905 (0.3)	1.2 (0.5)	0.3 (0.2)	1.1 (0.2)	1.5 (0.2)	1.6 (0.2)	2.4 (0.2)	8.4	0.9	4.1	0.6	-0.4	-2.4
20x20	1.068 (0.2)	0.999 (0.3)	1.029 (0.3)	0.997 (0.2)	0.974 (0.3)	0.946 (0.3)	0.5 (0.2)	-0.1 (0.1)	0.5 (0.2)	-0.1 (0.2)	0.8 (0.2)	0.8 (0.2)	5.9	1.5	4.9	2.0	0.4	-1.4
15x15	1.010 (0.2)	0.996 (0.2)	1.009 (0.2)	1.003 (0.2)	0.993 (0.2)	0.974 (0.2)	-0.6 (0.3)	-1.3 (0.1)	-0.9 (0.1)	-1.0 (0.1)	-0.3 (0.1)	0.0 (0.2)	1.1	0.1	1.5	1.2	0.0	-0.2
D6	1.007 (0.5)	0.988 (0.6)	1.001 (0.4)	1.009 (0.5)	1.020 (0.5)	1.025 (0.6)	-1.3 (0.8)	-2.1 (0.6)	0.0 (0.7)	0.6 (1.1)	0.8 (1.1)	1.8 (1.0)	2.2	0.4	0.5	1.2	0.0	1.4
4x4	0.931 (0.4)	0.933 (0.5)	0.916 (0.5)	0.945 (0.5)	0.994 (0.7)	1.012 (0.5)	-5.4 (0.5)	-1.6 (0.5)	-0.6 (1.1)	-0.7 (0.5)	1.2 (1.2)	-0.5 (1.1)	-0.1	-0.5	-2.5	-2.5	0.0	-1.6
D4	0.918 (0.4)	0.925 (0.5)	0.908 (0.5)	0.949 (0.6)	0.999 (0.6)	1.012 (0.5)	0.6 (1.0)	-2.1 (0.8)	-1.2 (0.8)	1.0 (0.9)	2.5 (0.6)	1.3 (0.6)	-0.8	-0.7	-2.3	-0.7	0.0	1.7
D3	0.863 (0.5)	0.880 (0.5)	0.890 (0.6)	0.932 (0.6)	0.999 (0.6)	0.998 (0.6)	-0.9 (0.5)	-0.5 (0.7)	-0.4 (1.2)	-1.2 (0.3)	1.7 (1.2)	1.7 (1.1)	0.2	0.1	-1.4	-1.1	0.0	1.7
D2	0.731 (0.8)	0.795 (0.9)	0.834 (0.9)	0.889 (1.1)	0.960 (1.0)	0.972 (1.3)	0.2 (0.9)	-0.8 (0.4)	-2.5 (1.0)	-0.1 (1.2)	0.1 (1.0)	1.9 (1.0)	-6.3	1.4	-3.4	-3.7	0.0	-0.3
D1	0.401 (1.1)	0.559 (1.0)	0.706 (1.1)	0.802 (1.0)	0.869 (1.1)	0.902 (1.2)	-1.1 (1.3)	-1.7 (0.5)	-2.5 (0.9)	0.6 (0.8)	2.5 (0.9)	1.4 (0.6)	-13.7	-9.8	-7.5	-3.4	-1.9	-1.8
20x3	1.007 (1.5)	0.903 (0.9)	0.947 (1.6)	0.925 (1.3)	0.975 (2.2)	0.932 (2.0)		-0.7 (0.8)	1.1 (0.8)	0.9 (0.8)	2.0 ()	3.0 ()	5.7	-0.1	4.3	-1.0	3.4	-1.9
10x2	0.865 (0.8)	0.849 (0.8)	0.909 (0.8)	0.959 (0.9)	0.971 (0.9)	0.983 (0.8)	-1.7 (1.1)	-2.0 (0.8)	-1.8 (1.0)	1.2 (0.7)	-2.3 (0.8)	0.3 (0.6)	-0.8	-2.4	0.0	1.5	0.0	0.5
(cutout shape)	0.890 (1.4)	0.881 (0.9)	0.916 (0.8)	0.969 (1.1)	0.977 (1.1)	0.983 (1.0)	-	-	-	-	-	-	-3.2	-3.1	-1.7	0.5	-0.9	-1.3
(cutout shape)	0.883 (1.0)	0.875 (1.1)	0.903 (1.2)	0.928 (1.4)	0.973 (1.5)	0.964 (1.5)	-	-	-	-	-	-	-3.9	-4.2	-3.5	-4.0	-1.5	-2.5

Table 4.2: Cutout factors for various energies and fields obtained by the CUTOUT code. The numbers in brackets are the 1σ statistical uncertainty on the CUTOUT and BEAM simulations. In the central part of the table, the percent difference between the cutout factors obtained by CUTOUT and the values obtained by BEAM are presented. In the right third of the table, the percent difference between the cutout factors obtained by CUTOUT and the values measured with the diode are presented.

4.2.2 Depth dose curves

The percentage depth dose curves simulated by the CUTOUT code are in excellent agreement with the measurements. The cases displayed in Figures 4.8, 4.9, 4.10 and 4.11 were chosen because they represented an especially stringent test for the algorithm as a combination of low energy and small or irregular beams. A similar agreement was observed in all the tested cases. There is a trade-off between resolution and maximum distal extent of the PDD because of the limit presently set on the number of scoring regions in the phantom of the CUTOUT code. The CUTOUT code initially aims at the determination of dose in the build-up region, which never extends beyond the first five centimetres. Nevertheless, the CUTOUT code could be modified in the future to allow for the prediction of doses even at larger depths. To achieve this goal, the number of scoring regions in the phantom of the CUTOUT code could be made simply larger or user-specified akin to the BEAM CHAMBER component module.
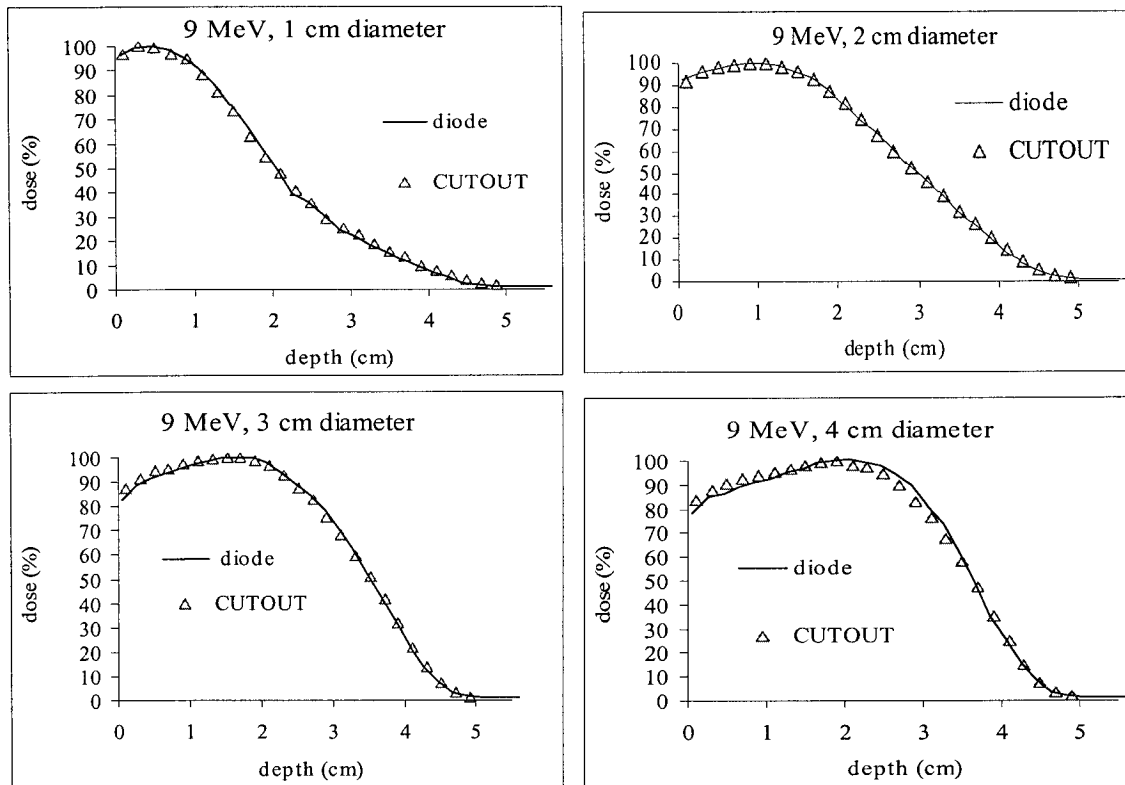
Figure 4.8: Central-axis percentage depth dose curves for a 9 MeV electron beam with circular fields of diameter 1, 2, 3 and 4 cm, as simulated by CUTOUT (Δ) and measured by the diode (continuous line).

Figure 4.9: Central-axis percentage depth dose curves with a circular field of diameter 1 cm for all energies, as simulated by CUTOUT (Δ) and measured by the diode (continuous line).

Figure 4.10: Central-axis percentage depth dose curves for 6, 9, 12, 15, 18 and 22 MeV with an irregular field (photo above), as simulated by CUTOUT (Δ) and measured by the diode (continuous line).

Figure 4.11: Off-axis percentage depth dose curves for 6, 9, 12, 15, 18 and 22 MeV with an irregular ex-centered elongated field (photo above), as simulated by CUTOUT (△) and measured by the diode (continuous line).

4.2.3 Validation of phase space scoring

The phase spaces produced by the CUTOUT code just below the cutout were collected and used as input to homogeneous water phantoms in DOSXYZnrc in order to obtain PDDs and profiles. The PDDs and profiles are depicted in Figure 4.12 for a selection of energies and field sizes, chosen as stringent for the CUTOUT code. They are in excellent agreement with the corresponding diode measurements for the selected tested fields. However, more such tests as well as the testing of the cutout factors predicted by using these output phase spaces remain to be done for the validation to be complete.

As a conclusion, the CUTOUT code has been validated for calculation of depth doses and cutout factors. It outputs values accurate within experimental uncertainty (2.5%-3 mm) for fields larger than 2 cm. The reason for the discrepancies obtained with narrower fields remains unknown, but some explanations requiring further exploration have been offered. The phase spaces used as input to model fields obtained with the 20x20 cm^2 and 25x25 cm^2 applicators for 6 MeV and 12 MeV also need to be re-acquired. The phase spaces collected by CUTOUT have to be validated. Some tests run on a few stringent cases provide good results for relative depth dose curve; however, the corresponding cutout factors remain to be tested.
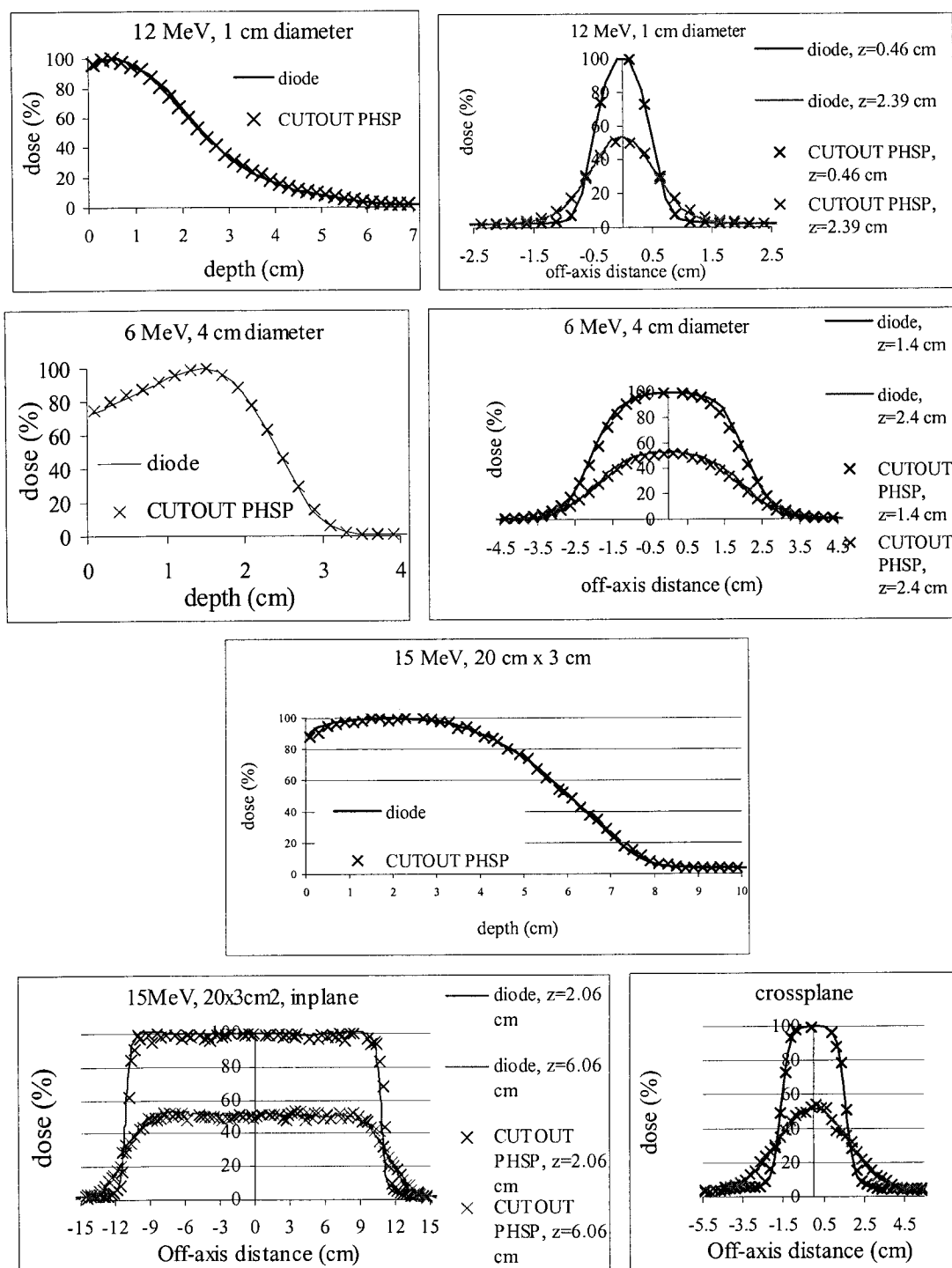
Figure 4.12: Percentage depth dose and profiles at z_{max} and R_{50} for a selection of energies and field sizes, as simulated by BEAM (◊), by CUTOUT (Δ), by DOSXYZ from a CUTOUT-generated phase space (×) and as measured by the diode (continuous line).

4.3 Automated Monte Carlo system for calculation of cutout factors

A graphical user interface (GUI) was built in order to automate the calculation of the COF, z_{max}, PDD and phase space with the CUTOUT code. It transfers to the CUTOUT code the data entered by the user, triggers execution on a remote computer or computer cluster, and extracts the relevant output. The GUI written in REALbasic can be compiled for operating systems (Apple, Windows, Unix) allowing to run the simulations remotely from any computer in the clinic.

4.3.1 Organization of the system and automation

The CUTOUT code requires input of geometry data and pre-calculated material cross-section, source and reference dose data. The material cross-sections are read from a PEGS4 file containing all relevant materials. The source data consisting of the phase space files for each combination of energy and electron applicator was collected for the linac CL2300 C/D. Maximum doses in a homogeneous water phantom calculated by the system for the reference field for all energies of a given linac are available in text files. Presently, all these pre-generated files required for the execution of CUTOUT are grouped on a devoted station.

Then, the user simply needs to input basic geometric data and beam parameters in the GUI as listed in the first column of Figure 4.13. The "Parameter" panel in Figure 4.14 is dedicated to the input of the cutout and phantom parameters. The "EGSnrc Set Up" page in Figure 4.15 available in the password protected "Expert mode", is dedicated to the choice of the Monte Carlo transport parameters.

Parameters of the beam
- **Select Linac**
- **Select energy**
- **Select cone size**

Parameters of the cutout
- **Digitize cutout**
- **Select thickness of cutout**
- **Select material of cutout**

Parameters of the gap
- **Select material inside cutout and "air" gap**
- **Select SSD** (*i.e.* thickness of air gap)

Parameters of the phantom
- *Select material of phantom*
- *Select thickness of scoring region*
- *Select radius of scoring region*

Monte Carlo transport parameters
- *Select ECUT*
- *Select PCUT*
- *Select backscatter type*
- *Select # histories*

Select type of output:
1) phase space
2) dose calculation
3) both

Link to table of Dmax for 10x10cm² for the nominal energy and phantom material selected name.egsoutputfactors

Link to corresponding input phase space CLname_energy(MeV)_side of squareconesize(cm).egsphsp1

A ".egscutoutdata" file is created. Name.egscutoutdata

Data are written in an input file for the cutout code, in the order specified by the numbers Name.egsinp

CALCULATE

PDD, Zmax, COF, % error

Phase space below cutout

Figure 4.13: Flowchart showing the input required from the user (bold input in the left column), the creation of the appropriate files and links and the calculation process of the automated Monte Carlo system for calculation of cutout factors for clinical electron beams. The parameters italicized are set to default parameters unless they are specified in the password-protected "Expert mode".
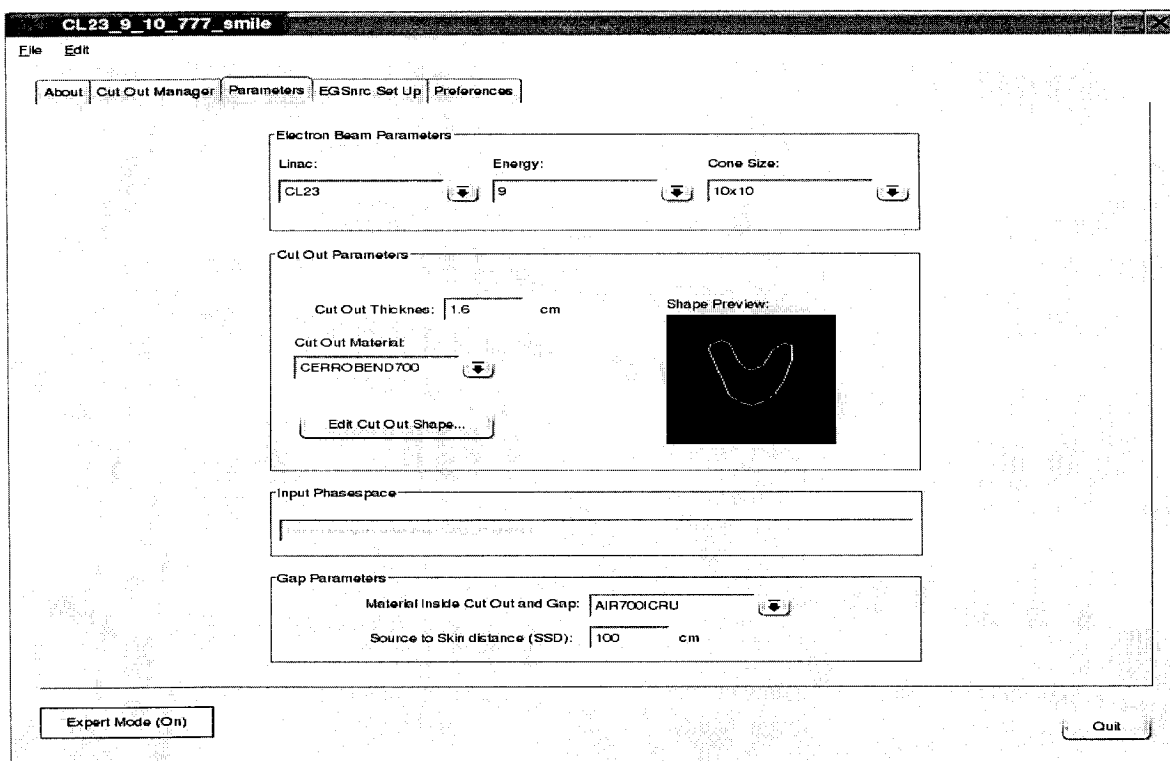
Figure 4.14: Snapshot of the page dedicated to the selection of geometry parameters on the GUI.
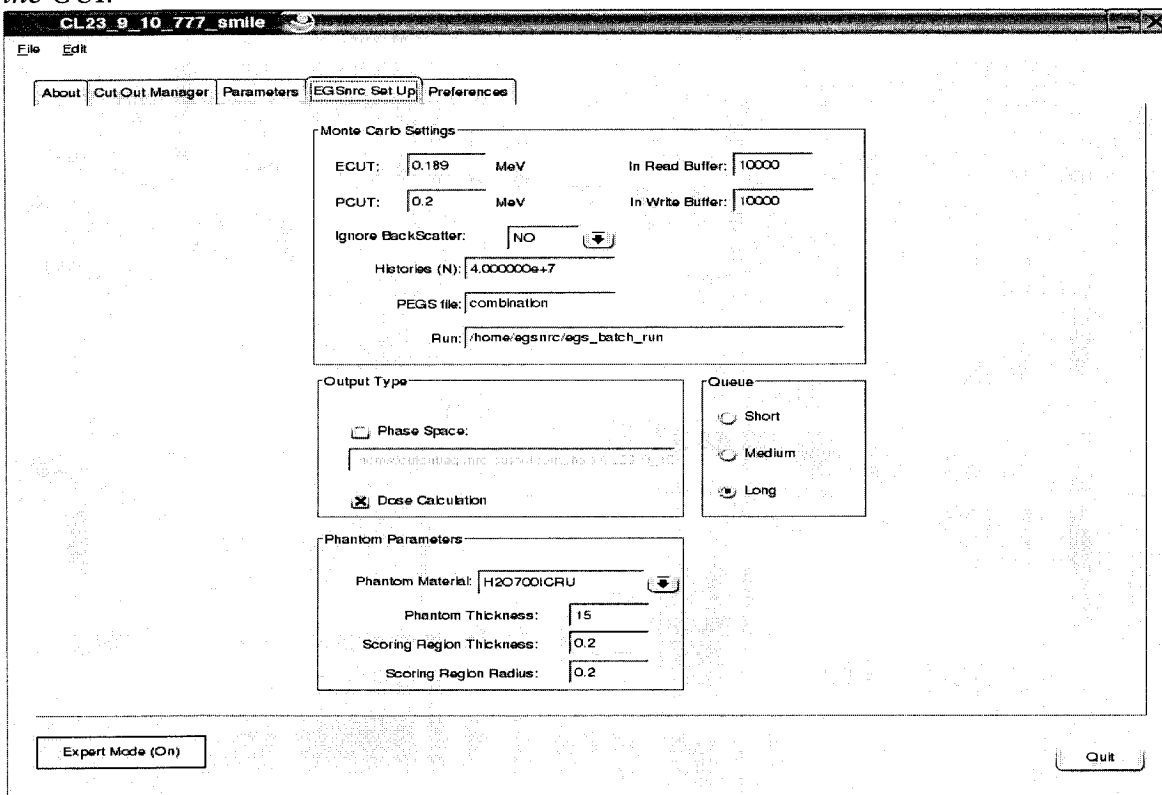
Figure 4.15: Snapshot of the page dedicated to the selection of Monte Carlo transport parameters on the GUI.

As far as the cutout itself is concerned, the data needed are its thickness, its material to choose from a list and its contour. The contour may be digitized *in situ* with the mouse on a beforehand-calibrated screen of any computer, as shown schematically in Figure 4.16.
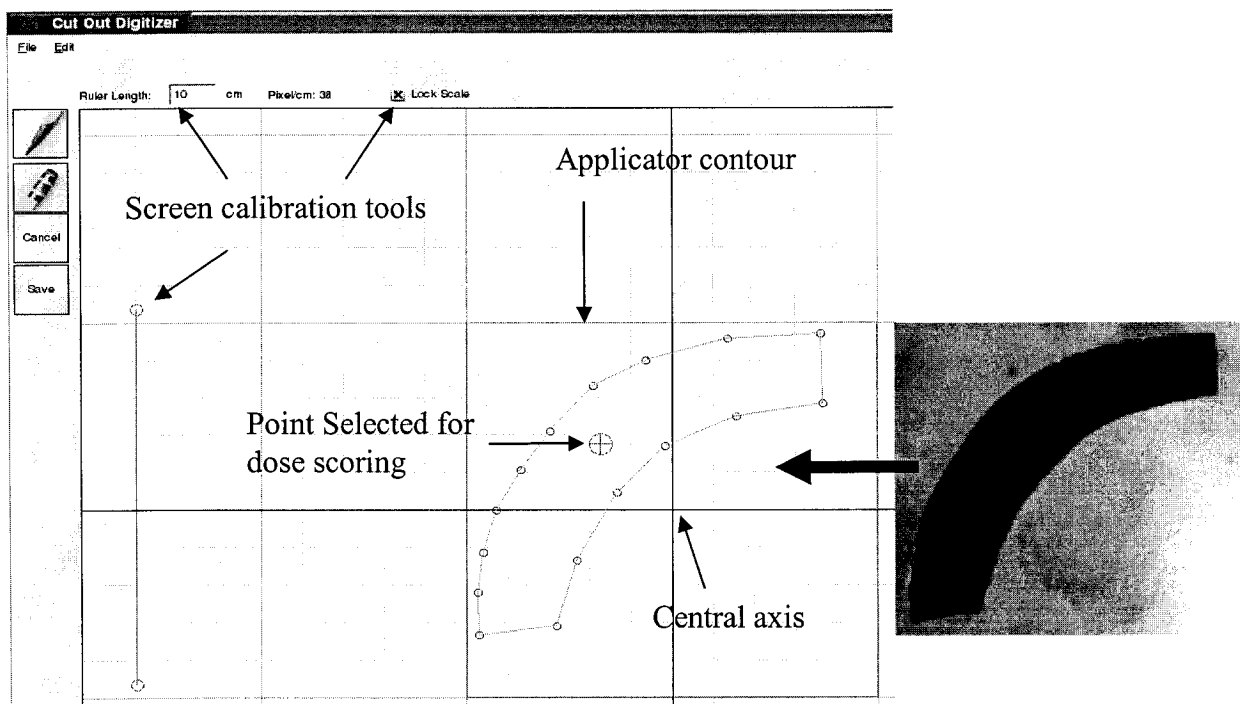
Figure 4.16: Snapshot of the digitization window on the GUI (with photo of the corresponding cutout on the right).

Based on this input information, the GUI writes the files and path required by the execution of the program, as shown in the second column of the flowchart in Figure 4.13 and starts the execution upon user initiative. The GUI monitors the status of the execution and displays the percentage of the execution achieved. For this, it reads the file containing partial depth dose results (with extension "egsbatchdata"). This also allows the display of the COF, z_{max} and PDD in real-time. Thus, the user can abort the execution early when the desired uncertainty is achieved and when the PDD looks smooth.

All cases that have been run are retrievable thanks to a dynamic filing system accessible from the GUI's main page. This main page, a snapshot of which is visible in Figure 4.17, displays all the cases entered in the system, with clinically relevant patient information, a preview of the cutout shape, indications of the treatment machine, energy

and applicator size used (in the name convention), as well as the calculation status for each case. In the results section, the COF and z_{max} for the selected case are displayed. The depth dose curve and details for the MC calculation (in the "egslog" file) can also be shown.
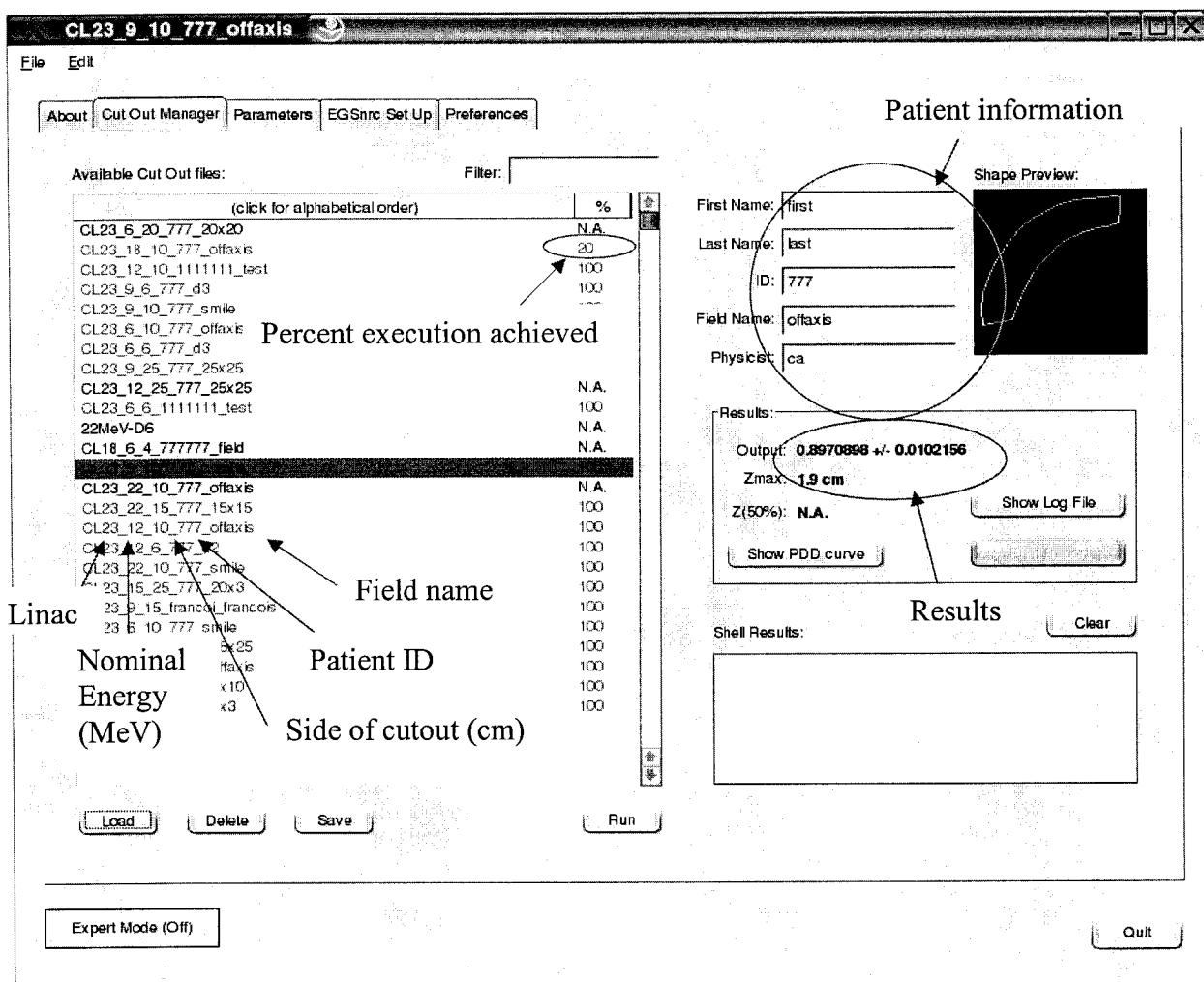
Figure 4.17: Snapshot of the main page of the GUI.

4.3.2 Time considerations

The computation time depends strongly on the number of histories, the size of the scoring region and the Monte Carlo transport parameters. On average, it can be estimated to be 30 min for a 2% statistical uncertainty on the dose values and 10 minutes for the acquisition of a 5 to 10 million particle phase space, on a single computer with a 1.9 GHz processor. This computation speed seems satisfactory to the clinic which currently uses

the automated system in its present state. Nevertheless, this could be improved by introduction of variance reduction techniques.

Presently, all particles are transported until they reach the energy cut-off. However, the photons contribute to the total dose similarly for various fields and have an insignificant effect on the dose ratio. They could therefore be discarded without significant degradation of the accuracy of the results, as previously suggested by Zhang *et al*[1] and Verhaegen *et al*[2]. This would considerably improve the calculation efficiency considering that photon transport is slower and that the input phase spaces for the system contain a majority of photons, as verified in the Table 4.3 showing the percentage of particles represented by photons in the input phase spaces of the system. Secondly, amongst the numerous electrons scattered from the cutout, only the few scattered from the edges of its opening actually reach the central axis or measurement axis. Therefore, one could discard the electrons impinging on the cutout outside of a "skin depth" without significantly altering the central-axis dose, thereby resulting in remarkable time gain. The skin depth would be energy-dependent and reach 2.5 cm maximum for a 20 MeV electron beam. This has been suggested by Zhang *et al*[1]; Verhaegen *et al*[2] proved that the subsequent dose change would be irrelevant. Obviously, the deletion of these scattered electrons is inappropriate when the CUTOUT code is used to collect a phase space instead of simply calculating depth doses and cutout factors. Finally, the simulations could obviously be split in batches and run on a cluster of computers. The computing time would thereby be decreased proportionally to the computing power and number of the machines it would run on.

% photons	6 MeV	9 MeV	12 MeV	15 MeV	18 MeV	22 MeV
6 cm x 6 cm	40.6	46.8	52.9	61.7	67.9	70.9
10 cm x 10 cm	38.6	44.5	49.0	57.3	63.7	66.7
15 cm x 15 cm	33.6	37.7	42.8	50.1	56.4	59.2
20 cm x 20 cm	30.7	35.0	42.7	47.7	52.5	55.3
25 cm x 25 cm	28.0	32.2	35.6	43.1	47.5	50.0

Table 4.3: Percentage of photons contained in the input phase spaces of the cutout factor calculation system.

4.4 Verification of CadPlan and Monte Carlo calculated dose distributions

Most of the electron treatment planning is done today based on measurements and analytical models, no treatment planning system (TPS) having provided dose distributions with a satisfactory accuracy. Only recently, a MC-based TPS has been distributed, clinically implemented and used[3]. In this section, the ability of Monte Carlo XVMC user code to calculate accurate electron beam dose distributions in CT images is evaluated. CadPlan and XVMC 3-dimensional dose calculations are compared to TLD measurements, firstly in a homogeneous Solid Water™ phantom, secondly in phantoms containing lung and bone slabs and finally in the head of an anthropomorphic phantom. Note that in all the following section, the doses displayed are the doses absorbed by the medium expressed in cGy upon irradiation by 100 MU of a 12 MeV electron beam of dimension 10x10 cm² at an SSD of 100 cm, except for the doses calculated by CadPlan which are expressed in terms of dose to water.

4.4.1 Homogeneous solid water phantom

Firstly, the dose measured with TLD-700 in solid water is compared to the dose measured with a diode in water and to the dose simulated by BEAM in water and solid water. Considering the excellent agreement between the curves in Figure 4.18, it is justified to use the model for XVMC simulations and to use TLD-700 for dose measurements.
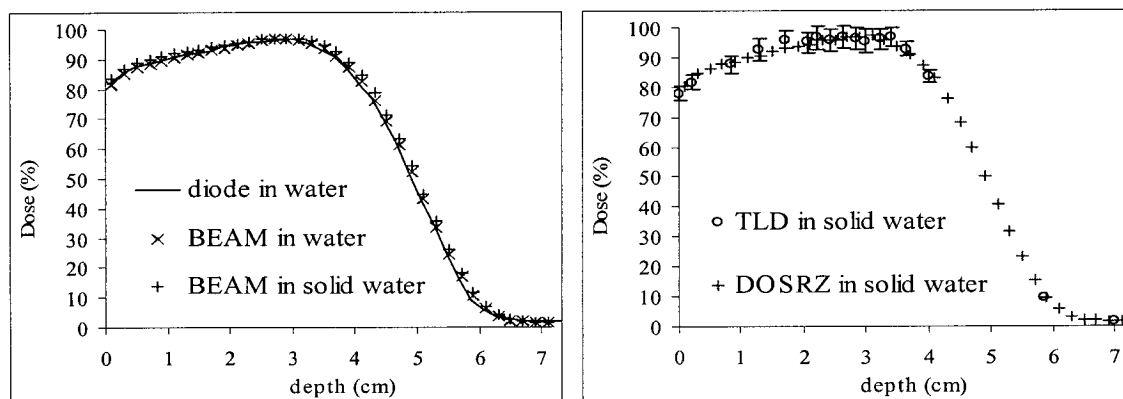
Figure 4.18: Validation of the TLD measurements for the central-axis percentage depth dose curves for a 12 MeV electron beam with a 10x10 cm² field size at an SSD of 100 cm. The BEAM simulations in water (×) are in good agreement with the diode measurements in water (continuous line). The TLD measurements in a homogeneous solid water phantom (o) match the Monte Carlo simulations in a homogeneous water phantom (+).

The next step consists of a comparison of the PDDs simulated by XVMC in the CT image compressed as described in section 3.1.2.d and in the mathematical phantom, with the PDDs predicted by CadPlan on the same CT image and with the TLD measurements in Figure 4.19. Overall, the PDDs simulated by XVMC and CadPlan are in good agreement with the measurements. In such a homogeneous phantom, CadPlan was actually expected to provide an accurate dose distribution. A few discrepancies are nevertheless noticeable. First, CadPlan's dose prediction at the end of the build-up region is inaccurate by 5%. This behaviour was observed by Ding *et al*[4] as well and may stem from a calculation grid size issue. Indeed, the pencil beams traced along central lines overlap at large depths where the beam divergence is more perceptible, leading to severe dose overestimations. However, the actual dose at large depths is small enough to make this effect difficult to notice. On the contrary, the combination of large doses and medium depths occurring at the deeper end of the build-up region enhances this adverse overlapping effect, then possibly explaining the 5% dose overestimation by CadPlan. CadPlan's PDD is also shifted by 1 mm downstream, which is considered acceptable in the criteria set by ICRU 42[5]. Moreover, as formerly observed by Ding *et al*[4] and Hodefi[6], CadPlan underestimates the surface dose by 13%, since the dose values in the first line of the dose matrix are systematically set to zero. Then, the PDDs obtained by XVMC run on mathematical homogeneous solid water phantoms and compressed CT image of the same phantom match well with the TLD measurements. As expected, the depth dose curve simulated in the mathematical phantom is closer to the measurements than that simulated in the CT image of the phantom, especially at the surface. However, this study aimed at a comparison between XVMC simulations in CT images and measurements. Considering that the agreement between XVMC simulations in mathematical phantoms and TLD measurements has already been established[7], our goal was to address some issues related to CT artefacts and the degree of reliability that can be conferred to XVMC simulations in CT images of phantoms. Finally, as mentioned in section 3.1.2.d, at shallow depths, Monte Carlo calculations are sensitive to medium averaging occurring at interfaces between phantom (or patient) and overlying air or inter-slab air gaps as part of the CT image. But, the surface dose can be extrapolated from the trend leading to a surface dose accurate within 2%.

The agreement between the profiles calculated by XVMC and CadPlan shown in Figure 4.20 is excellent as far as the dose profile shape and width are concerned. The discrepancies in the relative central-axis dose are in agreement with those previously discussed for the PDDs of Figure 4.19. They are worsened by the extraction of the dose values at slightly different depths due to non-identical voxel sizes, which is critical for the depth of R_{50} lying in a region of steep dose gradient.
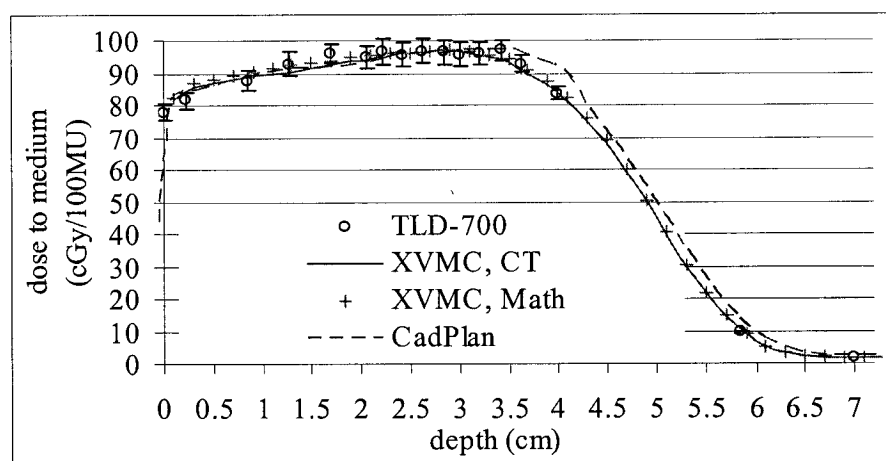
Figure 4.19: Validation of the central-axis doses calculated by XVMC and CadPlan for a 12 MeV electron beam of size 10x10 cm^2 on a solid water phantom. The CadPlan calculations in the CT image of the phantom (dashed purple line) and the XVMC simulations in the compressed CT image of the phantom (continuous blue line) and in a mathematical phantom (+) are compared to the measurements with TLD-700 (o).

Figure 4.20: Profiles at z_{max} and R_{50} for a 12 MeV electron beam of size 10x10 cm^2 on a solid water phantom. The XVMC simulations in a compressed CT image (continuous line) and in a mathematical phantom (+) are compared to the dose calculations performed by CadPlan (dashed line).

Finally, Figure 4.21 shows an agreement within 1.5 mm between the isodose distributions calculated by XVMC and by CadPlan in the central axial slice of the CT images of the phantom for isodoses below 80 cGy, as was previously reported by Hodefi[6]. High-dose isolines carry a significant uncertainty as a consequence of the small number of points of high dose which they connect. They are also very noisy, although the statistical uncertainty on these simulations is less than 1% at all dose levels. The noise could not be reduced by an increase in the number of history or in the voxel size or by running the simulations in a mathematical phantom, as presented in Figure 4.22. It might therefore be attributed to the use of a phase space as a source, as was suggested by the smoother isodoses obtained when running simulations with monoenergetic electron beams in a mathematical phantom. Moreover, the difference between the 85 and 90 cGy isodoses corresponds to the discrepancy in the build-up region of Figure 4.19, where CadPlan produces higher doses at shallower depths than XVMC and initiates the dose fall-off 5 mm before XVMC. Isodoses calculated by XVMC are constricted by more than 2 cm with respect to those calculated by CadPlan. A plot of isodoses calculated by XVMC in the CT image of the phantom and in the mathematical phantom in Figure 4.22 exhibits the same constriction. Therefore, this discrepancy between XVMC and CadPlan is not related to a miscalculation of XVMC in the CT phantom but to an inherent difference in the dose calculation by CadPlan compared to XVMC.

Now that the validity of XVMC and CadPlan dose distributions has been verified in homogeneous phantoms, the dose calculations are studied in heterogeneous phantoms.
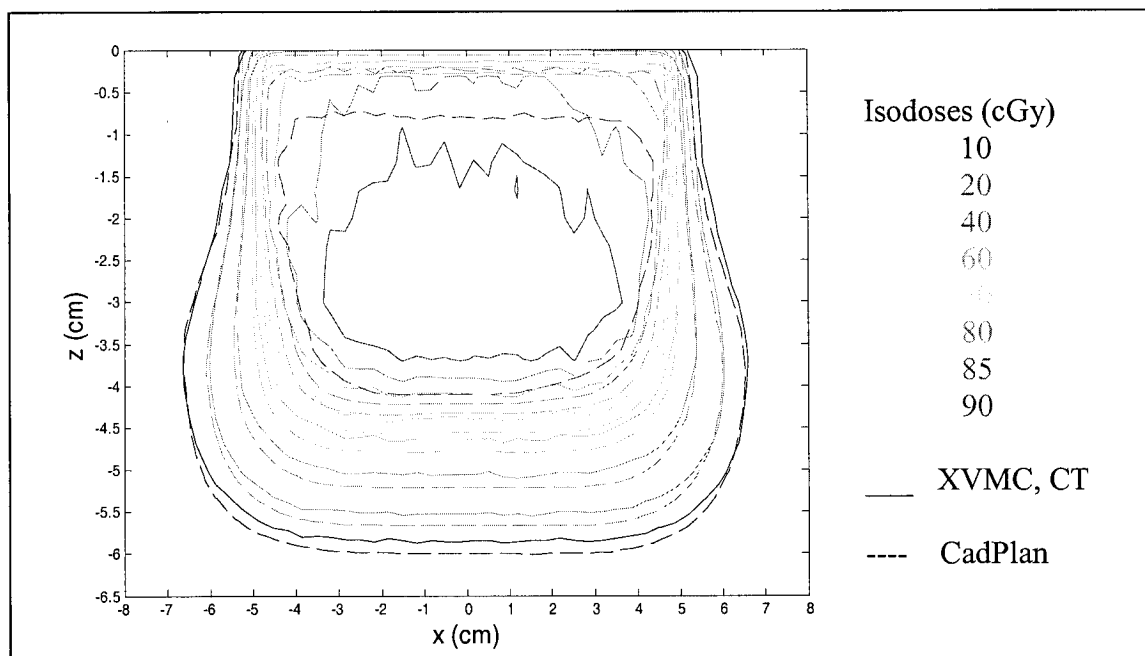
Figure 4.21: Axial distribution of dose to solid water (cGy) for a 12 MeV electron beam with a 10x10 cm² field impinging on a solid water phantom. The XVMC simulations in a compressed CT image (continuous line) are compared to those performed by CadPlan (dashed line).
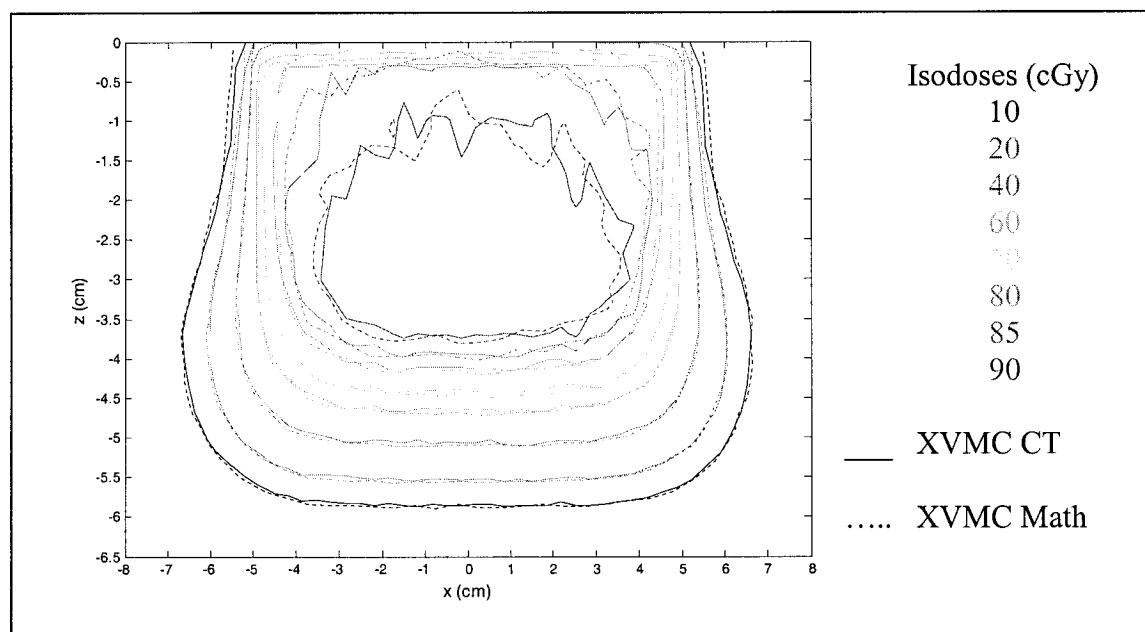
Figure 4.22: Axial distribution of dose to solid water (cGy) for a 12 MeV electron beam with a 10x10 cm² field impinging on a solid water phantom. The XVMC simulations in a compressed CT image (continuous line) are compared to those in a mathematical phantom (dotted line).

4.4.2 Heterogeneous lung phantom

This section examines the dose distribution in a heterogeneous phantom with a 3 cm-thick slab of lung at 1 cm depth in a solid water phantom.

Figure 4.23 compares the central-axis doses calculated by CadPlan in a CT image of the phantom and the central-axis doses calculated by XVMC in a mathematical phantom and in the modified image of a CT phantom to the measurements performed with TLD-700. The agreement between the PDDs is excellent. As expected, CadPlan handles properly the dose calculation in this 1-dimensional heterogeneity, although it is less sensitive than XVMC to abrupt dose change at the interface lung-solid water. CadPlan does not predict the abrupt increase in measured dose, because its algorithm neglects backscatter and inappropriately assumes similar angular distributions on both sides of the interface. This concurs with the findings of Ding *et al*[4]. The dose calculated by CadPlan in the lung slab is reported as dose to water, which may explain part of the 4% underestimation with respect to the other data, as estimated in section 3.3.3.c. Here again, the surface dose is underestimated by CadPlan by 12%. XVMC on the other hand predicts very accurately the depth dose curve, including the interface effects and the dose increase in lung. In the CT phantom, the interface effects predicted by XVMC are less pronounced, as a logical consequence of the density averaging in the voxel overlapping the interface. For the same reason, the dose calculated by XVMC in the CT phantom at 0.1 cm is 7% too low whereas the dose at the next depth (0.5 cm) is within 0.5% of the measured value.

The profiles calculated by CadPlan and XVMC on the same CT image of the phantom and by XVMC in a mathematical phantom have similar shapes and widths as in Figure 4.24. The discrepancy in the central-axis values appears smaller than expected from the PDD, simply because the profiles could not be plotted at the exact same depths, which has a strong impact on the doses at depth of R_{50}.
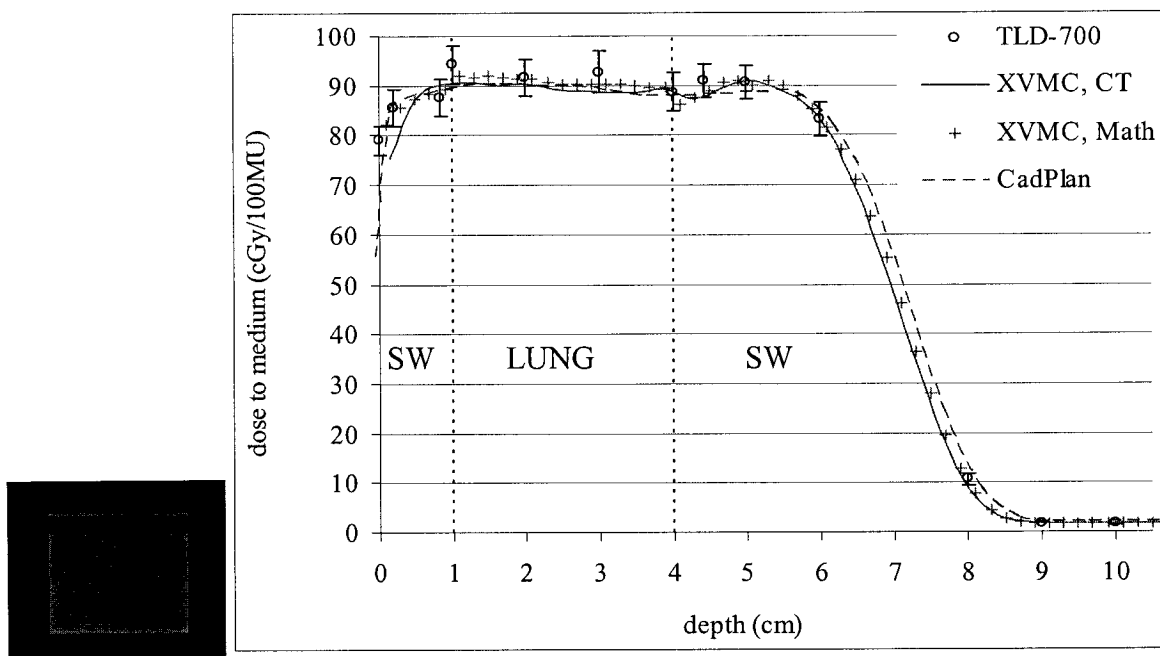
Figure 4.23: Validation of the central-axis doses calculated by CadPlan and XVMC in the case of a 12 MeV electron beam of size 10x10 cm² impinging on a solid water phantom with a 3 cm lung slab at 1 cm depth. The CadPlan calculations in the CT image of the phantom (dashed line) and the XVMC simulations in the compressed CT image of the phantom (continuous line) and in a mathematical phantom (+) are compared to the measurements performed with TLD-700 (o).
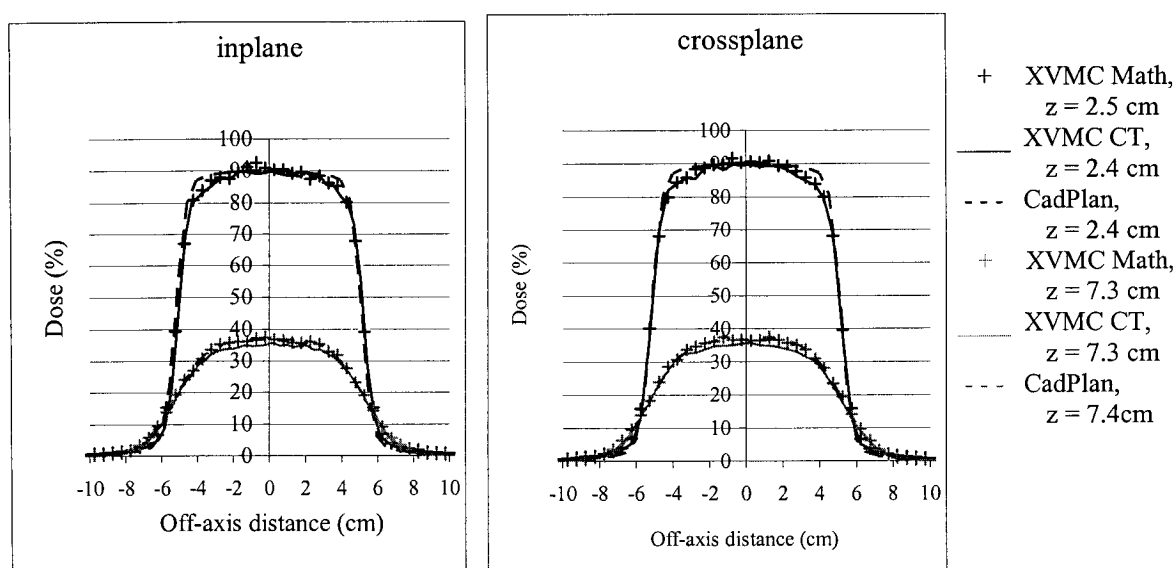
Figure 4.24: Profiles at z_{max} and R_{35} for a 12 MeV electron beam with a 10x10 cm² field size impinging on a solid water phantom with a 3 cm lung slab at 1 cm depth. The XVMC simulations in a compressed CT image (continuous line) and in a mathematical phantom (◊) are compared to the dose calculations performed by CadPlan (dashed line).

The CadPlan and XVMC calculations for the isodose distribution on the central axial slice of the CT images of the phantom with the lung heterogeneity match within 3% of the highest dose in region of low doses with small dose gradients and within 5 mm in region of high doses gradient, as presented in Figure 4.25. However, the 85 cGy idosose appears to be bulging out for CadPlan with respect to XVMC. This effect was observed in the homogeneous solid water phantom as well and is thus not due to the heterogeneity. However, the fact that the XVMC isolines are constricted at the lower end of the heterogeneity as well leads to the conclusion that this is an interface effect.

Both CadPlan and XVMC provide accurate dose calculations in the case of a phantom with a 1-dimensional low density heterogeneity, except at the surface for CadPlan and at the surface for XVMC in the CT phantom.
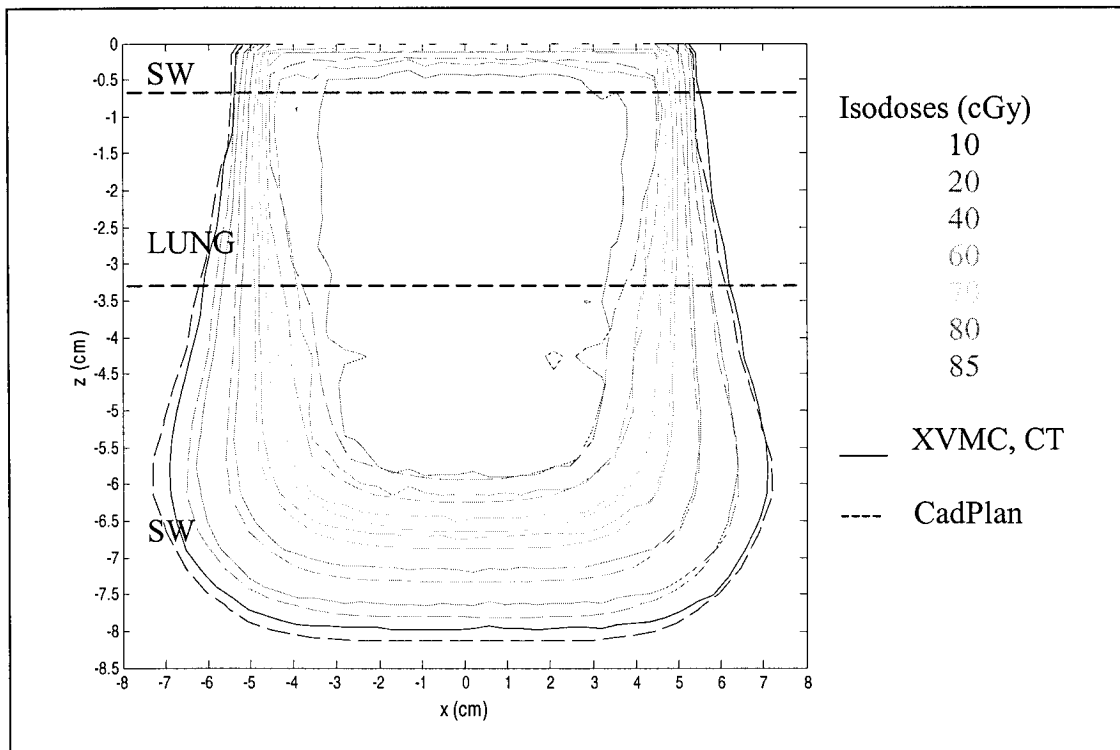
Figure 4.25: Axial isodose distribution for a 12 MeV electron beam with a 10x10 cm^2 field size impinging on a solid water phantom with a 3 cm lung slab at 1 cm depth. The doses correspond to the dose to medium for XVMC and the dose to water for CadPlan expressed in cGy per 100 monitor units. The XVMC simulations in a compressed CT image (continuous line) are compared to the dose calculations performed by CadPlan (dashed line).

4.4.3 Heterogeneous bone phantom

The depth dose curve in a phantom containing a 3 cm-thick bone heterogeneity falls-off much more rapidly than it would in a homogeneous solid water phantom, as appears in Figure 4.26. The electrons scattered out from the denser material are more numerous than the electrons in-scattered. In Figure 4.26, the depth dose curve calculated by CadPlan in the CT image of the phantom and that calculated by XVMC in the compressed CT image of the phantom and in a mathematical phantom are compared to TLD-700 measurements. The dose predicted by XVMC in the mathematical phantom is in excellent agreement with the measurements in the build-up region, including at the solid water-bone interface. But the dose in the fall-off region is underestimated by up to 6% with respect to measurements. When XVMC is run with the CT image of the phantom, the sharp dose fall-off at the solid water-bone interface is not modeled accurately, because of a strong CT beam hardening artefact before and after the bone slab which incorrectly increases the density of the voxels in the first centimetre of the phantom (Figure 4.27). This CT artefact is obviously to blame for the shift of the dose fall-off region towards larger depths both in XVMC and CadPlan. CadPlan underpredicts the surface dose by 50% and becomes closer to the measurements only at depths beyond 5 mm. Furthermore, the dose fall-off is shifted downstream by 5 mm. This experiment shows, in the extreme case of a thick, high density heterogeneity, how strongly CadPlan and XVMC calculations can be affected by CT artefacts.

The profiles simulated by CadPlan and XVMC plotted in Figure 4.27 have comparable shapes and widths. In addition, the central-axis dose discrepancies correspond to those formerly reported for Figure 4.26.
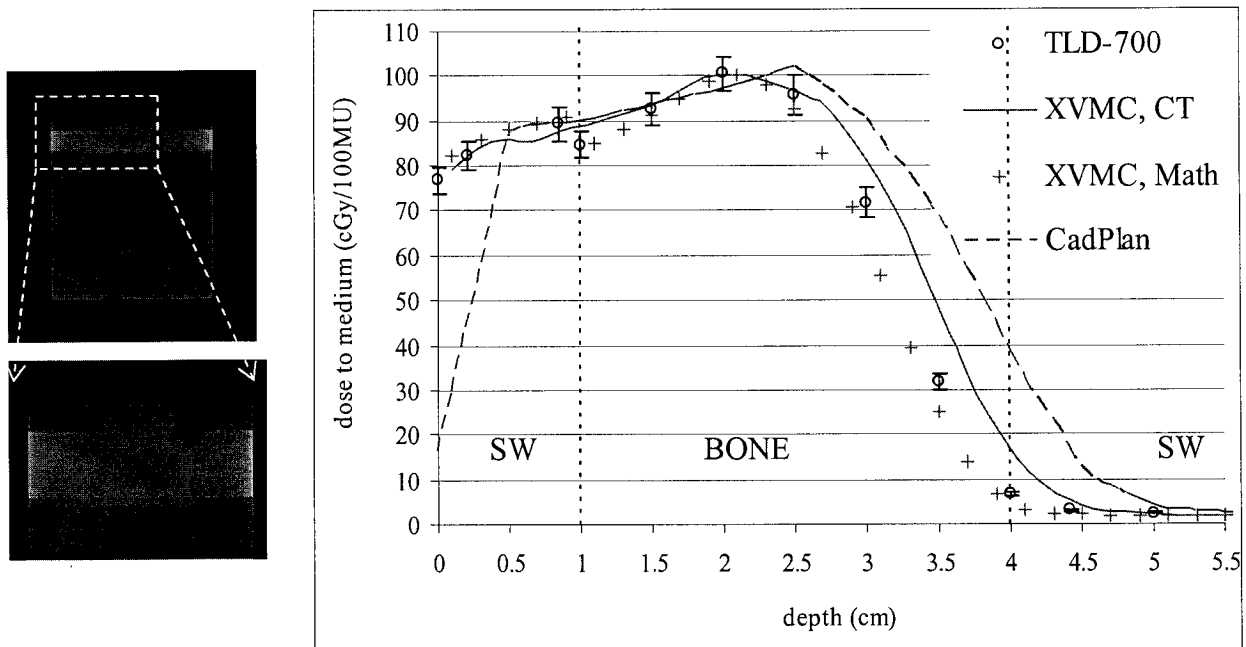
*Figure 4.26: Validation of the central-axis doses calculated by CadPlan and XVMC in the case of a 12 MeV electron beam with a 10x10 cm² field size impinging on a solid water phantom with a 3 cm **bone** slab at 1 cm depth. The CadPlan calculations in the CT image of the phantom (dashed line) and the XVMC simulations in the compressed CT image of the phantom (continuous line) and in a mathematical phantom (+) are compared to the measurements performed with TLD-700 (o).*
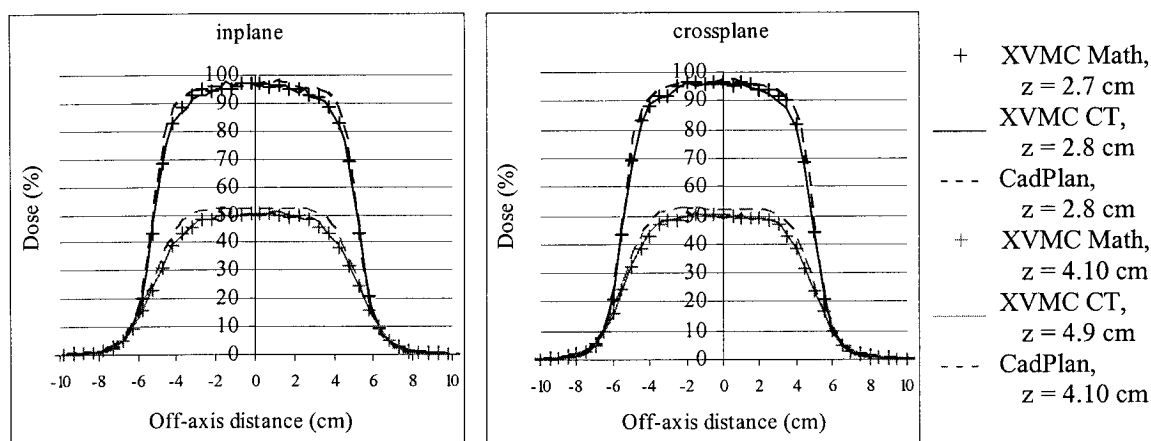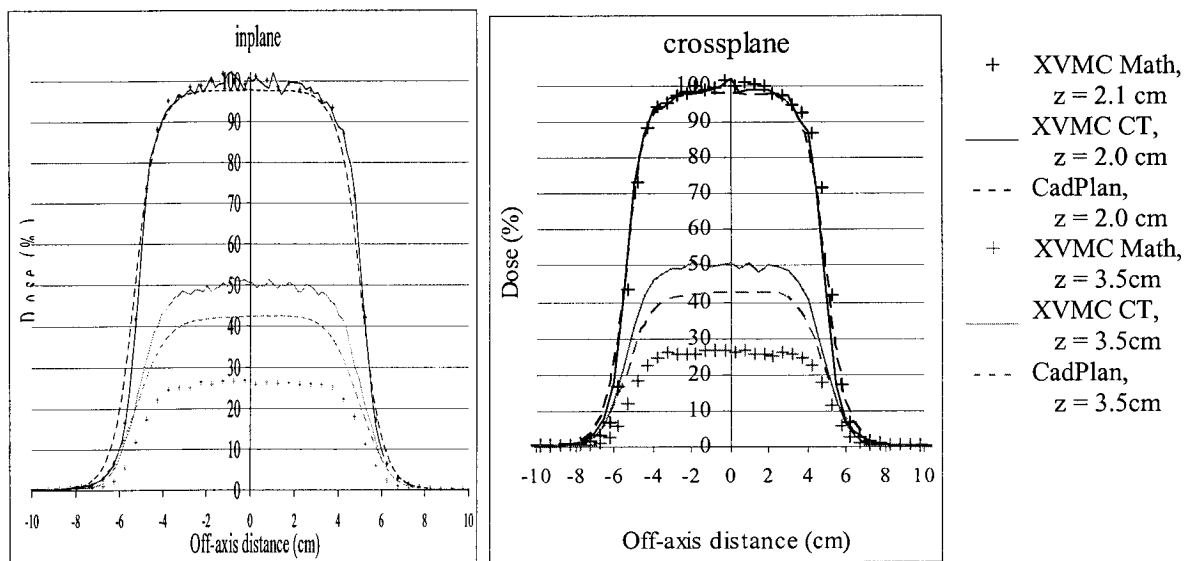

*Figure 4.27: Profiles at z_{max} and R_{50} for a 12 MeV electron beam with a 10x10 cm² field size impinging on a solid water phantom with a 3 cm **bone** slab at 1 cm depth. The XVMC simulations in a compressed CT image (continuous line) and in a mathematical phantom (◊) are compared to the dose calculations performed by CadPlan (dashed line).*

113

The discrepancies in the isodoses in the central axial slice between CadPlan and XVMC presented in Figure 4.28 confirm the trends observed in Figure 4.26 and 4.27. The isodoses are in excellent agreement both in the central-axis dose fall-off region and in the penumbra region. However, the high dose isolines are significantly different as predicted by observation of the PDDs in Figure 4.26. Finally, as previously observed in Figures 4.21 and 4.25, the high dose isolines simulated by XVMC are narrower at shallow depths than in the case of CadPlan.
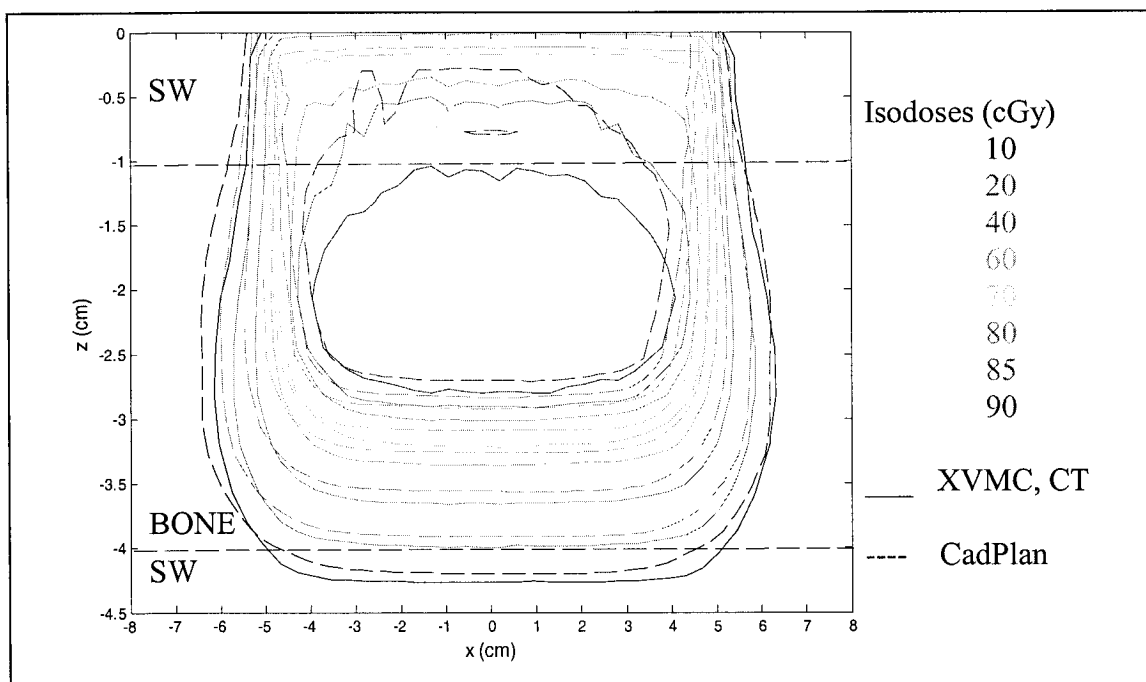
*Figure 4.28: Axial isodose distribution for a 12 MeV electron beam with a 10x10 cm² field size impinging on a solid water phantom with a 3 cm **bone** slab at 1 cm depth. The XVMC simulations in a compressed CT image (continuous line) are compared to the dose calculations performed by CadPlan (dashed line).*

4.4.4 Anthropomorphic phantom

XVMC simulations and CadPlan calculations in a CT image of the head of the Rando Alderson anthropomorphic phantom imaged with the TLD in their measurement position are compared to measurements performed with TLD-100.

Figure 4.29 shows the corresponding depth dose curves, Figure 4.30 the isodoses calculated by CadPlan compared to the TLD dose values and Figure 4.31 the isodoses

calculated by XVMC compared to the TLD dose values, which are not corrected for stopping-power ratio nor for difference in fluence perturbation effects. Figure 4.32 displays the percent difference between the doses to medium calculated by XVMC and measured. The doses predicted by CadPlan are in relatively good agreement with measurements at shallow depths, the surface contour being correctly accounted for by CadPlan. However, the dose falls off too rapidly in the nasal air cavity, the doses after this heterogeneity are underestimated by up to 15%, the error being propagated far below. These inaccuracies in CadPlan are a consequence of the semi-infinite slab approximation, the central-ray approximation, the improper modeling of lateral electron scatter and the range straggling modification function valid only for a narrow range of materials and energies. This concurs with the findings of Glegg *et al*[8] and is slightly worse than the results of Hogstrom *et al*[9] who found an agreement within 5%-4 mm for most points, a 13% underestimation of the dose to septum and an 8 mm isodose shift when irradiating such a phantom with a 13 MeV electron beam of size 8x8 cm^2 in oblique incidence. The above mentioned effect may be partially aggravated due to the fact that CadPlan reports dose to water instead of dose to air, which would be slightly higher and bring the difference between our Cadplan calculation and our measurements closer to that found by Hogstrom. Qualitatively, XVMC accounts better for heterogeneity and provides isodoses appropriately inflected by the long narrow nasal bony structures. The long air cavity results in a locally elongated treatment range as predicted by Monte Carlo but missed by Cadplan. Ma *et al*[10] observed this effect as well. However, the dose in the air cavity appears underestimated by 7% with respect to the raw TLD measurements. This might be attributed to the disregard of the effect of the atomic number on stopping-powers and scatter as well as to the fit of the stopping powers as a function of material density built in XVMC. This analysis can not be conducted more thoroughly without applying corrections to the TLD measurements for stopping-power ratio and fluence perturbation. In addition, fluence perturbation effects may be significant in the low density cavity below the nose. Alternatively, XVMC could be used to report dose to lithium-fluoride using the electron fluence calculated on the fly in the CT digitized phantom.
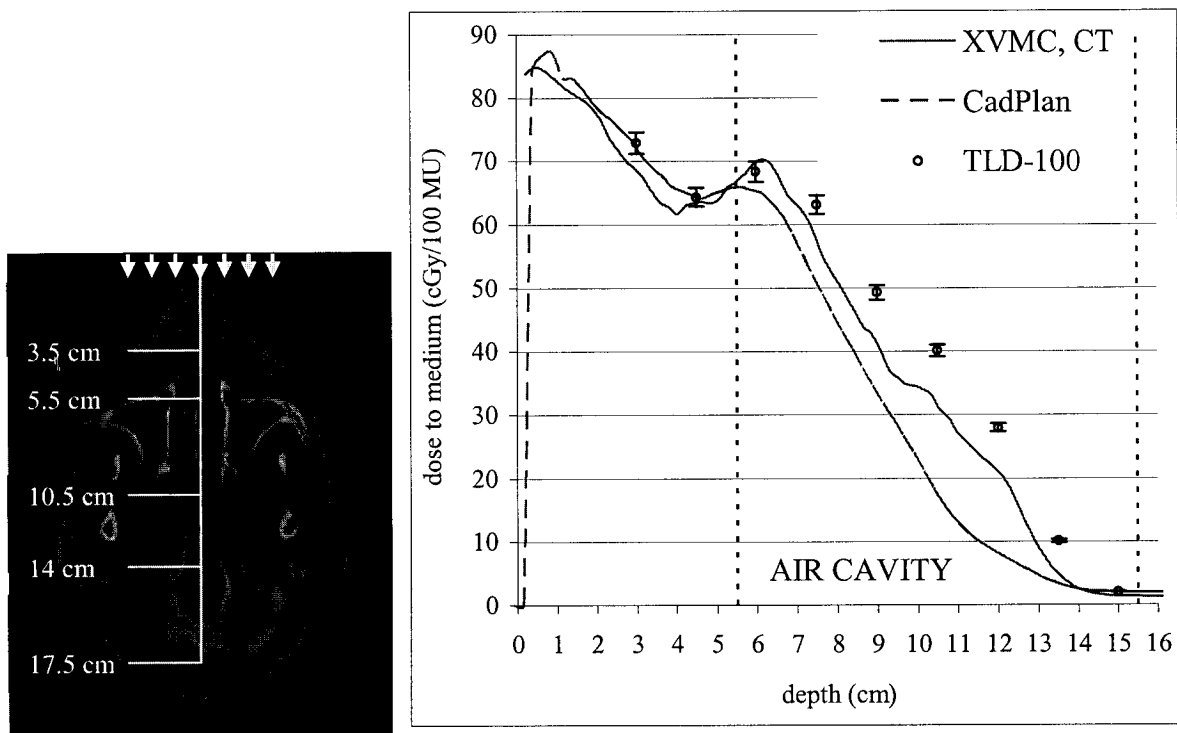
Figure 4.29: Comparison of the central-axis dose calculated by CadPlan and XVMC for a 12 MeV electron beam with a 10x10 cm^2 field size impinging on the nose of the anthropomorphic phantom. The CadPlan calculations in the CT image of the phantom (dashed line) and the XVMC simulations in the compressed CT image of the phantom (continuous line) are compared to the raw measurements performed with TLD-700 (o).
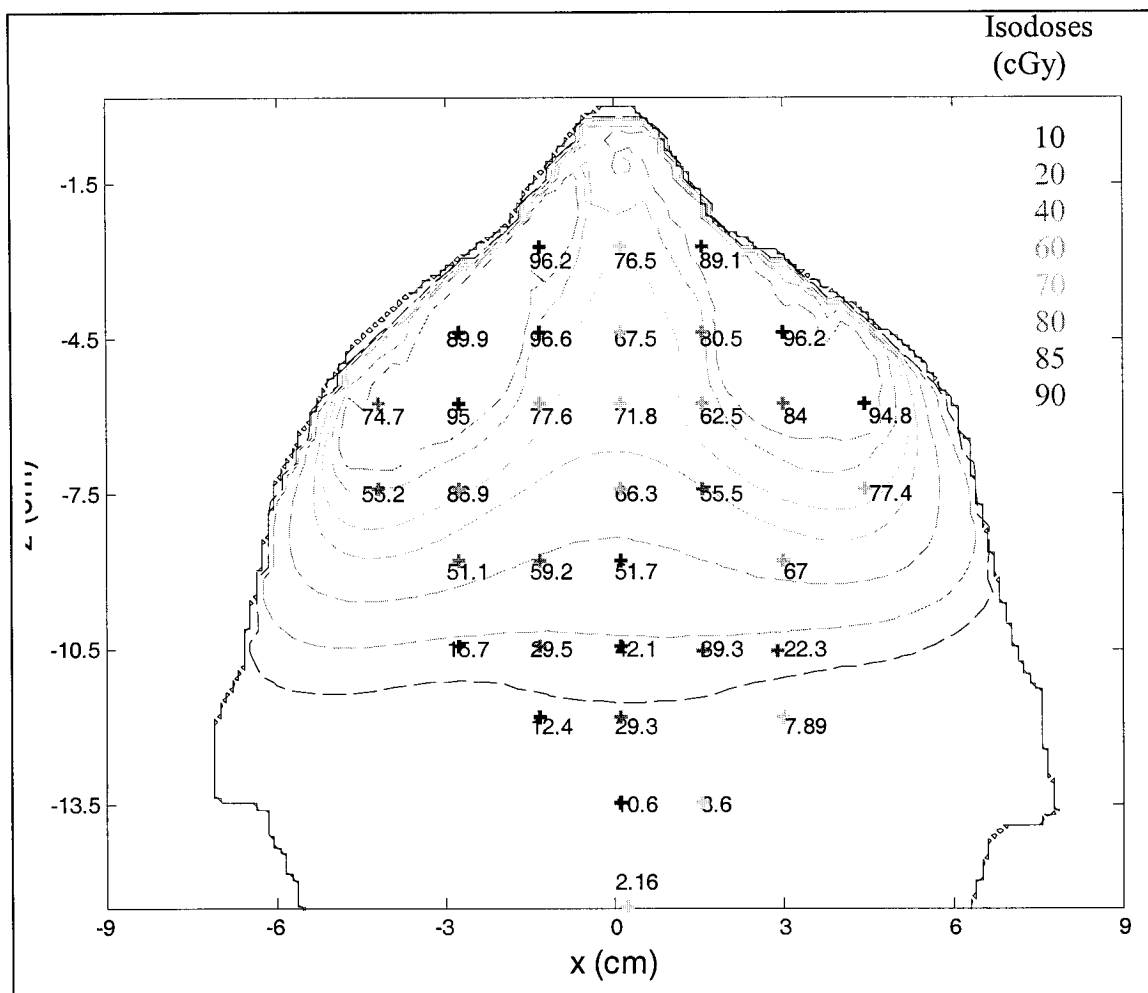
Figure 4.30: Axial isodose (in cGy/100 MU) distribution for a 12 MeV electron beam with a 10x10 cm^2 field size impinging on the nose of the anthropomorphic phantom. The dashed line represents CadPlan doses reported to water and the crosses with a number correspond to raw TLD measurements reported as dose to medium.
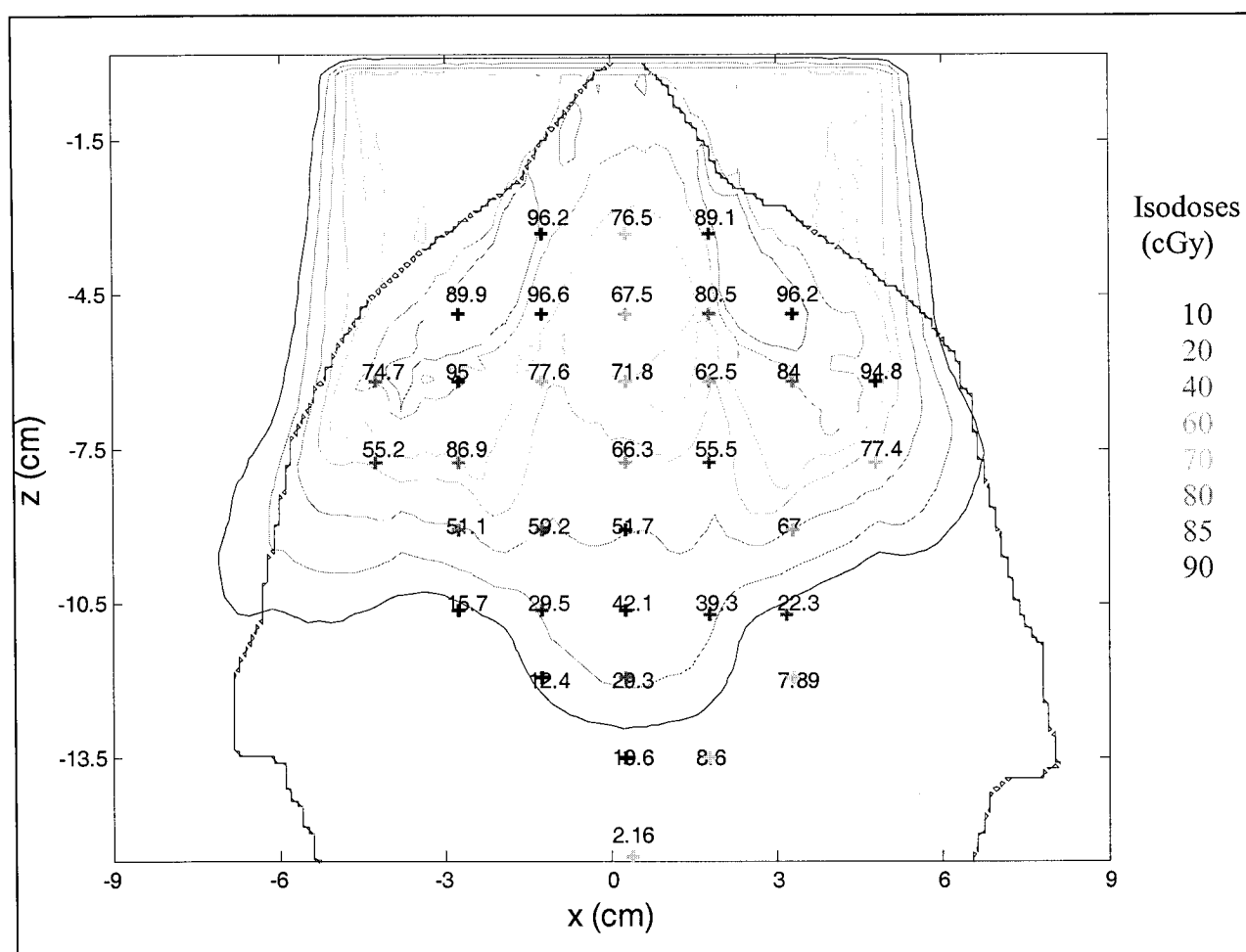
Figure 4.31: Axial isodose (dose to medium in cGy/100 MU) distribution for a 12 MeV electron beam with a 10x10 cm² field size impinging on the nose of the anthropomorphic phantom. The continuous line represents XVMC simulations, the dashed line represents CadPlan calculation and the crosses accompanied by a number correspond to raw TLD measurements.
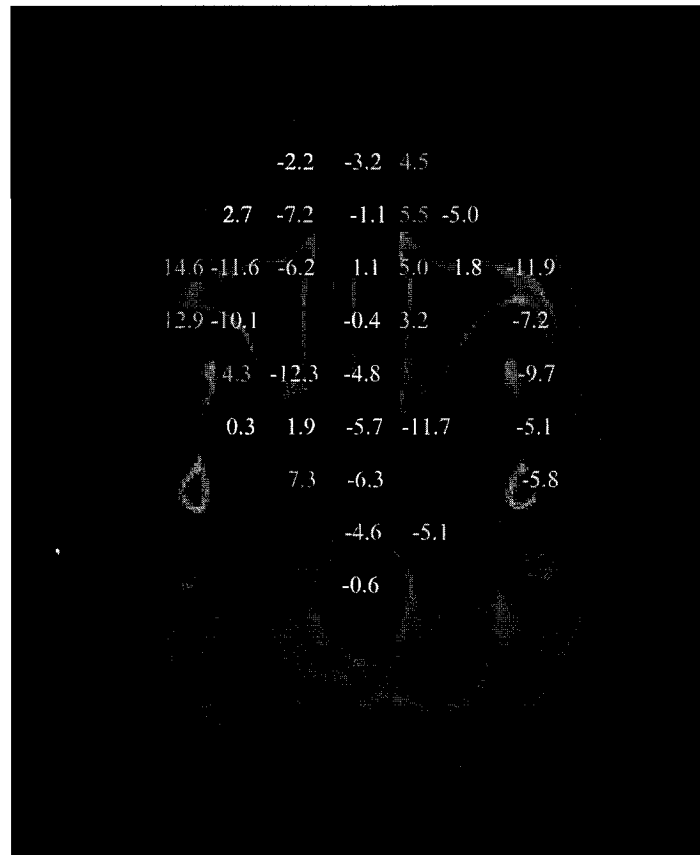
Figure 4.32: Percent difference (D_{MC}-D_{TLD})x100 between the XVMC calculated and measured dose to medium for a 12 MeV electron beam with a 10x10 cm^2 field size impinging on the nose of the anthropomorphic phantom. Differences written in yellow, blue and orange are within ±3%, lower than -3% and larger than +3% respectively.

As a conclusion, comparison of dose distributions calculated by XVMC and CadPlan with TLD measurements established the ability of both systems to predict dose accurately in rectangular phantoms with a 1-dimensional heterogeneity, despite inaccuracies in the surface dose produced by Cadplan. CadPlan failed at calculating the dose distribution accurately in a phantom containing a narrow 3-dimensional heterogeneity, whereas XVMC achieved a closer agreement with measurements. Both systems lead to erroneous dose distributions in CT images containing serious artifacts.

References:

[1] G. G. Zhang, D. W. O. Rogers, J. E. Cygler, T. R. Mackie, "Monte Carlo investigation of electron beam output factors versus size of square cutout", Med. Phys. **26** (5), 743-750 (1999)

[2] F. Verhaegen, C. Mubata, J. Pettingell, A. M. Bidmead, I. Rosenberg, D. Mockridge, A. E. Nahum, "Monte Carlo calculation of output factors for circular, rectangular and square fields of electron accelerators (6-20 MeV)", Med. Phys. **28** (6), 938-949 (2001)

[3] J. E. Cygler, G. M. Daskalov, G. H. Chan, G. X. Ding, "Evaluation of commercial Monte Carlo electron treatment planning", Med. Phys. **31** (1), 141-153 (2004)

[4] G. X. Ding, J. E. Cygler, G. G. Zhang, M. K. Yu, "Evaluation of a three-dimensional electron beam treatment planning system", Med. Phys. **26** (12), 2571-2580 (1999)

[5] ICRU, "Use of Computers in External Beam Radiotherapy Procedures with High-Energy Photons and Electrons", ICRU Report No. 42, International Commission on Radiation Units and Measurements, Washington, D.C. (1987)

[6] D. Hodefi, "Evaluation of CadPlan for electron beam treatment planning", M. Sc. Thesis, 2004

[7] R. Doucet, "Experimental verification of Monte Carlo calculated dose distributions for clinical electron beams", M. Sc. Thesis (2001)

[8] M. M. Glegg, "Electron dose calculations: a comparison of two commercial treatment planning computers", Med. Dosim. **28** (2): 99-105 (2003)

[9] K. R. Hogstrom, P. R. Almond, "Comparison of experimental and calculated dose distributions", in A. Brahme, "Computed electron beam dose planning", Acta Radiol. Suppl. **364**, 89 (1983)

[10] C. M. Ma, E. Mok, A. Kapur, T. Pawlicki, D. Findley, S. Brain, K. Forster, A. L. Boyer, "Clinical implementation of a Monte Carlo treatment planning system", Med. Phys. **26** (10), 2133-2143 (1999)

Chapter 5. Conclusion and future work

5.1 Summary and conclusions

The main objective of this project was to build a Monte Carlo system that transports particles through arbitrarily shaped cutouts and calculates the corresponding cutout factors for clinical electron beams. Monte Carlo simulated and CadPlan calculated isodose distributions in CT images of clinically relevant phantoms were also compared to measurements.

5.1.1 BEAM model for a linac Varian CL2300 C/D

A model for the linac Varian CL2300C/D in the electron mode was built for all energies and applicators. Its predictions are in good agreement with measurements performed with a p-Si diode within experimental uncertainty (2.5%-3 mm). The model should be improved for dose calculations at the edge of the beam, where it underestimates doses by 2 to 5%. Phase space files were collected with this model and used as input in the cutout calculator and in the dose distribution simulations.

The BEAM model was tested only at an SSD of 100 cm and in perpendicular incidence. Although the model should theoretically work at extended SSDs and under oblique beam incidence as well, a thorough evaluation will be necessary.

5.1.2 CUTOUT calculation system

An in-house developed EGSnrc user code, CUTOUT, was tested and debugged. The depth dose curves and cutout factors calculated with CUTOUT for regular and irregular fields of half-dimension ranging from 1 to 25 cm at all energies are in excellent agreement with diode measurements, within experimental and statistical uncertainty, for fields larger than 2 cm. For narrower fields, the CUTOUT code properly models the PDDs but underestimates the cutout factors by up to 13%, the effect worsening with decreasing energy. This issue is still unexplained by may be related to an overestimation of the scoring region dimensions. Measurements of cutout factors for small fields with other detectors such as the Markus chamber and GafChromic film should provide a better

understanding of this issue. The depths of maximum dose are perfectly reliable for low energy beams or narrow fields. However, for beams with a wide region of maximum dose, the depth of maximum dose is more difficult to determine accurately both in measurements and simulations. When the PDD is not smooth, the depth dose curves should be fitted rather than solely scanned for the depth of maximum dose. Examination of the output phase spaces by plots of dose profiles by EGSnrc/DOSXYZnrc gave satisfactory results on the studied cases, but more tests are required to complete the validation.

A REALbasic Graphical User Interface facilitates the use of the code and makes it accessible from any computer in the clinic, regardless of the operating system. It creates input files, triggers execution of the CUTOUT code and extracts the results. It also allows for *in situ* digitization of the cutout, calculation status information and real-time display of the results as they are being calculated. All the calculated cases are retrievable thanks to a dynamic filing system, the cases being sorted by linacs, energies, applicator, field and patient name or ID.

On average, a 10 million particle phase space can be collected in 10 minutes and a 2% statistical uncertainty on the dose values results can be achieved in 30 minutes on a single 1.9 GHz processor, although the calculation time strongly depends on the transport parameters, the dimension of the field, the scoring region and the desired statistical uncertainty. The relatively long calculation time was deemed acceptable by the clinical staff of the Montreal General Hospital, who uses the system in its current state on a stand-alone machine. However, the efficiency of the program could be drastically improved by introduction of variance reduction techniques or by parallelization.

5.1.3 Dose distributions in homogeneous and heterogeneous phantoms

Dose distributions calculated by the XVMC Monte Carlo code and CadPlan in CT images were compared to TLD measurements in phantoms of clinical interest. They established the ability of both systems to predict dose accurately in CT images of rectangular phantoms with 1-dimensional heterogeneity, provided a minimal image quality. However, CadPlan misses abrupt dose changes at interfaces between materials of different densities and underestimates the surface dose by at least 15%. On the other

hand, the surface dose calculated by XVMC Monte Carlo is accurate within 2% for mathematical phantoms. In CT images of phantoms however, XVMC Monte Carlo can underestimate the dose by up to 5% in CT images of phantom due to voxel averaging issues and can predict a smeared interface effect due to averaging of different densities in a given voxel. Both CadPlan and XVMC Monte Carlo lead to erroneous dose distributions when run in the CT image hampered by a major beam hardening artefact. CadPlan's semi-infinite slab approximation triggers erroneous dose distributions beside and below 3-dimensional heterogeneities of dimension smaller than the range of laterally scattered electrons.

5.2 Future work

The Monte Carlo cutout calculation system provided to the clinic, although reliable, should be further developed and improved in various ways.

5.2.1 CUTOUT calculation system

As previously mentioned, the output phase spaces produced by the CUTOUT code should be tested in a few more cases by calculation of dose profiles using them as input in DOSXYZ. Prediction of output factors by DOSXYZ using such phase spaces for the field of interest and for the field of reference should be studied as well for the phase space calculation, before the validation process can be considered complete.

The efficiency of the CUTOUT code can be increased by implementation of variance reduction techniques, namely discarding the numerous photons contained in a phase space and establishing a skin depth beyond which scattered electrons are discarded, as discussed in section 4.3.2. The execution could also be split into batches and sent on a cluster of computers.

Numerous developments of the program can be imagined. First, as suggested by the MGH staff, automation of the Monte Carlo calculation of lateral profiles and isodoses in mathematical phantoms with the fast Monte Carlo code VMC++. Thus, the medical physicist would be provided with data for each treatment plan and this would improve treatment accuracy. This would simply require adaptation of the GUI for running

VMC++ using the phase spaces collected by CUTOUT on pre-generated mathematical phantoms. The CUTOUT code was initially designed to determine cutout factors. To serve this purpose, accurate characterization of the build-up region only was useful. However, the CUTOUT code could also be easily adjusted to calculate whole PDDs without sacrificing resolution. This would simply require to increase the number of scoring regions from 25 currently to 100 or so to make it user-specified such as in the CHAMBER component module in the BEAM code. Then, other clinically useful parameters could be obtained, such as R_{50}, E_0 or R_p.

This study focused on the Varian CL2300C/D, it would be useful to prepare BEAM models and input phase spaces for other treatment machines of the MGH.

5.2.2 Dose distributions in homogeneous and heterogeneous phantoms

In order to allow better comparison of calculated and measured isodoses, the stopping-power ratio and fluence corrections are needed. The stopping-power ratio corrections could be obtained by modifying existing MC codes. Either the SPRXYZnrc user code could be adjusted to allow running simulations on CT images; or, the XVMC Monte Carlo code could be modified to report the dose to lithium-fluoride. Correction of the dose values measured by TLD for the fluence perturbation effect should also improve the results.

Measurements with GafChromic film would also provide interesting information. They would require the abovementioned corrections as well, LiF being then replaced by the film material.

Bibliography

AAPM, "A protocol for the determination of absorbed dose from high-energy photon and electron beams", Task Group 21 Report, Med. Phys. **10** (6), 741-771 (1983) 64

AAPM, "Clinical Electron-Beam Dosimetry", Task Group 25 Report, Med. Phys. **18** (1), 73-109 (1991) 26, 66

AAPM, "AAPM's TG-51 protocol for clinical reference dosimetry of high energy photon and electron beams", Task Group 51 Report, Med. Phys. **26** (9), 1847-1870 (1999) 31, 65

A. A. Al-Beteri, D. E. Raeside, "Optimal electron-beam treatment planning for retinoblastoma using a new three-dimensional Monte Carlo-based treatment planning system", Med. Phys. **19** (1), 125-135 (1992) 8

A. P. Alivisatos, "Less is more in medicine", Sci. Am. **285** (3), 66-73 (2001) 1

F.H. Attix, *Introduction to Radiological Physics and Radiation Dosimetry*, (John Wiley & Sons, New York, 1986) 17

H. J. Bhabba, "The scattering of positrons by electrons with exchange on Dirac's theory of the positron", Proc. Roy. Soc. **A154**, 195-206 (1936) 16

M. J. Berger, "Monte Carlo calculation of the penetration and diffusion of fast charged particles", Methods Comput. Phys. **1**, 135-215 (1963) 39

M. J. Berger and S.M. Seltzer, "ETRAN, Monte Carlo code system for electron and photon transport through extended media", *Documentation for RSIC Computer Code Package CCC-107* (Oak Ridge Natl. Lab., Oak Ridge, Tennessee, 1973) 38

M. J. Berger, J. S. Coursey, M. A. Zucker, "ESTAR, ASTAR and PSTAR: Computer Programs for Calculating Stopping-Power and Range Tables for Electrons, Protons, and Helium Ions (version 1.21)", NIST Report NISTIR-4999, Washington, DC (1992) and online: http://physics.nist.gov/Star, National Institute of Standards and Technology, Gaithersburg, MD (1999) 41, 46

H. Bethe, W. Heitler, "On the stopping of fast particles and on the creation of positive electrons", Proc. Roy. Soc. **A146**, 83-112 (1934) 16

A. F. Bielajew, "HOWFAR and HOWNEAR: Geometry Modeling for Monte Carlo Particle Transport," NRCC Reports PIRS-0341 (1995) 42

W.H. Bragg, *Studies in radioactivity*, MacMillan and Co., London, (1912) 22

A. Brahme, "Current algorithms for computed electron beam dose planning", Radioth. Oncol. **3**, 347-362, (1985) 8

A. Brahme, I. Lax, P. Andreo, "Electron beam dose planning using discrete Gaussian beams. Mathematical background", Acta Radiol. Oncol. **20**, 147-158, (1981) 62

I. A. D. Bruinvis, A. Van Amstel, A. J. Elevelt, R. Van der Laarse, "Calculation of electron beam dose distributions for arbitrarily shaped fields", Phys. Med. Biol. **28**, 667-683 (1983) 28

I. A. D. Bruinvis, W. A. F. Mathol, "Calculation of electron beam depth-dose curves and output factors for arbitrary field shapes", Radiother. Oncol. **11**, 395-404 (1988) 28

I. A. D. Bruinvis, W. A. F. Mathol, P. Andreo, "Inclusion of electron range straggling in the Fermi-Eyges multiple-scattering theory", Phys. Med. Biol. **34** (4), 491-507 (1989) 20

D. T. Burns, G. X. Ding, D. W. O. Rogers "R_{50} as a beam quality specifier for selecting stopping-power ratios and reference depths for electron dosimetry", Med. Phys. **23** (3), 383-388 (1996) 66

J. R. Cameron, N. Suntharalingam, G. N. Kenney, *Thermoluminescent dosimetry*, The University of Wisconsin Press, Madison, 1968 32

D. R. Choi, P. N. Mobit, K. E. Breitman, "The clinical implementation of a method for calculating the output factor and per cent depth dose for an electron beam", Phys. Med. Biol. **48**, 899-908 (2003) 28

E. H. Crosby, P. R. Almond, R. J. Shalek, "Energy dependence of lithium fluoride dosimeters at high energies", Phys. Med. Biol. **11**, 131 (1966) 33

J. E. Cygler, J. J. Battista, J. W. Scrimger, E. Mah, J. Antolak, "Electron dose distributions in experimental phantoms: a comparison with 2D pencil beam calculations", Phys. Med. Biol. **32** (9), 1073-1086 (1987) 7, 60

J. E. Cygler, G. M. Daskalov, G. H. Chan, G. X. Ding, "Evaluation of commercial Monte Carlo electron treatment planning", Med. Phys. **31** (1), 141-153 (2004) 8, 104

G. X. Ding, J. E. Cygler, G. G. Zhang, M. K. Yu, "Evaluation of a three-dimensional electron beam treatment planning system", Med. Phys. **26** (12), 2571-2580 (1999) ....
....7, 28, 45, 105, 108

G. X. Ding, "Energy spectra, angular spread, fluence profiles and dose distributions of 6 and 18 MV photon beams: results of Monte Carlo simulations for a Varian 2100EX accelerator", Phys. Med. Biol. **47**, 1025-1046 (2002) 44

R. Doucet, "Experimental verification of Monte Carlo calculated dose distributions for clinical electron beams", M. Sc. Thesis (2001) 105

R. Doucet, M. Olivares, F. DeBlois, E. B. Podgorsak, I. Kawrakow, J. Seuntjens, "Comparison of measured and Monte Carlo calculated dose distributions in homogeneous phantoms in clinical electron beams", Phys. Med. Biol. **48** (15), 2339-2354 (2003) ...8, 50

E. El-Khatib, J. Antolak, J. Scrimger, "Evaluation of film and thermoluminescent dosimetry of high-energy electron beams in heterogeneous phantoms", Med. Phys. **19** (2), 317-323 (1992) 76

L. Eyges, "Multiple scattering with energy loss", Phys. Rev. **74**, 1534-1535 (1948) 20

E. Fermi (1940) in B. Rossi, K. Greisen, "Cosmic ray theory", Rev. Mod. Phys. **13**,265-268 (1941) 20

M. Fippel, "Fast Monte Carlo dose calculation for photon beams based on the VMC electron algorithm", Med. Phys. **26** (8), 1466-1475 (1999) 44

R. L. Ford, W. R. Nelson, "The EGS Code System (Version 3)", SLAC Rep. 210 Stanford University, Stanford, California (1978) 38

M. M. Glegg, "Electron dose calculations: a comparison of two commercial treatment planning computers", Med. Dosim. **28** (2): 99-105 (2003) 114

S. Goudsmit, J.L. Saunderson, "Multiple Scattering of Electrons," Phys. Rev. **57**, 24 (1940) 20

Gouvernement du Québec, Ministère de la Santé et des Services Sociaux, "La radiothérapie au Québec, situation actuelle et perspectives", Comité de Radio-Oncologie du Conseil Québécois de Lutte contre le Cancer, mars 2000 1

L.H. Gray, "The absorption of penetrating radiation," Proc. Roy. Soc. **A122**, 647-668 (1929) 22

L.H. Gray, "An ionization method for the absolute measurement of y-ray energy," Proc. Roy. Soc. **A156**, 578-596 (1936) 22

D. Harder in *Symposium on High Energy Electrons (Montreaux)*, Eds A. Zuppinger and G. Poretti, Berlin, Springer, p260 (1965) 24

D. Harder, P. Schroder-Babo, A. Mandour, "Unified notation and fast computation of electron beam dose distributions", Private communication, (1982) 26

F. Hobeila, J. P. Seuntjens, "Effect of XCOM photoelectric cross-sections on dosimetric quantities calculated with EGSnrc", in *Standards and codes of practice in medical radiation dosimetry*, Vol. 1, International Atomic Energy Agency, Vienna (2003) 41

D. Hodefi, "Evaluation of CadPlan for electron beam treatment planning", M. Sc. Thesis, 2004 ....63, 64, 105, 107

K. R. Hogstrom, M. D. Mills, P. R. Almond, "Electron beam dose calculations", Phys. Med. Biol. **26** (3), 445-459 (1981) 7, 60

K. R. Hogstrom, P. R. Almond, "Comparison of experimental and calculated dose distributions", in A. Brahme, "Computed electron beam dose planning", Acta Radiol. Suppl. **364**, 89 (1983) 115

K. R. Hogstrom, "3D Electron Beam Dose Algorithms", in *3D Radiation Treatment Planning and Conformal Therapy*, J. A. Purdy, B. Emami, International Symposium Proceedings, Medical Physics Publishing (1995) 8

J. G. Holt, G. R. Elderstein, T. E. Clark, "Energy dependence of the response of lithium fluoride TLD rods in high energy electron fields", Phys. Med. Biol. **20** (4), 559-570 (1975) 33, 74

H. Huizenga, P. R. M. Storchi, "The in-air scattering of clinical electron beams as produced by accelerators with scanning beams and diaphragm collimators", Phys. Med. Biol. **32**, 1011-1029 (1987) 63

S. Hyödynmaa, "Three-dimensional implementations of the generalized Gaussian pencil beam algorithm for electron beam, dose planning", *Ph.D.* Thesis, Technical Research Centre of Finland, Publications 74, Espoo (1991) 62

S. Hyödynmaa, "Dose computation for irregular and blocked electron beams with the generalized Gaussian pencil beam", *Proc. 1st European CadPlan users' meeting*, Luzern, November 14-15, 1991 62

S. Hyödynmaa, "Electron beam dose computation using generalized Gaussian pencil beam algorithm with 3-D inhomogeneity correction and arbitrary field shapes", *Proc. Xth International Conference on the Use of Computers in Radiation therapy*, Manchester, 1994 62

IAEA, "The Use of Plane Parallel Ionization Chambers in High Energy Electron and Photon Beams: An International Code of Practice for Dosimetry," Technical Report Series Vol. 381, International Atomic Energy Agency, Vienna (1997) 24, 45

ICRU, "Radiation dosimetry: Electrons with initial energies between 1 and 50 MeV", ICRU Report No. 21, International Commission on Radiation Units and Measurements, Washington, D.C. (1972) 19, 24, 60

ICRU, "Determination of absorbed dose in a patient irradiated by x or gamma rays in radiotherapy procedures", ICRU Report No. 24, International Commission on Radiation Units and Measurements, Washington, D.C. (1976) 7, 8

ICRU, "Radiation Quantities and Units" ICRU Report No. 33, International Commission on Radiation Units and Measurements, Washington, D.C. (1980) 2, 33, 60

A. Kapur, C-M. Ma, E. C. Mok, D. O. Findley, A. L. Boyer "Monte Carlo calculations of electron beam output factors for a medical linear accelerator", Phys. Med. Biol. **43**, 3479-3494 (1998) 28

A. Kapur, C. M. Ma, "Stopping-power ratios for clinical electron beams from a scatter-foil linear accelerator", Phys. Med. Biol. **44**, 2321-2341 (1999) 65

I. Kawrakow, M. Fippel, K. Friedrich, "3D electron dose calculation using a Monte Carlo algorithm (VMC)", Med. Phys. **23** (4), 445-457 (1996) 43

I. Kawrakow, "Accurate condensed history Monte Carlo simulation of electron transport. I EGSnrc, the new EGS4 version," Med Phys **27** (3), 485 – 498 (2000) 41

I. Kawrakow, D. W. O. Rogers, "The EGSnrc System, Status report" from Advanced Monte Carlo for Radiation Physics, Particle Transport Simulation and Applications: Proceedings of the Monte Carlo 2000 Conference, Lisbon, 23-26 October 2000, Springer, Berlin, 2001. Eds A. Kling, F. Barao, M. Nakagawa, L. Travora, P. Vaz 41

I. Kawrakow and D.W.O. Rogers, "The EGSnrc Code System: Monte Carlo Simulation of Electron and Photon Transport," NRCC Reports PIRS-701, NRC Canada (2001) 41

F. M. Khan, F. C. Deibel, B. J. Gerbi, I. J. Das, "Dosimetry of irregularly shaped electron fields", Med. Phys. **14**, 473 (1987) 28

F.M. Khan and R.A. Potish, *Treatment Planning in Radiation Oncology* (William and Wilkins, Baltimore, 1998) 59, 61

S. C. Klevenhagen, *Physics of Electron Beam Therapy*, Medical Physics Handbooks 13, Adam Higler Ltd, Bristol, England (1985) 2, 26, 30

A. Kosunen, D. W. Rogers, "Beam quality specification for photon beam dosimetry", Med. Phys. **20** (4), 1181-1188 (1993) 43

I. Lax, A. Brahme, P. Andreo, "Electron beam dose planning using Gaussian beams. Improved radial dose profiles", Acta Radiol. Suppl. **364**, 49-59 (1983) 8, 63

I. Lax, A. Brahme, "Electron beam dose planning using Gaussian beams. Energy and spatial scaling with inhomogeneities", Acta Radiol. Oncol. **24**, 75-85 (1985) 8, 63

I. Lax, "Inhomogeneity corrections in electron-beam dose planning. Limitations of the semi-infinite slab approximation", Phys. Med. Biol. **31**, 879-892 (1986) 8

I. Lax, "Development of a generalized Gaussian model for absorbed dose calculation and dose planning in therapeutic electron beams", *Ph.D.* Thesis, Stockholm University (1986) 62

C. M. Ma, E. Mok, A. Kapur, T. Pawlicki, D. Findley, S. Brain, K. Forster, A. L. Boyer, "Clinical implementation of a Monte Carlo treatment planning system", Med. Phys. **26** (10), 2133-2143 (1999) 8, 115

E. Mah, J. Antolak, J. W. Scrimger, J. J. Battista, "Experimental evaluation of a 2D and 3D electron pencil beam algorithm", Phys. Med. Biol. **34**, 235-249 (1986) 7

B. J. McParland, "A parametrization of the electron beam output factors of a 25-MeV linear accelerator", Med. Phys. **14** (4), 665-669 (1987) 28

B. J. McParland, "A method of calculating the output factors of arbitrarily shaped electron beams", Med. Phys. **16** (1), 88-93 (1989) 28

A. F. McKinlay, *Thermoluminescence dosimetry*, Medical Physics Handbooks 5, Adam Hilger Ltd, Bristol, England (1981) 32

ICRU, "Radiation Dosimetry: Electron Beams with Energies Between 1 and 50 MeV" ICRU Report No. 35, International Commission on Radiation Units and Measurements, Bethesda, Maryland. (1984) 24, 66

ICRU, "Stopping Powers for Electrons and Positrons", ICRU Report No. 37, International Commission on Radiation Units and Measurements, Washington, D.C. (1984) 15, 17, 46

ICRU, "Use of Computers in External Beam Radiotherapy Procedures with High-Energy Photons and Electrons", ICRU Report No. 42, International Commission on Radiation Units and Measurements, Washington, D.C. (1987) 105

ICRU, "Photon, Electron, Proton, and Neutron Interaction Data for Body Tissues", ICRU Report No. 46, International Commission on Radiation Units and Measurements, Washington, D.C. (1992) 44

ICRU, "Prescribing, Recording, and Reporting Photon Beam Therapy", ICRU Report No. 50, International Commission on Radiation Units and Measurements, Washington, D.C. (1993) 6

H. E. Johns, J. R. Cunningham, *The Physics of Radiology*, Ed C. C. Thomas, Springfield, Illinois, 1983 28

D. Jones, P. Andre, J. T. Washington, M. D. Hafermann, "A method for the assessment of the output of irregularly shaped electron fields", Br. J. Radiol. **63**, 59-64 (1990) 28

P. A. Jursinic, R. Mueller, "A sector-integration method for calculating the output factors of irregularly shaped electron fields", Med. Phys. **24** (11), 1765-1769 (1997) 28

M. D. Mills, K.R. Hogstrom, P. R. Almond, "Prediction of electron beam output factors", Med. Phys. **9** (1), 60-68 (1982) 27

M. D. Mills, K.R. Hogstrom, R. S. Fields, "Determination of electron beam output factors for a 20-MeV linear accelerator", Med. Phys. **12** (4), 473-476 (1985) 27

N. Mobit, A. E. Nahum, P. Mayles, "The energy correction factor of LiF thermoluminescent dosemeters in megavoltage electron beams: Monte Carlo simulations and experiments", Phys. Med. Biol. **41**, 979-993 (1996) 23

N. Mobit, G. A. Sandison, A. E. Nahum, "Electron fluence perturbation correction factors for solid state detectors in megavoltage electron beams: Monte Carlo simulations and experiments", Phys. Med. Biol. **45** (2), 255-265 (2000) 33

G. Moliere, "Theorie der Streuung schneller geladener Teilchen II: Mehrfach-und Vielfachstreuung," Z. Naturforsch. **3a**, 78 (1948) 20

C. Møller, "Zur Theories des Durchgangs schneller Elektronen durch Materie", Ann. Phys. **14**, 568-577 (1932) 16, 19

NACP, "Electron beams with mean energies at the phantom surface below 15 MeV", Supplement to the recommendations of the Nordic Association of Clinical Physicists (1980), Acta Radiol. Oncol. Rad. Phys. **20**, 402-415, (1981) 24

A. E. Nahum, "Water/air stopping-power ratios for megavoltage photon and electron beams", Phys. Med. Biol. **23**, 24-38 (1978) 23, 43

National Cancer Institute of Canada: Canadian Cancer Statistics 2003, Toronto, Canada, 2003 1

L. J. Old, "Immunotherapy for cancer", Sci. Am. **275** (3): 150-154 (1996) 1

M. Olivares, F. Deblois, E. B. Podgorsak, J. P. Seuntjens, "Electron fluence correction factors for various materials in clinical electron beams", Med. Phys. **28** (8), 1727-1734 (2001) 33

B. R. Paliwal, P. R. Almond, "Applications of cavity theories for electrons to LiF dosemeters", Phys. Med. Biol. **20** (4), 547-558 (1975) 74

C. A. Perez, L. W. Brady, J. L. Roti, Overview in *Principles and Practice of Radiation Oncology*, Eds C. A. Perez, L. W. Brady, Philadelphia PA: Lippincott-Raven, 1-78 (1998) 1

A. P. Pinkerton, J. G. Holt, J. S. Laughlin, "Energy dependence of lithium fluoride dosimeters and high electron energies", Phys. Med. Biol. **11**, 129 (1966) 33

V. Robar, C. Zankowski, M. Olivares Pla, E. B. Podgorsak, "Thermoluminescent dosimetry in electron beams: energy dependence", Med. Phys. **23** (5), 667-673 (1996) .33

D. W. O. Rogers, B. A. Faddegon, G. X. Ding, C. M. Ma, J. Wei, T. R. Mackie, "BEAM: A Monte Carlo code to simulate radiotherapy treatment units", Med. Phys. **22** (5), 503-524 (1995) 8, 42

D.W.O. Rogers, C.M. Ma, G.X. Ding and B. Walters, "BEAMnrc Users Manual," NRCC Report PIRS-0509(A), National Research Council of Canada, 1996 available online at http://www.sao.nrc.ca/inms/irs/BEAM/users_manual/beamnrc_um/ 43, 52

D.W.O. Rogers and A.F. Bielajew, "Monte Carlo Techniques of Electron and Photon Transport for Radiation Dosimetry" in *The Dosimetry of Ionizing Radiation*, Ed Academic Press, New York (1990) 40

D. W. O. Rogers, I. Kawrakow, B. Walters, "Revised relationship between R_{50} and E_0 for electron beams", Conf. Proc. of the IEEE 2000 (2000) 46

B. Rossi, *High energy particles*, Englewood Cliffs NJ, Prentice Hall (1952) 19, 20

P. Rubin, S. McDonald, R. Qazi, *Clinical Oncology: a multidisciplinary approach for physicians and students*, Eds W. B. Saunders Company (1993) 2

A. S. Saini, T. C. Zhu, "Dose rate and SDD dependence of commercially available diode detectors", Med. Phys. **31** (4), 914-924 (2004) 65

J. Seuntjens, A. Van der Plaetsen, H. Thierens, M. Piessens, "Comparison of measured and calculated dose distributions in lung after electron beam treatment of the chest wall", Med. Phys. **21** (12), 1959-1968 (1994) 7

K. R. Shortt, C. K. Ross, A. F. Bielajew, D. W. O. Rogers, "Electron beam dose distributions near standard inhomogeneities", Phys. Med. Biol. **31** (3) 235-249 (1986) 8, 67

L.V. Spencer, F.H. Attix, "A theory of cavity ionization," Rad. Res. **3**, 239-254 (1955) 22

R. M. Sternheimer, "Density effect for the ionization loss of charged particles in various substances", Atom. Data and Nucl. Data Tables **30**, 261-271 (1984) 41

E. Storm and H. Israel, "Photon cross-sections from 1 keV to 100 MeV for elements Z=1 to Z=100", *At. Data Nucl. Data Tables* **7**, 565-681 (1970) 41

A. Sutton, "Researchers explore possible applications of nanotechnology in cancer treatment", OncoLog **48** (7/8) (2003) 1

N. Tapley, *Clinical Applications of Electron Beams*, Robert E. Krieger Publishing Company, Malabar, FL (1982) 2

M. Tubiana, J. Dutreix, A. Wambersie, *Radiobiologie*, Taylor & Francis, London-New York-Philadelphia (1990) 2

J. Van Dyk, *The Modern Technology of Radiation Oncology: A Compendium for Medical Physicists and Radiation Oncologists* (Medical Physics Publishing, Madison, Wisconsin, 1999) 1, 6, 7

Varian Treatment Planning Systems, *CadPlan, External Beam Modelling Physics*, Varian Medical Systems, Inc., Varian Oncology Systems (1999) 63

F. Verhaegen, R. Symonds-Tayler, H. H. Liu, A. E. Nahum, "Backscatter towards the monitor ion chamber in high-energy photon and electron beams: charge integration versus Monte Carlo simulation", Phys. Med. Biol. **45**, 3159-3170 (2000) 49

F. Verhaegen, C. Mubata, J. Pettingell, A. M. Bidmead, I. Rosenberg, D. Mockridge, A. E. Nahum, "Monte Carlo calculation of output factors for circular, rectangular and square fields of electron accelerators (6-20 MeV)", Med. Phys. **28** (6), 938-949 (2001) 28, 103

B. R. B. Walters, I. Kawrakow, D. W. O. Rogers, "History by history statistical estimators in the BEAM code system", Med. Phys. **29** (12), 2745-2752 (2002) 40

I. Weinberg, A. Wigner, *"Physical Theory of Neutron Chain Reactions"*, University Chicago Press, 1958, p 715 77

D. Wilkins, X. A. Li, J. Cygler, L Gerig, "The effect of dose rate dependence of p-type silicon detectors on linac relative dosimetry", Med. Phys. **24** (6), 879-881 (1997) 66

G. G. Zhang, D. W. O. Rogers, J. E. Cygler, T. R. Mackie, "Monte Carlo investigation of electron beam output factors versus size of square cutout", Med. Phys. **26** (5), 743-750 (1999) 28, 47, 103